Gesellschaft für Mikro- und
Nanoelektronik

GMe Workshop 2006

Proceedings

Workshop organized by the
Society for Micro- and Nanoelectronics
(Gesellschaft für Mikro- und Nanoelektronik –
GMe)

October 13, 2006

GMe

Gesellschaft für
Mikro- und Nanoelektronik

Gesellschaft für Mikro- und
Nanoelektronik

GMe Workshop 2006

Proceedings

Workshop organized by the
Society for Micro- and Nanoelectronics
(Gesellschaft für Mikro- und Nanoelektronik – GMe)

October 13, 2006

Sponsored by:

Gesellschaft für Mikro- und Nanoelektronik
Bundesministerium für Verkehr, Innovation und Technologie
Bundesministerium für Wirtschaft und Arbeit

Program Committee:

Emmerich Bertagnolli
Karl Riedling
Friedrich Schäffler

Editor of the Proceedings:

Karl Riedling

Seminar Organization:
Karl Riedling
Claudia Benedela

Production of the Proceedings:
Claudia Benedela
Karl Riedling

ISBN: 978-3-901578-17-5

Gesellschaft für Mikro- und Nanoelektronik (GMe)
c/o Technische Universität Wien
Institut für Sensor- und Aktuatorsysteme
Gusshausstrasse 27-29/366, A-1040 Vienna

Preface

The “GMe Workshop” continues a long series of seminars on microelectronics technology which have been organized by the Society for Micro- and Nanoelectronics (*Gesellschaft für Mikro- und Nanoelektronik* – GMe; originally “*Gesellschaft für Mikroelektronik*”) since its foundation in the mid-1980s. The original seminars addressed a purely academic audience. They were followed by three larger “GMe Forum” events, which took place at the Vienna University of Technology in 2001, 2003, and 2005, and which put more emphasis on addressing participants from Austrian industrial enterprises and governmental organizations. The “GMe Workshop” was the first event of its kind. Taking place in conjunction with an industrial electronics exhibition, the Vienna-Tec 2006, it was open to the public, but its scope was closer to that of the original seminars. In contrast to the “GMe Forum”, the conference language was German, although the proceedings have been prepared in English. There were two invited lectures from international speakers, but its main focus was on the presentation of the results of the university institutions supported by the GMe.

The Society for Micro- and Nanoelectronics is mainly financed by the Federal Ministry for Traffic, Innovation and Technology (*Bundesministerium für Verkehr, Innovation und Technologie*). Its goal is to promote micro- and nanoelectronics research and technology at Austrian universities with the main aim to stimulate the transfer of know-how to the Austrian industry and by carrying out pilot projects in the GMe supported cleanroom facilities. The relatively small budget of the GMe does not allow full sponsoring of research projects. Nevertheless, the GMe supplements other research funding sources by providing contributions for creating and maintaining state of the art laboratory infrastructure.

The main goal of the GMe in recent years was the support of the two cleanroom centers at the Vienna University of Technology and at the Johannes Kepler University Linz, respectively, where internationally competitive technological equipment has been made available to researchers, students, and industry customers.

We hope that the proceedings will promote the impact of the GMe Forum 2005, and that they may contribute to an even better international cooperation of the Austrian micro- and nanoelectronics research at academic institutions and in industry.

o.Univ.Prof. Dr. Erich GORNIK
President of the GMe

Ao.Univ.Prof. Dr. Karl RIEDLING
Secretary General of the GMe

Workshop Program

09.00 – 10.00	Registration; Coffee
10.00 – 10.15	Opening
10.15 – 11.00	Karl Eberl: „*GaAs based High Power Laser Diodes from Lumics*“ – ***page 3***
11.00 – 11.30	M. Böberl, M. Kovalenko, J. Roither, T. Fromherz, G. Springholz, W. Heiss: „*Narrow-band lead salt photodetectors and solution-processible nanocrystal photodetectors for the midinfrared*“ – ***page 5***
11.30 – 12.00	K. Unterrainer, F.F. Schrey et al.: „*Optical properties of IR quantum dots*“ – ***page 9***
12.00 – 13.30	Lunch Break
13.30 – 14.15	Silke Christiansen: „*Semiconductor nanowires: properties and applications*”
14.15 – 14.45	A. Lugstein, C. Schöndorfer, E. Bertagnolli: „*Synthesis of nanowires in room temperature ambient with a focused ion beam*“ – ***page 15***
14.45 – 15.15	G. Chen, H. Lichtenberger, G. Bauer, W. Jantsch, F. Schäffler: „*Initial stage of the 2D-3D transition of a strained Ge layer on a pit-patterned Si(001) template – Progress in Quantum Dot Array (QDA)*“ – ***page 19***
15.15 – 15.45	S. Kostner, M. J. Vellekoop: „*On-Chip Cytometric Detection of Single Biological Cells Using Integrated Photodiodes*” – ***page 25***
15.45 – 16.00	Coffee
16.00 – 18.00	Poster Session

Poster Presentations

Optoelectronics:

Analytic Methods:

Technology:

Nanodots, Nanowires, and Nanocrystals:

1. C. Schoendorfer, A. Lugstein, and E. Bertagnolli: „*Focused Ion Beam induced Nanodot and Nanowire Growth*“ – ***page 93***
2. E. Auer, M. Steinmair, T. Köck, A. Lugstein, E. Bertagnolli: „*Growth of Si-Nanowires – VLS and SLS*“
3. M. Niedermayr, G. Pillwein, W. Heiss, G. Brunthaler: „*Fabrication of narrow split contacts for nano-crystal investigations*“ – ***page 97***
4. B. Mandl, J. Stangl, T. Mårtensson, M. Brehm, T. Fromherz, G. Bauer, L. Samuelson, W. Seifert: „*Metal-free growth and characterisation of* $InAs_{1-x}P_x$ *nanowires*“ – ***page 101***

Si/SiGe:

1. D. Pachinger, H. Lichtenberger, F. Schäffler: „*Stranski-Krastanov Growth of Tensely Strained Si on Ge (001) Substrates*“ – ***page 107***
2. T. Berer, D. Pachinger, G. Pillwein, M. Mühlberger, H. Lichtenberger, G. Brunthaler, F. Schäffler: „*Lateral Quantum Dots in strained Si/SiGe Heterostructures*“ – ***page 111***

Sensor Systems:

1. G. Hairer, D. Graschopf, M. Mansfeld, Ch. Nöhammer, M. J. Vellekoop, „*PCR microsystem for fast cycling*“ – ***page 117***
2. A. Jachimowicz, J. Schalko, J. Kuntner, F. Kohl, and B. Jakoby, „*Bridge-based microsensor for determining the thermal properties of liquids*“ – ***page 121***
3. Ch. Riesch, E. Reichel, F. Keplinger, B. Jakoby, „*Measurement of Liquid Properties with Resonant Cantilevers*“ – ***page 127***
4. F. Keplinger, J. Kuntner, A. Jachimowicz, F. Kohl, „*Sensitive Measurement of Flow Velocity and Flow Direction using a Circular Thermistor Array*“ – ***page 133***

List of Participants

DI Stephan Abermann
TU Wien
Institut für Festkörperelektronik
Floragasse 7
A-1040 Wien

Dr. Aaron Maxwell Andrews
TU Wien
Institut für Festkörperelektronik
Floragasse 7
A-1040 Wien

Dipl. Ing. Maximilian Austerer
TU Wien,
ZMNS
Floragasse 7
A-1040 Wien

o.Univ.Prof. Dr. Günther Bauer
Johannes Kepler Universität Linz
Institut für Halbleiter- und Festkörperphysik
Altenbergerstrasse 69
A-4040 Linz

DI Thomas Berer
Johannes Kepler Universität Linz
Institut für Halbleiter- und Festkörperphysik
Altenbergerstrasse 69
A-4040 Linz

Iris Bergmair
Profactor Produktionsforschungs GmbH
A-4407 Steyr-Gleink

o.Univ.Prof. Dr. Emmerich Bertagnolli
TU Wien
Institut für Festkörperelektronik
Floragasse 7
A-1040 Wien

DI Michaela Böberl
Johannes Kepler Universität Linz
Institut für Halbleiter- und Festkörperphysik
Altenbergerstrasse 69
A-4040 Linz

Stephan Bräuer
Johannes Kepler Universität Linz
Institut für Halbleiter- und Festkörperphysik
Altenbergerstrasse 69
A-4040 Linz

Christine Brendt
TU Wien
Institut für Festkörperelektronik
Floragasse 7
A-1040 Wien

Univ. Doz. Dr. Hubert Brückl
ARC Seibersdorf research GmbH
Donau-City-Strasse 1
1220 Wien

Dr. Gerhard Brunthaler
Johannes Kepler Universität Linz
Institut für Halbleiter- und Festkörperphysik
Altenbergerstrasse 69
A-4040 Linz

Dr. Silke Christiansen
Max-Planck_Institut Halle
D-06120 Halle

Ing. Elvira Dzigal
TU Wien
Institut für Festkörperelektronik
Floragasse 7
A-1040 Wien

Dr. Karl Eberl
(CEO - Geschäftsführer)
Lumics GmbH
D-12489 Berlin

Prof. i.R. Dr. Wolfgang Fallmann
TU Wien
Institut für Sensor- und Aktuatorsysteme
Gusshausstrasse 27-29
A-1040 Vienna

Dr. Ernest J. Fantner
SCL-Sensor.Tech.GmbH
A-1220 Wien

Dipl.-Ing. Georg Fercher
TU Wien
Institut für Sensor- und
Aktuatorsysteme
Gusshausstrasse 27-29
A-1040 Vienna

Dr. Karen Forberich
Johannes Kepler Universität Linz
Institut für Halbleiter- und
Festkörperphysik
Altenbergerstrasse 69
A-4040 Linz

Sebastian Golka
TU Wien
Institut für Festkörperelektronik
Floragasse 7
A-1040 Wien

o.Univ.Prof. Erich Gornik
TU Wien
Institut für Festkörperelektronik
Floragasse 7
A-1040 Wien

Gabriel Hairer
TU Wien
Institut für Sensor- und
Aktuatorsysteme
Gusshausstrasse 27-29
A-1040 Vienna

Alma Halilovic
Johannes Kepler Universität Linz
Institut für Halbleiter- und
Festkörperphysik
Altenbergerstrasse 69
A-4040 Linz

Dr. Univ Doz. Kurt Hingerl
Uni Linz
CD Labor für OOM
A-4040 Linz

DI Roman Holly
CD Laboratory of Surface Optics
A-4040 Linz

Dr. Artur Jachimowicz
TU Wien
Institut für Sensor- und
Aktuatorsysteme
Gusshausstrasse 27-29
A-1040 Vienna

Dr. Franz Keplinger
TU Wien
Institut für Sensor- und
Aktuatorsysteme
Gusshausstrasse 27-29
A-1040 Vienna

Dipl. Ing. Stefan Kostner
TU Wien
Institut für Sensor- und
Aktuatorsysteme
Gusshausstrasse 27-29
A-1040 Vienna

Dr. Alois Lugstein
TU Wien
Institut für Festkörperelektronik
Floragasse 7
A-1040 Wien

Bernhard Mandl
Wehrbach 4

Michael Mühlberger
Profactor Produktionsforschungs GmbH
4407 Steyr-Gleink

Michael Niedermayr
A-4040 Linz

Dipl. Ing. Soner Özcan
TU Wien
Institut für Festkörperelektronik
Floragasse 7
A-1040 Wien

Dipl.-Ing. Dietmar Pachinger
Johannes Kepler Universität
A-4040 Linz

Silvia Pflug
TU Wien
Institut für Festkörperelektronik
Floragasse 7
A-1040 Wien

Stefan Pichler
Johannes Kepler Universität Linz
Institut für Halbleiter- und
Festkörperphysik
Altenbergerstrasse 69
A-4040 Linz

Antonia Praus
Johannes Kepler Universität Linz
Institut für Halbleiter- und
Festkörperphysik
Altenbergerstrasse 69
A-4040 Linz

Dr. Karl Riedling
TU Wien
Institut für Sensor- und
Aktuatorsysteme
Gusshausstrasse 27-29
A-1040 Vienna

Dipl.-Ing. Christian Riesch
TU Wien
Institut für Sensor- und
Aktuatorsysteme
Gusshausstrasse 27-29
A-1040 Vienna

Dr. Johannes Schalko
TU Wien
Institut für Sensor- und
Aktuatorsysteme
Gusshausstrasse 27-29
A-1040 Vienna

Stephan Schartner
TU Wien
Institut für Festkörperelektronik
Floragasse 7
A-1040 Wien

DI Christoph Schoendorfer
TU Wien
Institut für Festkörperelektronik
Floragasse 7
A-1040 Wien

DI Matthias Schramböck
TU Wien
Institut für Festkörperelektronik
Floragasse 7
A-1040 Wien

Dr. techn. Frederik Schrey
TU-Wien
Institut für Photonik
Gusshausstrasse 27-29
A-1040 Wien

Prof. Dr. Siegfried Selberherr
TU Wien
Institut für Mikroelektronik
Gusshausstrasse 27-29
A-1040 Wien

Dipl.-Ing. Clemens Simbrunner
Johannes Kepler Universität Linz
Institut für Halbleiter- und
Festkörperphysik
Altenbergerstrasse 69
A-4040 Linz

DI Mathias Simma
Johannes Kepler Universität Linz
Institut für Halbleiter- und
Festkörperphysik
Altenbergerstrasse 69
A-4040 Linz

Dr. Gottfried Strasser
TU Wien
Institut für Festkörperelektronik
Floragasse 7
A-1040 Wien

Dipl.-Ing. Gebhard Thomas
Karolinengasse 12/35
A-1040 Wien

Dipl.-Ing. Enzo Ungersböck
TU Wien
Institut für Mikroelektronik
Gusshausstrasse 27-29
A-1040 Wien

Contents

Nanodots, Nanowires, and Nanocrystals (Posters) ... 91

Si/SiGe (Posters) ... 105

Sensor Systems (Posters) ... 115

Optoelectronics
(Talks)

GaAs Based High Power Laser Diodes from Lumics

Karl Eberl

Lumics GmbH, Carl Scheele-Str. 16, D-12489 Berlin, Germany
www.lumics.com

The Lumics GmbH, based in Berlin, Germany is specialized in laser module components. The product range includes laser diodes and fiber coupled devices in various designs for the use in optical communication networks, analytical instruments and industrial laser applications. It is specialized in development and production of laser devices in the infra-red range from 800nm to 1080nm wavelength.

Lumics was founded in 2000 as a spin-off from the Max-Planck-Institute for solid state research in Stuttgart. The company has invented and utilizes a manufacturing process which includes a proprietary facet passivation technique for high power laser diodes.

Separate confinement InGaAs /AlGaAs quantum well structures are used in the very reliable devices. Doping and composition profiles are optimized for electrical and thermal resistance in order to achieve most efficient operation.

The presentation will include an overview on company founding, VC-financing and business development. Design, performance and applications of laser diodes with operating power levels up to 700mW for single mode and up to 8W for 100µm broad area emitters are presented.

Narrow-Band Lead Salt Photodetectors and Solution-Processible Nanocrystal Photodetectors for the Midinfrared

M. Böberl, M. Kovalenko, J. Roither, T. Fromherz, G. Springholz, W. Heiss

Institut für Halbleiter- und Festkörperphysik, Universität Linz,
Altenbergerstrasse 69, A-4040 Linz

Introduction

Molecular absorption line strengths are much stronger in the midinfrared spectral range than in the near infrared and the visible. Thus, for sensitive gas analysis and atmospheric pollution monitoring highly efficient optoelectronic devices for the midinfrared are required. For portable gas detection systems, infrared spectrometers and other applications, one obvious requirement is to avoid the need for cryogenic cooling of the system components, including also the detectors. To achieve room temperature photodetectors we show two different approaches. One is the use of epitaxial PbTe detectors which we integrated monolithically on optical filter structure like λ/2 microcavities. The second is the development of photodetectors based on solution-processible nanocrystals.

Narrow-Band PbTe Photodetectors

The integrated PbTe detector consists of a 500-nm-thick PbTe photosensitive layer deposited on top of a microcavity filter, designed for a target wavelength of λ = 3.6 µm. The microcavity filter consists of two EuTe/$Pb_{0.94}Eu_{0.06}Te$ Bragg interference mirrors separated by a λ/2 $Pb_{0.94}Eu_{0.06}Te$ cavity layer [1]. For the bottom mirror, a single EuTe/PbEuTe layer pair is chosen, which is sufficient to obtain a reflectivity of 83%, whereas for the top mirror an odd number of layers (3) has to be used in order to obtain similar reflectivities in respect to PbTe. The samples were grown with excess Te flux resulting in a p-type doping of the PbTe layers with a hole concentration of 10^{17} cm^{-3} and a mobility of 1700 cm^2/Vs at room temperature. By adjusting the substrate temperature and the Te to Eu flux ratio during growth, n-type conductivity is obtained in the EuTe films. Mesas were fabricated by standard photolithography and chemical wet etching. Pt/Ti/Au pads are used as ohmic contacts for p-type PbTe whereas In contacts serve as n-type contacts for EuTe.

A cross sectional scanning electron microscope (SEM) image of the complete structure is shown in Fig. 1(a), where the chemical contrast between the layers was enhanced by selective plasma etching. In the SEM image, the PbEuTe and EuTe layers of the Bragg mirrors and of the cavity region as well as the photosensitive PbTe film on top of the structure can be clearly distinguished.

The high optical quality of the microcavity filter is demonstrated by the FTIR transmission spectrum depicted in Fig. 1(a). Within the wide stop band from 2.7 µm to 5 µm a narrow cavity resonance peak at 3.66 µm is observed, corresponding to the first order cavity resonance mode. The full width at half maximum (FWHM) of the peak is 100 nm, which corresponds to a cavity finesse of 27. The photovoltage spectrum of the device under backside illumination in Fig. 1(b) exhibits a single peak at 3.67 µm, which is just above the PbTe band gap at room temperature. This resonance peak position coincides exactly with the strong O=C-H stretching bond absorption line characteristic for non-aromatic aldehydes. This is indicated in Fig. 1(b) by the characteristic absorption spectrum of acetaldehyde used e.g. in the production of perfumes, polyester resins, and basic dyes. Obviously the relative width of the photoresponse peak of $\Delta\lambda/\lambda = 2.7\%$ corresponds very well with the width of the acetaldehyde absorption peak. The single photovoltage peak of the detector coincides in position and line width with the peak found in transmission measurements. Therefore, the photovoltaic response of the detector is directly correlated to the filter transmittance. The broadband feature shown in Fig. 1(b) at shorter wavelengths (< 3 µm) is due to the transmission of the filter structure above the Bragg mirror stop band. This signal can be eliminated by adding a PbEuTe absorber layer underneath the microcavity filter structure, acting as long pass filter and blocking all radiation above the band gap energy. This would allow to obtain detectors with only a narrow-band photoresponse, which can be easily tuned to the molecular vibration-rotation lines of other gases just by adjusting the filter design. Such monolithically integrated detectors would perfectly meet the demands given by compact gas detection systems.

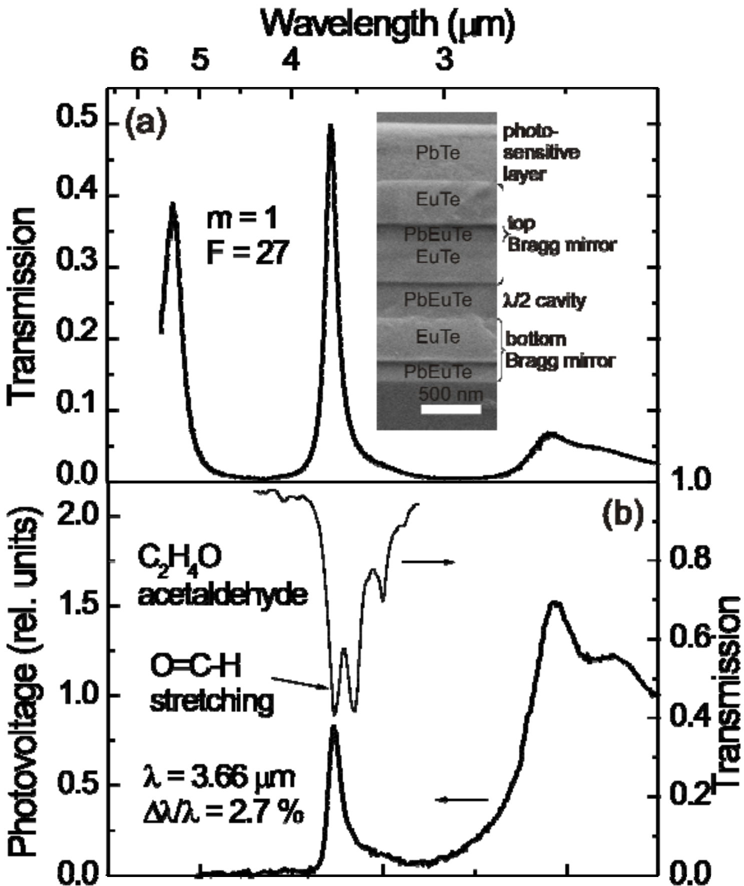

Fig. 1: (a) Transmission spectrum of the integrated PbTe photovoltaic detector on a λ/2 microcavity filter. The inset shows a SEM image of the device cross section. (b) Room temperature photovoltage spectrum of the integrated PbTe photovoltaic detector, compared to the absorption spectrum of acetaldehyde.

Nanocrystal Photodetectors for the Midinfrared

For the solution-processible photodetectors we used HgTe nanocrystals (NC), whose photoluminescence peak can be tuned between 1.2 and 3.5 µm by increasing the NC average size from 3 to 12 nm [2]. The HgTe NCs were prepared in aqueous solutions with hydrophilic thiols as stabilizers. A post-synthetic heat treatment increased the sizes of the NCs and pushed their bandgap to longer wavelength. Subsequently, a ligand exchange with dodecanethiol was carried out making the NCs soluble in commonly used organic solvents. The photoluminescence peak of the NCs can be tuned between 1.2 and 3.5 µm by increasing the NC average size from 3 to 12 nm [2].

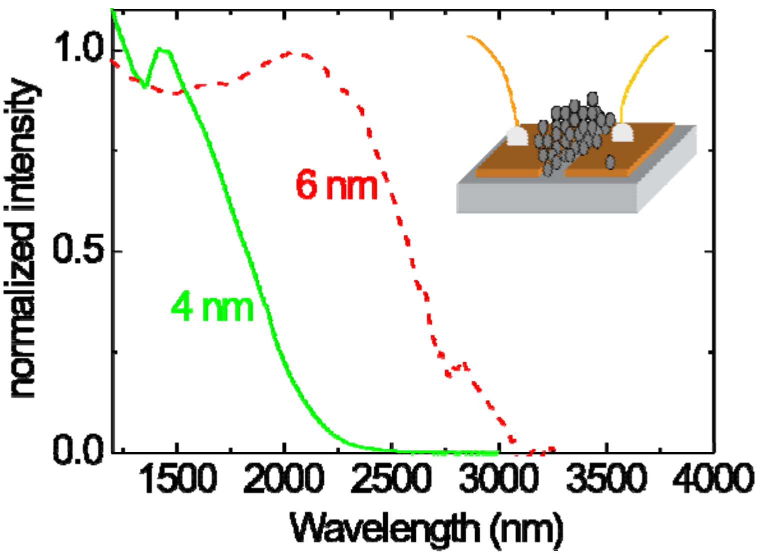

Fig. 2: Sensitivity spectra of HgTe NC photodetectors different in the NC size. The inset shows schematically the device structure.

For photoconductive devices NCs in solution were drop-casted on glass substrates and dried to form solid films. Cr/Au pads with a spacing of 50 µm serve as lateral contacts to the films. The sketch of the device structure is depicted in the inset of Fig. 2. The NC detectors were measured at room temperature and under ambient conditions. The normalized sensitivity spectra of the samples with different HgTe NC sizes are shown in Fig. 2. The onset of the photoresponse for 4 nm-big NCs is around 2.3 µm, whereas the onset for 6 nm-big NCs is shifted to longer wavelength due to the reduced confinement effect and is at 3 µm. The dark current of the NC detectors is about 10 nA. Illumination with a power of only 20 µW increases the current to 300 nA, thus the increase is more than a factor of 10. Measurements of the time behavior show that the time constant of the HgTe NC detectors is less than 20 µs, which is fast compared to organic semiconductor devices. The device structure is not yet optimized; nevertheless the sensitivity obtained from the HgTe NC detectors is 30 mA/W. A big advantage of the HgTe NCs in contrast to conjugated polymers is that they are photostable even under ambient conditions.

The ability to use solution-processible HgTe NCs gives future prospects for infrared devices on flexible or porous substrates and for highly integrated detector arrays.

Conclusion

In conclusion, we demonstrate monolithically integrated PbTe detectors, where the photosensitive PbTe layer is grown on top of a microcavity filter. The detectors show a single resonance in the photoresponse spectrum with a relative width of 2.7%. By adjusting the filter design, the peak wavelength and line width of the photoresponse can be matched to the characteristic absorption lines for various gases, as demonstrated for acetaldehyde. This makes these detectors ideal for molecule identification and quantification purposes in low-cost integrated systems.

Furthermore, we present solution-processible photodetectors based on HgTe NCs. With the size of the NCs the onset of the photoresponse can be tuned. We obtained an onset wavelength of 3 µm which is the longest wavelength demonstrated so far for NC photodetectors. These detectors offer a low-cost possibility to conventional photodetectors for the midinfrared due to the easy process handling.

Acknowledgements

Financial support from bm:bwk, FWF (Project START Y179 and SFB IR-ON) is gratefully acknowledged.

References

[1] M. Böberl, T. Fromherz, J. Roither, G. Pillwein, G. Springholz, W. Heiss: “Room temperature operation of epitaxial lead-telluride detectors monolithically integrated on midinfrared filters” Appl. Phys. Lett. **88**, 041104 (2006)

[2] M. V. Kovalenko, E. Kaufmann, D. Pachinger, J. Roither, M. Huber, J. Stangl, G. Hesser, F. Schäffler, W. Heiss: “Colloidal HgTe Nanocrystals with Widely Tunable Narrow Band Gap Energies: From Telecommunications to Molecular Vibrations” J. Am. Chem Soc., **128**, 3516-3517 (2006)

Ultrafast Spectroscopy of QD Structures for Mid-Infrared Applications

F.F. Schrey, G. Fasching, T. Müller, G. Strasser, K. Unterrainer

Institut für Photonik und Zentrum für Mikro- und Nanostrukturen
Technische Universität Wien, Gusshausstrasse 25-29, A-1040 Wien

Introduction

The capture and relaxation of carriers in semiconductor quantum dots (QDs) has attracted much attention during the last decade, since a profound understanding of these processes is essential for the development of novel optoelectronic devices. A drastic slow-down of the relaxation compared to higher-dimensional structures has been predicted because of the so-called phonon bottleneck effect. However, it has turned out that a number of scattering processes, including multiphonon emission, electron-electron scattering, and electron-hole scattering can circumvent the phonon bottleneck, leading to very different capture and relaxation times from approximately one to above hundred of picoseconds. This discrepancy is still a major problem when the suitability of QDs for optoelectronic applications as well as for applications in quantum information processing has to be evaluated. Therefore it is essential to study fundamental optical properties of self-assembled InAs quantum dots within a GaAs host matrix or within a GaAs/AlAs quantum well superlattice in all relevant spectral regions from the NIR to the THz.

Experiments

For this purpose, we developed a multi-purpose spectroscopy system that can fulfill the special requirements for ultrafast time-domain spectroscopy in the near- and mid-infrared, while considering the dispersion properties of the short laser pulses as well as highly sensitive detection schemes in order to allow the study of isolated, single quantum dots. Further, this system offers all standard characterization methods for single quantum dot investigations and ensemble experiments such as micro-photoluminescence, photoluminescence excitation and photocurrent spectroscopy.

QD Ensembles

The necessary fundamental studies on QDs are always accompanied by the investigation of quantum dot based mid-infrared photodetectors with and without additional AlAs quantum wells in the GaAs host matrix. Here we developed a suitable model to describe the effects of vertical dot alignment within these structures. From this model, we can correctly predict the spectral photoresponse of such devices based on the growth parameters of the GaAs/AlAs quantum well system and some basic quantum dot parameters such as its exciton ground state energy. Further, it allows predicting and optimizing the polarization characteristics of these devices and explaining the emission spectra of a quantum cascade structure with embedded quantum dots in its active region [1]. As expected, comparison between the model and the experiments indicated a strong influence of the quantum dot potential onto the superlattice structure and vice versa, the dots energetic spectrum is modified due to the presence of the GaAs/AlAs superlattice [2].

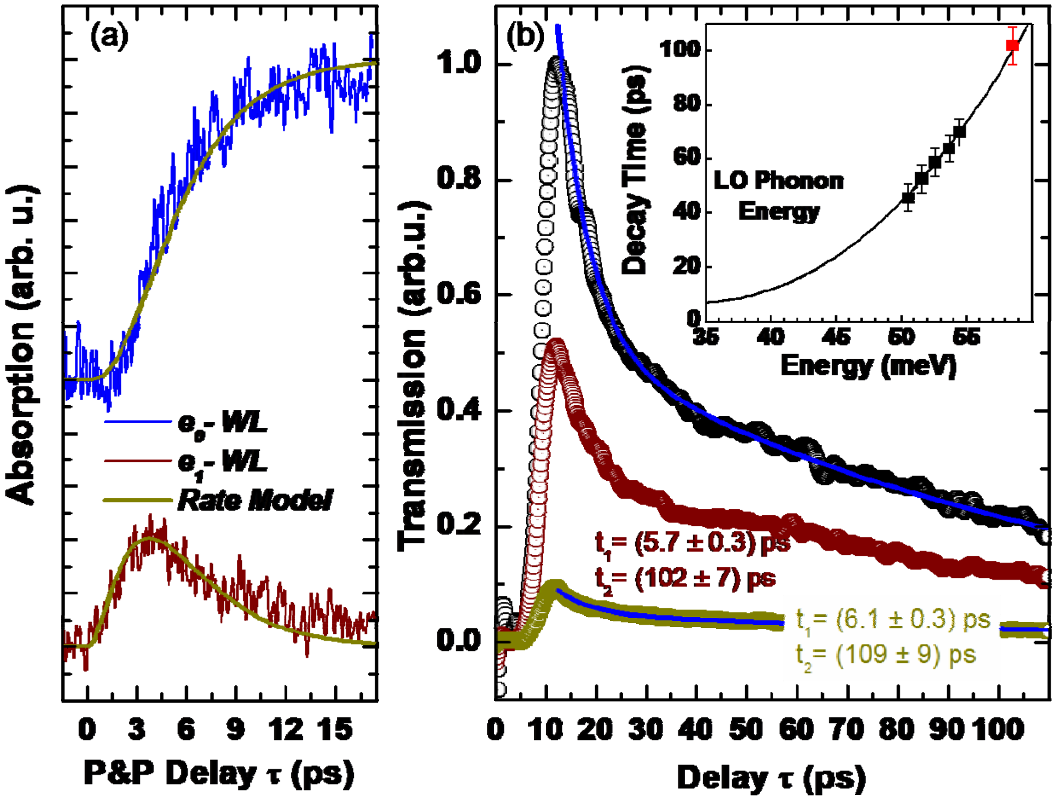

Fig. 1: Time-resolved differential transmission spectroscopy in a NIR pump, THz-probe configuration (a) and in a THz-pump, THz-probe configuration. Method (a) requires optical carrier injection into the QD via the NIR pump pulse, while method (b) traces the decay of excited doping electrons inside the dot. The inset in (b) relates the measured intersublevel decay to a polaronic decay mechanisms as described in [3].

In a parallel approach, we studied the depopulation dynamics of the excited quantum dot exciton and electron states by means of ultrafast interband pump and intersubband probe spectroscopy [4], or by single-color mid-infrared differential transmission spectroscopy on quantum dot ensembles. The related relaxation times vary between only a few and more than hundred picoseconds and strongly suggest extending our investigations to single quantum dots in order to exclude ensemble related effects such as Coulomb interactions within and between different dots [5]. Nevertheless, the obtained excited state lifetimes already point towards a significant influence of phonon related relaxation mechanisms within the quantum dots. Consequently, single quantum dot spectroscopy will also serve as a tool to further characterize these mechanisms. Within these experiments under resonant and non-resonant continuous wave laser excitation, we obtain important information about the energy level redistribution for multi-carrier complexes within a single quantum dot. Photoluminescence excitation studies further reveal and underline possible coupling mechanisms between the discrete quantum dot states and the surrounding matrix via phonons. Therefore, the quantum dot cannot be considered as isolated subsystem within the host matrix, but the variation of the coupling efficiency to different phonon modes for given intersublevel transition within the different dots suggests to further investigate those quantum dots by means of time-resolved spectroscopy for which longer relaxation times might be expected.

QD Ensembles

In a first step we had to evaluate the influence of higher filling states of the single quantum dot intersublevel dynamics. Therefore, we performed emission saturation pump and probe spectroscopy (ESS) for intense pulsed excitation into the wetting layer region of the single quantum dot as shown in Fig. 2 (a) and (b). From a corresponding rate equation model (Fig.2 (c)) we deduced that the main effect of a high carriers density in and around the quantum dot is the shortening of the carrier capture time into the highest discrete quantum dot states, but no significant acceleration of the relaxation process from the excited dot states into the exciton ground state can be observed for these highly excited multi-carrier complexes.

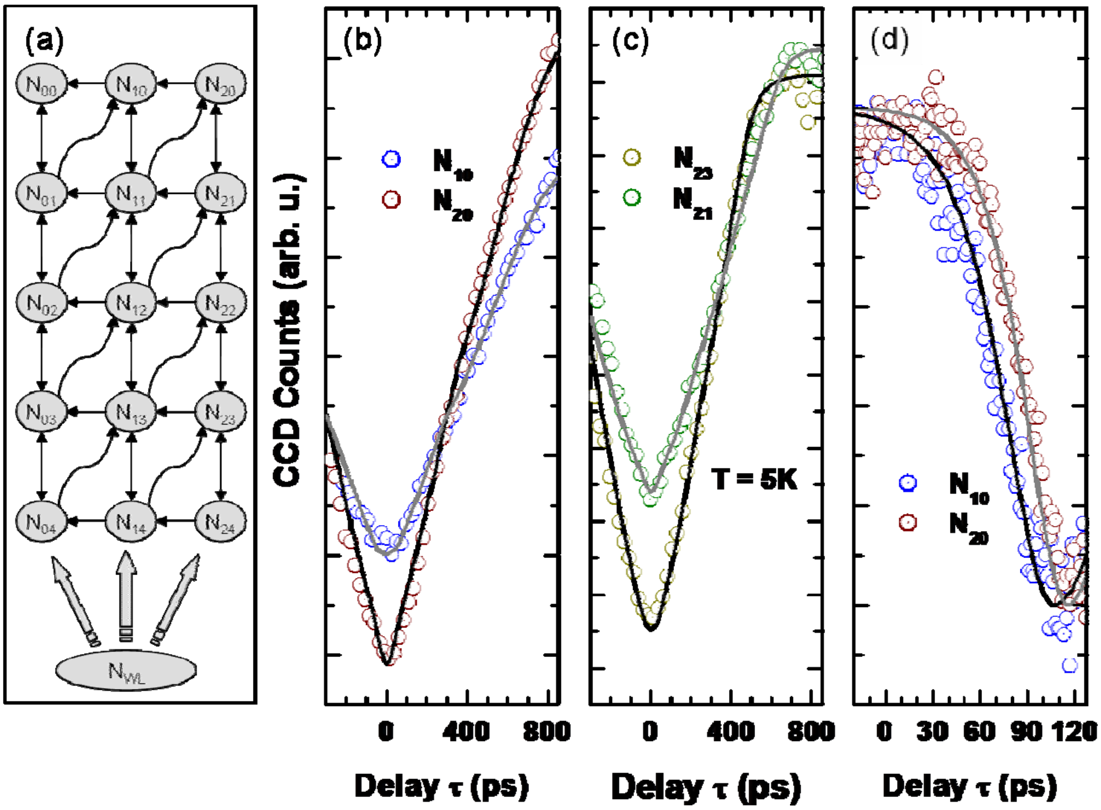

Fig. 2: (a) Scheme of the rate equation system describing the geminate capture and decay of excitons in a single QD. (b) and (c) show the ESS trace of the indicated S-states ($N_{10,}$ N_{20}) and P-states ($N_{21,}$ N_{23}) of a single QD. (d) Interband pump and intersubband probe spectroscopy on the same QD. All experiments lead to intersublevel relaxation times in the range of 60 to 80 ps.

Then we measured the relaxation time from the wetting layer into the exciton ground state by interband pump and intersubband probe spectroscopy, while monitoring the population of the exciton ground state via its electron-hole-pair recombination radiation. The result is shown in Fig. 2 (d). Again we can determine the intersublevel relaxation time between the S- and P-states of the QD to be in the range of several tens of picoseconds. Additionally, to our knowledge, this is also the first time that the influence of ultrafast mid-infrared excitation on the population state of a single self-assembled quantum dot is observed in the time-domain.

Conclusion

As shown in the previous paragraphs, these experiments directly confirm the intersublevel relaxation time to be in the range of several tens of picoseconds, a period that is sufficiently long to use InAs quantum dots in THz related optoelectronic as well as in quantum information processing related applications. Further, the results underline the importance of considering ensemble related effects into the design of QD based devices, since these effects can affect the relaxation times inside the dots strongly. It has to be noted here that until today mostly interband and intraband properties of QDs have been exploited. Our results now strongly motivate to focus also on intersublevel related applications in QDs and QD molecules.

Acknowledgements

This work was supported by the Austrian FWF (SFB ADLIS, SFB IR-ON) and the Austrian Gesellschaft für Mikro- und Nanoelektronik (GMe).

References

[1] F.F. Schrey, T. Müller, G. Fasching, S. Anders, C. Pflügl, W. Schrenk, G. Strasser, and K. Unterrainer, *Physica E* **25**, 271 (2004)

[2] F.F. Schrey, L. Rebohle, T. Müller, G. Strasser, K. Unterrainer, D. Nguyen, N. Regnault, I. Ferreira, and G. Bastard; *Phys. Rev. B* **72**, 155310 (2005).

[3] S. Sauvage, P. Boucaud, R.P.S.M. Lobo, F. Bras G. Fishman, R. Prazeres, F. Glotin, J.M. Ortega, and J.-M. Gérard, *Phys. Rev. Lett.* **88**, 177402 (2002).

[4] T. Müller, F.F. Schrey, G. Strasser, and K. Unterrainer, *Appl. Phys. Lett.* **83**, 3572 (2003)

[5] T. Müller, G. Strasser, and K. Unterrainer, *Appl. Phys. Lett.* **88**, 192105 (2006)

Nanowires and Quantum Dots (Talks)

Synthesis of Nanowires in Room Temperature Ambient with Focused Ion Beams

A. Lugstein, C. Schöndorfer, E. Bertagnolli

Institut für Festkörperelektronik, TU Wien,
Floragasse 7, A-1040 Wien

Introduction

Exciting discoveries of essentially new nanostructures, particularly nanowires, have been sparked by a desire to tune the fundamental optical, electronic, mechanical and magnetic properties of materials through rational control of their physical size. Possible applications range from new-generation nanoelectronics [1] to catalysis [2].

Several techniques for the production of various types of nanowires have been reported, such as thermal gas decomposition or laser ablation of powder targets. Most of them are based on the Vapor-Liquid-Solid (VLS) mechanism, in which metal droplets catalytically enhance the growth of nanowires [3]. The liquid alloy cluster serves as a preferential site for adsorption of reactant from the vapor phase and – when supersaturated – as the nucleation site for crystallization. However, there is still an on-going effort in developing synthesis methods with the main goal to grow nanowires at moderate temperatures not to damage preexisting modules and to grow them at a prespecified location while eliminating the requirement of a later assembly process.

Our study differs from all of the previous reports in that an intense focused ion beam initiates the nanowire growth in room temperature ambient without using any additional materials source.

Experimental

All machining experiments were carried out using the Micrion twin lens FIB system (model 2500) equipped with a Ga liquid metal ion source. For patterning, the 50 keV Ga^+ ion beam is scanned in discrete steps across the sample surface at normal incidence. If not mentioned in particular, the processing was done in the single scan mode, thereby each pixel is irradiated only once and the fluence is adjusted by the dwell time the beam remained on each single spot.

The pattern evolution was observed by top-view and cross-sectional Secondary Electron Microscopy (SEM) of cleaved samples, High Resolution Transmission Electron Microscopy (HRTEM) and Electron Dispersive X-ray (EDX) analysis. The chemical composition of the pattern was evaluated by Auger Electron Spectroscopy (AES) using a VG Microlab 310F system enabling a lateral resolution of 20 nm for elemental analysis.

Results

In our approach, we milled holes from the back side through antimony samples, with sufficient initial smoothness, as schematically shown in Fig. 1(a). Remarkably nanowire formation was observed on both sides of the sample, i.e. at the site of the impinging beam as well as at the plane where the FIB leaves the sample. As FIB milling is done close to the edge of the sample some nanowires extend over the rim of the sample as shown in the SEM image in Fig. 1(b). Thus, enabling HRTEM investigations and Energy Disperse X-ray EDX analysis, of undisturbed nanowires as illustrated in Fig. 1. EDX analysis performed in such a way on individual nanowires proved that the wires consist of pure antimony (left inset in Fig. 1(b)). The Cu signal is an artifact originating from the TEM copper grid. The HRTEM image revealed that the as grown nanowires are amorphous with remarkably uniform diameters in the range of about 25 nm along their entire length (right inset in Fig. 1(b)). Particularly we have investigated the tips of the wires. Neither compositional variations nor solidified catalytic particles, which are characteristic features of a VLS controlled growth mechanism, have been observed on any of the Sb nanowires.

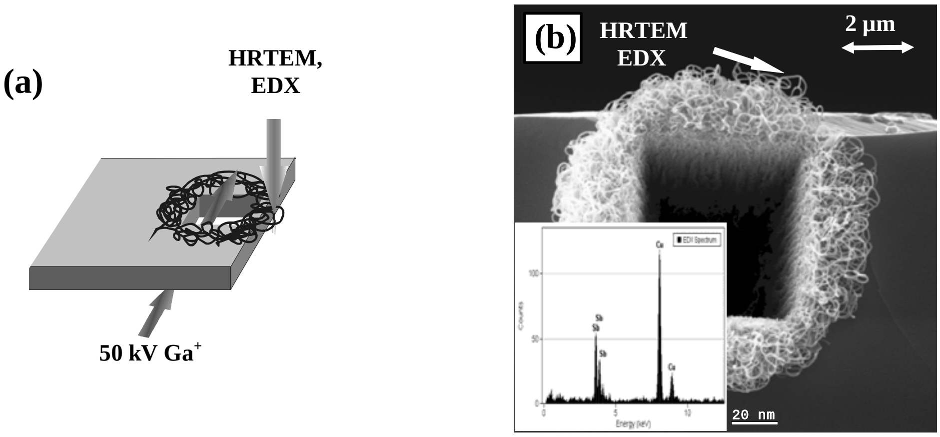

Fig. 1: (a) Schematic illustration of FIB based approach used to synthesize nanowires drilling a hole from the back side through the sample. (b) SEM image of a 5x5 µm^2 wide hole milled trough the sample. The insets show a typical EDX spectrum from an individual nanowire and the HRTEM image of such synthesized wires.

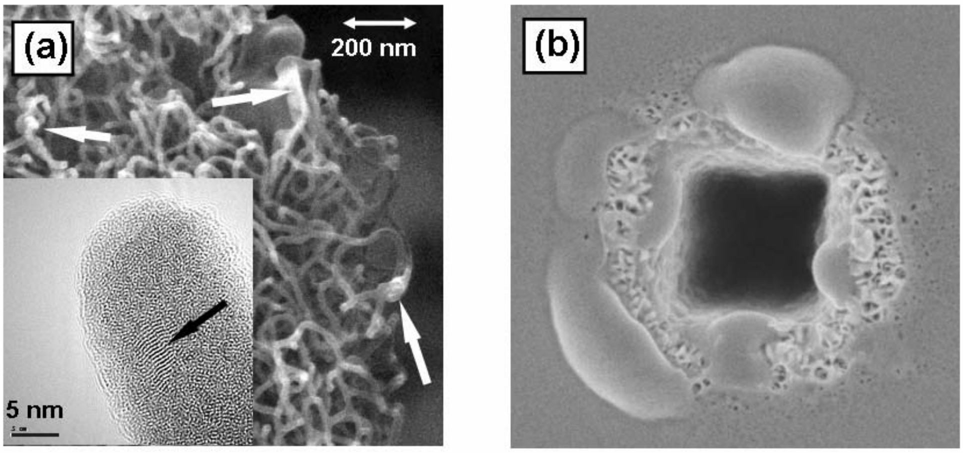

Fig. 2: (a) Low magnified SEM image of the nanowires observed on GaSb after FIB hole milling through the sample. The inset shows a high resolution TEM image of the tip of an isolated GaSb wire with a diameter around 25 nm. (b) SEM image of a hole milled in GaSb with a 30 kV focused Ga$^+$ ion beam.

For GaSb as substrate material FIB exposure leads to the formation of a cellular structure of columnar tangled rods and precipitations embedded within the porous network of nanowires (see SEM image in Fig. 2(a)). AES measurements revealed that the precipitations marked by the white arrows in Fig. 2(a) appear to be pure Ga. HRTEM investigations (inset of Fig. 2(a)) proved that the roughly 25 nm thick wires show mostly an amorphous structure. For some wires a few regions with a diameter up to 5 nm with crystallographic ordering are visible, indicated by the black arrow. The lattice fringes distance observed in the region marked by the black arrow is 0.35 nm and corresponds with the {111} planes in bulk GaSb with cubic Zinkblende structure. The elemental composition of the nanowires investigated using EDX revealed an almost ideal 1:1 stoichiometry of Ga and Sb independent of the morphology. For beam energies of 30 keV or lower, formation of nanowires could be observed neither for GaSb nor Sb substrates. Fig. 2(b) shows the SEM image of the GaSb surface after 30 kV FIB exposure. The droplet-like features surrounding the FIB milled hole are Ga droplets as determined by AES measurements.

In accordance with the catalytic VLS approach we suppose that the formation of GaSb nanowires necessitates a catalytic particle, mostly a eutectic alloy, with a low melting point. In our approach we suppose that Ga droplets are formed in situ during FIB exposure (Fig. 3(a) - process step 1). As we have recently reported, FIB milling of GaAs leads to the formation of Ga droplets on the surface [4]. For FIB exposure with the 30 keV beam we have also observed in-situ migration of Ga precipitations on the GaSb surface. We assume that exposing the substrate to the 50 keV Ga+ ion beam leads to material decomposition due to physical sputtering. The excess Ga atoms because of enhanced diffusion agglomerate into Ga-rich precipitations (process step 1). Due to the low melting point of Ga and high energy injection during FIB milling with the 50 keV beam, these precipitations behave like a liquid. Decomposed material from the substrate – diffusing on the surface – is adsorbed and dissolved by the Ga containing clusters (process step 2). Finally, when the concentration of the solved materials exceeds supersaturation, nucleation sites will be formed and initiate the growth of the coexisting solid GaSb phase (process step 3). Nanowire growth from the base continues as long as the droplet remains in a liquid state and reactant is available. In accordance with the phase diagram shown in Fig. 3(b) precipitation of GaSb continues at the liquid-solid as long as the catalytic particle remains in a liquid state and reactant is available.

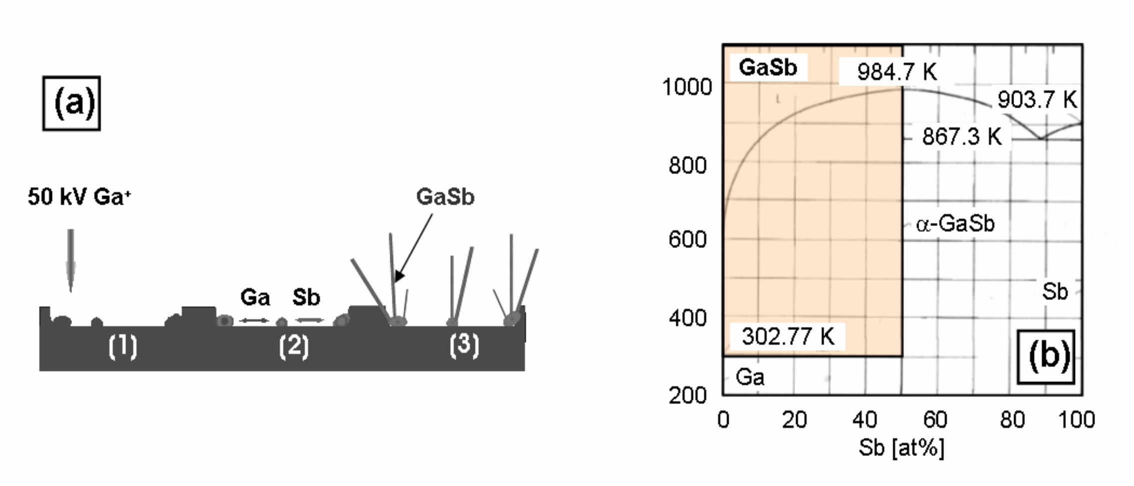

Fig. 3: (a) The proposed growth model; (b) The phase diagram (after Landolt-Börnstein, New Series IV/5) of the binary Ga-Sb system illustrates the thermodynamics of the nanowire growth.

The formation of pure Sb nanowires could be discussed straightforward by examining the Sb rich part of the binary Ga-Sb phase diagram (Fig. 3(b)). Within the framework of our approach, FIB processing of the Sb substrate produces mobile Ga and Sb species on the surface that rapidly agglomerate forming Sb-rich nanoclusters. In case of the Sb substrate Ga is introduced only by the FIB and the concentration of these clusters is somewhere in the right-most part, i.e. the Sb-rich region, of the phase diagram. Again due to supersaturation of the nanocluster, the coexisting pure Sb phase precipitates as nanowires.

At present, we do not understand the origin of the tangling of the nanowires although we note that extensive tangling has been observed previously in Ga based VLS processes [5]. The authors stated also that Ga droplets could simultaneously catalyze the growth of hundreds of thousands of nanowires. Additionally we want to mention that in contrast to the conventional VLS mechanism the growth rate for our approach is extremely high. As the whole FIB processing takes only a few seconds, growth rate must be in the range of a few 100 nm/s.

Conclusion

According to our experimental results, we assume that at least two key parameters are required to induce nanowire formation by an intense FIB. One should use an equilibrium phase diagram to choose a substrate that can form a liquid alloy with Ga. Even when FIB-induced nanowire growth occurs far-off the thermodynamic equilibrium, known phase diagrams can be used to choose a specific composition (catalyst – nanowire material) so that there is coexistence of liquid alloy and solid material. Second, a sufficiently high beam energy to ensure that the liquid alloy is formed during the FIB processing.

The above studies illustrate the potential of our approach for synthesis of nanowires in room temperature ambient without using a gas-type source. We suppose that our approach should not be limited solely to the materials discussed here – other substrates or sources of the ion beam should extend this method to other materials.

Acknowledgements

This work is partly funded by the Austrian Science Fund (Project No. 18080-N07). The authors would like to thank the Center for Micro- and Nanostructures (ZMNS) for providing the clean-room facilities. The financial support from the Austrian Society for Micro- and Nanoelectronics (GMe) is gratefully acknowledged.

References

[1] A. O. Orlov, I. Amlani, G. H. Bernstein, C. S. Lent, G. L. Snider, *Science* 277, 928 (1997); A. B. Greytak, L. J. Lauhon, M. S. Gudiksen and C. M. Lieber, *Appl. Phys. Lett.* 84, 4176 (2004); A. P. Alivisatos, *Science* 271, 933 (1996); S. Sun, C. B. Murray, D. Weller, L. Folks, A. Moser, *Science* 287, 1998 (2000).

[2] M. Valden, X. Lai, D. W. Goodman, *Science* 281, 1647 (1998).

[3] R. S. Wagner, W. C. Ellis, *Appl. Phys. Lett.* 4, 89 (1964).

[4] A. Lugstein, B. Basnar, E. Bertagnolli, *J. Vac. Sci. Technol.* B 22, 888 (2004).

[5] Z. W: Pan, Z. R: Dai, C. Ma, Z. L. Wang, *J. Am. Chem. Soc.* 124, 1817 (2002).

Ordering of Strained Ge Islands on Prepatterned Si(001) Substrates: Morphological Evolution and Nucleation Mechanisms

G. Chen, H. Lichtenberger, G. Bauer, F. Schäffler, W. Jantsch

Institut für Halbleiter- und Festkörperphysik,
Johannes-Kepler-Universität Linz, A-4040 Linz, Austria

Introduction

The spontaneous formation of 3D islands during epitaxial growth of lattice-mismatched heteromaterials (Stranski-Krastanov [SK] growth) has become the most important self-organization mechanism for the fabrication of coherently embedded nanostructures. However, the randomness of island nucleation, and the broad distribution of their size severely restrict the application potential of this approach: Most electronic and spintronic device applications require the individual addressability of such nanostructures, and thus a means for the precise control of their nucleation sites.

We realized perfectly ordered SiGe and Ge islands in two (2D) and three dimensions (3D) by providing preferential nucleation sites through nanostructuring for the SK growth mode [1]. The islands nucleate preferentially at the bottom of reactively ion etched pits, which assume the shape of truncated inverted pyramids, after overgrowth with a thin Si buffer layer. This nucleation site is at first sight rather surprising, because it appears to be the least favorable site for strain relaxation within the pit template. To gain a better understanding of the mechanisms that lead to the preferential nucleation of the Ge dots there, we studied the very early stages of Ge coverage in detail [2].

Experimental

The samples were grown by solid source molecular beam epitaxy (MBE) in a Riber SIVA 45 reactor. Pit-patterned templates on Si(001) substrates were obtained by electron beam lithography and reactive ion etching (RIE) in SF_6. The pits form a regular two-dimensional grid ordered along two orthogonal <110> directions with a periodicity between 260 and 380 nm. After etching, the samples were chemically cleaned to remove RIE deposits and residues from the e-beam resist. Immediately before introduction into the MBE reactor the samples were treated in diluted HF to create a hydrogen terminated surface that stabilizes the nanostructures against transient enhanced diffusion during the following *in situ* thermal treatment at 900°C for 5 minutes. Since we wanted to characterize the very early stages of ordered Stranski-Krastanov growth on prepatterned substrates, we employed growth conditions that were optimized for this purpose over the last few years. MBE growth always commenced with a 100 nm thick Si buffer layer that was grown at a rate of 0.5 Å/s while ramping the substrate temperature from 450°C to 520°C. This procedure eliminates surface roughness and damage induced by RIE, but, most importantly, modifies the morphology and improves the homogeneity of the pattern. Subsequently, 0 (reference for the effect of the Si buffer alone), 2.6, 4, and 5 monolayers (ML) of Ge were deposited at 620°C and at a fixed rate of 0.03 Å/s on samples A, B, C, and D, respectively. An additional series of samples (E, F, G) was grown to investigate the stability of the observed features. Under otherwise identical conditions, 5 ML of Ge were deposited at 670 and 570°C on samples E and F, respectively, and 9 ML at 570°C on sample G. The denoted substrate temperatures were calibrated with a thermocouple embedded into a Si reference wafer to an estimated accuracy of ±15°C. Since the rate for Ge deposition is at the lower limit of our flux controller, we further enhanced the migration of the deposited Ge atoms or dimers by growth interruption for 10 s after each deposited ML. Afterwards, the substrate temperature was quickly decreased, and the surface morphology was characterized *ex-situ* with a Digital Instruments atomic force microscope (AFM) in the tapping mode.

Results

Sample	A	B	C	D
Ge Coverage (ML)	0	2.6	4	5
Morphology	Faceted Inverted Pyramid	Corrugations Without Pyramid[1]	Corrugations With Pyramid[2]	Corrugations With Dome[3]

Tab. 1: Shows the morphological evolution in the samples with different Ge coverage.

[1] As exhibited in the AFM images in Fig. 1(a) and (b);
[2] As exhibited in the 3D model in Fig. 2;
[3] As exhibited in the AFM images Fig. 1(c) and (d);

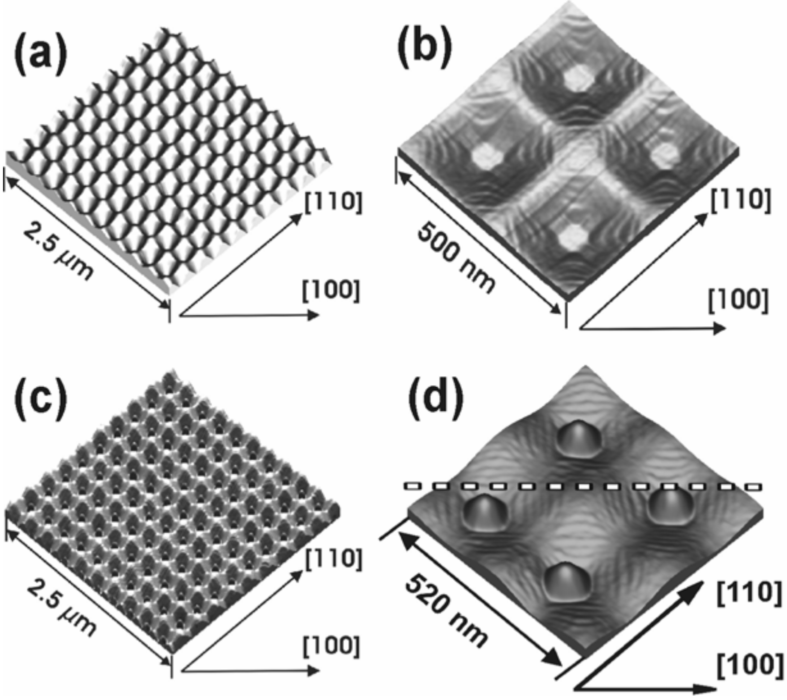

Fig. 1: AFM images in different scale for the pits after 2.6 ML Ge deposition [(a) and (b)]; after 5 ML Ge deposition [(c) and (d)], respectively..

The experiments showed that the initially forming Ge wetting layer develops a complex, but highly symmetric morphology on the inclined sidewalls of the pits [as described in Table 1].

This pattern is driven by strain- and surface energy minimization, and leads after the deposition of typically three monolayers of Ge to a conversion of the pit sidewalls into a pattern that consists exclusively of {105} and (001) facets. We attribute the subsequent islands nucleation to Ge accumulation at the bottom of the pits, which is driven by capillarity and the enhanced surface diffusion on the by now {105} faceted sidewalls of the pits. This complex interplay of mechanism in the confined geometry of the pits leads to preferential dot nucleation at the bottom of the pits despite the disadvantages of this site in terms of strain relaxation.

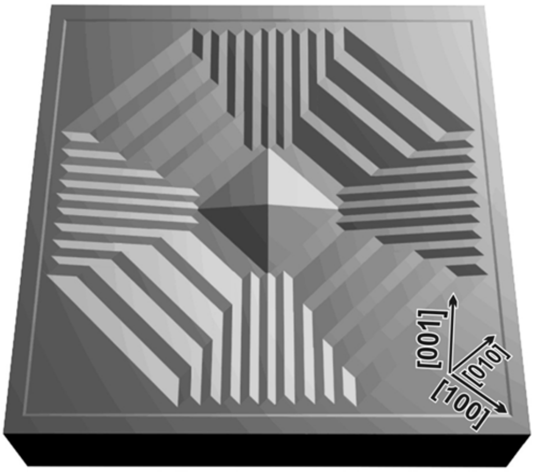

Fig. 2: Schematic 3D representation of the pit structure after the surface is converted into {105} and (001) facets. The central pyramid is pointing outwards. The 3D effect is seen best in the upper right corner.

Conclusion

The results show that SK growth in combination with nanostructured surfaces can be exploited for the implementation of perfectly ordered SiGe and Ge nanostructures that fulfill basic preconditions for meaningful device applications, namely addressability.

Acknowledgements

Valuable discussions with Z. Zhong are gratefully acknowledged. We thank H. Hoppe and G. Springholz for help with the AFM measurements. This work was financially supported by GMe (Vienna), FWF (Vienna) via Projects No.14684, No. 16631, No. 16223, and SFB 025, INTAS via Project No. 03-51-5015, as well as by EC Projects SANDIE, and D-DOTFET (EC012150).

References

[1] Z.Zhong et al., J. Appl. Phys. **93**, 6258 (2003).

[2] G. Chen, H. Lichtenberger, G. Bauer, W. Jantsch, and F. Schäffler, Phys. Rev. B **74**, 035302 (2006).

Sensors (Talks)

On-chip Cytometric Detection of Single Biological Cells Using Integrated Photodiodes

S. Kostner, M. J. Vellekoop

Institute of Sensor and Actuator Systems
Vienna University of Technology, Gusshausstrasse 27-29
1040 Wien

In this contribution we present the principle and measurement results on cytometric detection of single biological cells using integrated photodiodes. The sensing element is built into a microfluidic flow cell that allows for positioning the cells directly over the sensor. Additionally to results with calibrated polystyrene beads we show sensor readings for yeast cells. Experiments show that those cells actually act like lenses, focusing the incoming light to the sensor.

Introduction

Cytometry is a measurement process in which physical or (bio-) chemical information about single cells is obtained [1]. Several methods can be found in literature like optical and impedance based techniques which are used to determine parameters like cell size/shape, protein content, electric conductivity and viability. Measuring single cells yields statistical information from a given sample that is usually hidden when the sample is measured in suspension. For obtaining this statistical information tens of thousands of particles have to be measured in a relatively short time period (for instance 10^6 events/second).

A typical optical setup for flow cytometry consists of a light source, a test volume, and one or more sensing elements. Usually the reflected, transmitted and/or absorbed light fraction is of interest and can be related to a physical parameter of the test substance. Very often the relation between wanted parameters and physical sensor readings is found in an empiric way by experiment.

Using microfabrication techniques the volume of the test channel can be made small enough so that suspended objects like small particles or biological cells can be detected as single events. The natural limitation to the miniaturization of these optical systems is diffraction: the size range of particles and photosensitive area cannot be much smaller than the wavelength used.

Compared to other systems our approach for gaining optical information about the cells is different in the sense that we place the photosensitive element directly into the analysis channel, thus sensing in the optical near field of the particle. This allows for obtaining information about the particle that is usually hidden for systems that pick up the far field only (like FACS systems).

Sensor Design and Technology

In order to produce repeatable sensor readings it is necessary not only to have a proper sensor layout but also to have means to control how the particles are being delivered to the sensor. Therefore a flow cell was designed that provides position control in 3D for the particles that move over the sensor [2]. This is achieved by generating a non-coaxial sheath flow that can be controlled by applying different flow rates to the fluidic ports of the device.

Figure 1 shows the principle of the sensor that consists of a strip photodiode (2 µm x 50 µm) that is arranged perpendicular to the flow channel which has a width of 150 µm. The device is a sandwich consisting of a bottom silicon wafer (with the integrated photodiodes; 1 µm standard bipolar process) and a top glass slide which are bonded together by an intermediate SU-8 layer (height: 70 µm) forming the fluidic structure [3]. The through-holes for the fluidic connection of the chip were etched in Si from the bottom.

When a particle moves over the sensor a change in the photocurrent or voltage can be measured that is proportional to the shadow area produced by the particle [4].

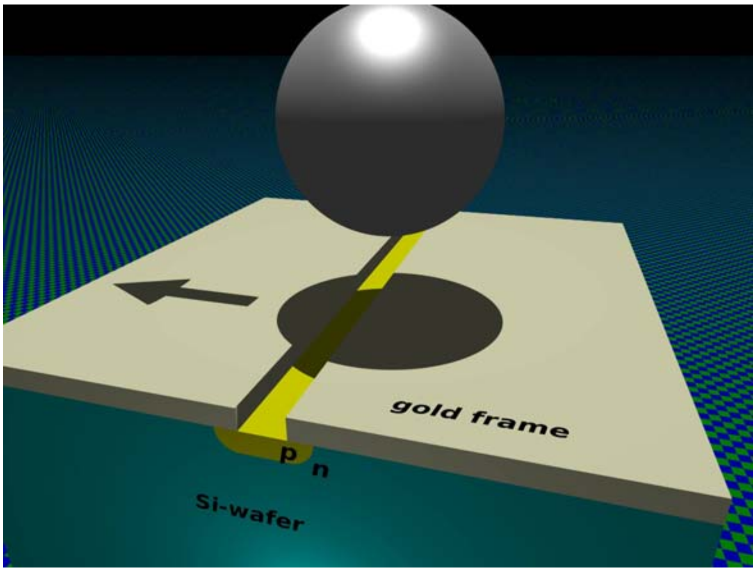

Fig. 1: Principle of the sensor with the integrated photodiodes. The arrow indicates the flow direction. The non-transparent particle produces a shadow on the light sensitive area which causes a signal drop.

Experimental Setup

The chip was clamped onto a custom made device holder that provides the electrical and fluidic connections. Syringe pumps with carefully chosen flow rates were used to apply a sheath flow to force the particles/cells closely over the photosensitive area. A modulated green laser source (592 nm, Roithner Lasertechnik GLMC1-10) was used to illuminate the chip from the top through the cover glass slice. The sensor signal (photodiodes in photovoltaic mode) was measured and demodulated with a lock in amplifier (Signal Recovery 7280). The demodulated signal was recorded with a digital storage oscilloscope. The whole setup was mounted on a solid construction in order to suppress vibrations in the optical path.

Results and Discussion

First experiments with polystyrene test particles of 20 µm and 24 µm diameter were carried out for the calibration of the sensor and published in [5]. In this contribution we show the use of the same system for the detection of yeast cells suspended in physiologic solution.

Figure 2 (left) shows sensor readings from experiments with polystyrene beads. The silver coated particles generate a negative pulse in voltage as expected since the shadow of the particle covers part of the photodiode. The transparent particles (plain polystyrene) show an increase in the sensor signal which can be explained by a “lens effect” where the particle actually focuses the light to a bright spot on the sensor area (Fig. 2 right).

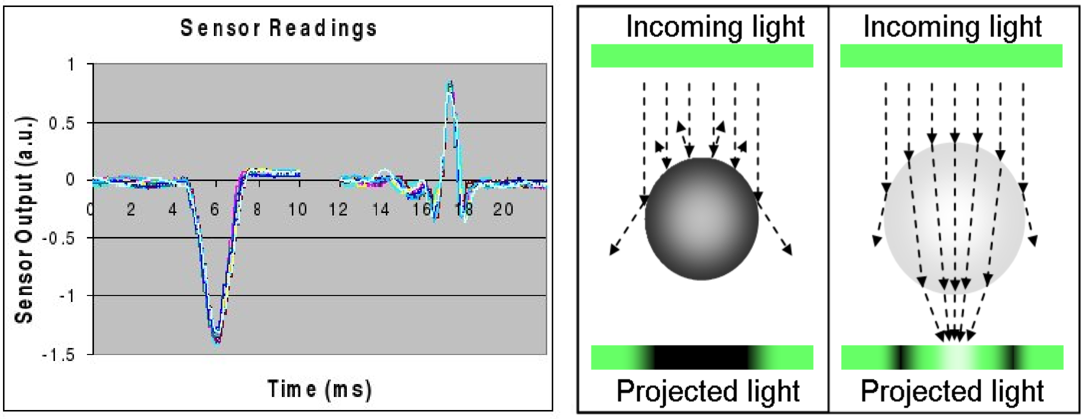

Fig. 2: Sensor readings from experiments with polystyrene beads (left). Silver coated particles cause a signal drop, while transparent plain particles show a signal increase. This behavior can be explained by a lens effect where a transparent particle focuses the incoming light to a bright spot, thus increasing the light intensity in the center of the projection (right) [5].

Because of this lens effect the intensity of the projected light depends on the height at which the particle passes the sensor. For repeatable results it is very important to keep this height constant.

With the polystyrene particle measurements as a reference, the sensor was now operated with suspended yeast cells. These measurements are more difficult because the cells are much smaller (about 3 – 5 µm diameter) and there is variation in some properties compared to calibration beads: the variation in size causes uncertainties, also the shape is not perfectly spherical and the surface is not well defined. As a result the focused beam has uncertainties in the focal length (caused by shape and size variation) and the intensity (absorption and diffraction at the irregular surface).

Measurement results are shown in Fig. 3. The cells are very well detectable but the SNR in the system is lower compared to measurements with the large polystyrene particles. Very interesting is the fact that those cells cause a positive peak which indicates their transparent character.

Conclusions

We have successfully demonstrated the optical detection of yeast cells in a projection cytometer. In our current setup we were able to detect particles down to the size of yeast cells with the sensor (photodiode) placed in the near field of the particle. Non-transparent particles produce a drop in the sensor signal as expected due to their shadow. In the case of (semi-) transparent particles an increased sensor signal was observed which is explained by a lens effect. Measurements with yeast cells showed a similar sensor output (positive peaks) which indicates their transparent character.

We conclude that this analysis method can be used to distinguish different types of cells by their optical transmission and absorption properties.

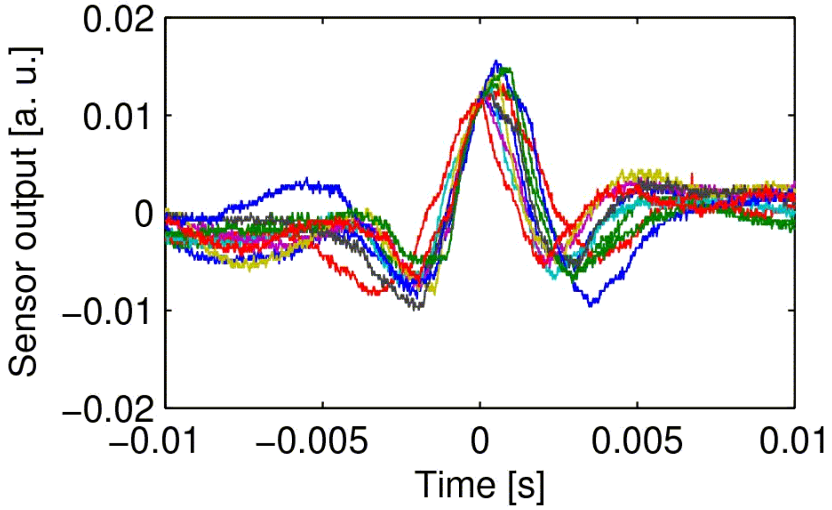

Fig. 3: Measurement results from experiments with yeast cells. The positive peak indicates the transparent character of the cells.

Acknowledgement

The chips were made in cooperation with the Delft University of Technology and co-funded by the Technologiestichting STW (project DPC.5521).

References

[1] H. M. Shapiro, “Practical Flow Cytometry”, 4th ed., 2003, Wiley & Sons

[2] J.H. Nieuwenhuis, J. Bastemeijer, P.M. Sarro, and M.J. Vellekoop, “Integrated Flow-Cells for Novel Adjustable Sheath flows”, Lab on a Chip, vol. 3, pp.56-61, 2003

[3] P. Svasek, E. Svasek, B. Lendl, and M. Vellekoop, “Fabrication of miniaturized fluidic devices using SU-8 based lithography and low temperature wafer bonding”, Sensors and Actuators A, vol. 115, pp. 591-599, 2004

[4] J.H. Nieuwenhuis, J. Bastemeijer, A. Bossche, and M.J. Vellekoop, “Near-Field Optical Sensors for Particle Shape Measurements”, IEEE Sensors Journal, vol. 3, pp. 646-651, 2003

[5] J.H. Nieuwenhuis, P. Svasek, P.M. Sarro, and M.J. Vellekoop, “Particle Discrimination with an Improved Projection Cytometer”, Proc. of µTAS 2004, Malmö, Sweden

Optoelectronics (Posters)

Dislocation-Free GaN/AlGaN Double-Barrier Diodes Grown on Bulk GaN

S. Golka, G. Pozzovivo, W. Schrenk, G. Strasser, C. Skierbiszewski, M. Siekacz, I. Grzegory, S. Porowski

Zentrum für Mikro- und Nanostrukturen, TU Wien,
Floragasse 7, A-1040 Vienna, Austria

Introduction

Integrated resonant tunneling diodes (RTDs) are interesting devices for a number of applications, such as ultrafast switches or as components in HF oscillators. The last might be particularly interesting in the GaN/AlGaN system due to its high power handling capability and availability of well performing GaN HEMTs at elevated temperature.

While AlGaN quantum cascade electro-optic devices recently received particular interest, the behavior of such vertical devices is not well understood and their performance greatly lags behind that of horizontal devices. The RTD is a benchmark for any such quantum cascade/intersubband (ISB) device. While epitaxial quality of InGaN/AlGaN could be improved so far that blue laser diodes became possible, the fabrication of RTDs still suffers from instabilities that relate to the large defect density near such heterostructures.

Other ISB devices such as detectors could be realized already. A clear relationship between energetic levels of QW states and the continuum was established by ISB absorption and photovoltage [1] experiments. At the same time results obtained for resonant tunneling [2] are still very scarce and controversial [3]. The observed current-voltage (IV) characteristics exhibited a negative differential resistance (NDR), but only on one-sided and not reproducible. This is likely to be at least partly due to conduction over dislocations [4]. However the recent availability of high pressure grown bulk samples [5] makes fabrication of dislocation free RTDs possible [6].

Experimental

Dislocation free mesas were achieved with the low dislocation density ($10^2\,\mathrm{cm}^{-2}$) of bulk substrates and fabrication of single diodes of 6 µm diameter, which is much smaller than in previous studies (40 µm Ref. [2] and 100 µm Ref. [3])

The epitaxial structure was grown by plasma assisted molecular beam epitaxy (PAMBE). On top of a template overgrown by 1 µm of a metal organic chemical vapor deposition (MOVPE) GaN:Si layer the following structure was deposited (starting at substrate): GaN:Si – $Al_{0.7}Ga_{0.3}N$ – GaN - $Al_{0.7}Ga_{0.3}N$ –GaN:Si. Layer thicknesses were 150 – 2 – 2 – 2 – 100 nm respectively. Calculating this structure with a self-consistent Schrödinger-Poisson solver, not taking into account transport, the QW ground state is 0.6 eV above the Fermi level.

Mesas (Fig. 1) were defined by standard UV contact lithography. The irregular and small shape of the bulk samples was overcome by spray coating of 2 µm photoresist. Mesas were then etched in an inductively coupled plasma reactive ion etcher (ICP-RIE) with $SiCl_4$ chemistry. SiN_x (300 nm) was deposited with 300°C plasma enhanced chemical vapor deposition (PECVD) and opened with SF_6 RIE. Evaporated Ti – Al – Ni

– Au (10 – 150 – 35 – 200 nm) annealed at 580°C for 30 s serves as the top contact. Annealing was limited by the thermal resistance/adhesion of the SiN_x.

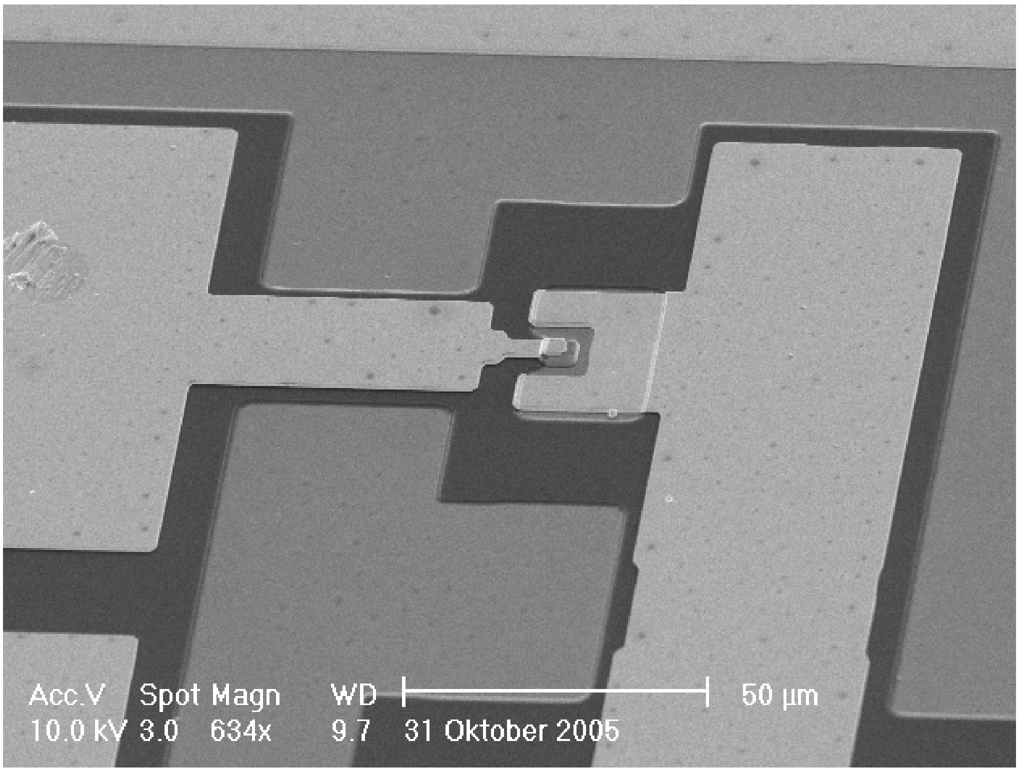

Fig. 1: SEM image of fully processed device with 6 µm diameter and separate bottom contact

Results

Like in studies published earlier [2] we see a fundamental and abrupt change in the IV curve between the first trace on a virgin mesa and the subsequent retrace or any further trace leaving only the exponential background. Contrary, the NDR (seen in 20% of all devices) our IVs consist of multiple data points. The asymmetry in the IVs (voltage applied to top contact) stems partially from the internal polarization fields and partly from the difference between a good ohmic back contact and a Schottky-like top contact. No direct relationship between measurement conditions and shape/position of the NDR has been observed. However, position of the NDR varies randomly between different devices within limits (Fig. 2). The ‘hysteresis’ that causes this decay is described in more detail in [6].

While in principle a degradation or breakdown of the material could be responsible for such decay, especially concerning the high peak current density in the 10 kA/cm2 range, the same observations in pulsed mode with low duty cycle contradict that assumption.

The position and magnitude of NDR depends mainly on the greatest (previously) applied voltage. After decay the NDR can be restored partly (Fig. 3) by thermal treatment. Such behavior can be explained by a combination of tunneling and electron trapping effects.

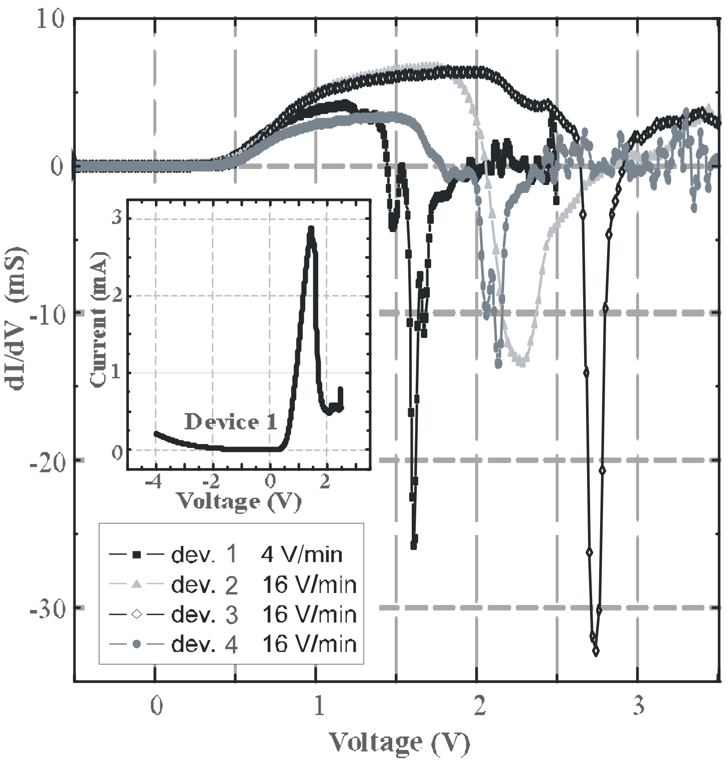

Fig. 2: Differential conductivity dI/dV of four devices all with 6 μm diameter measured at RT. *Inset:* Original IV of device 1.

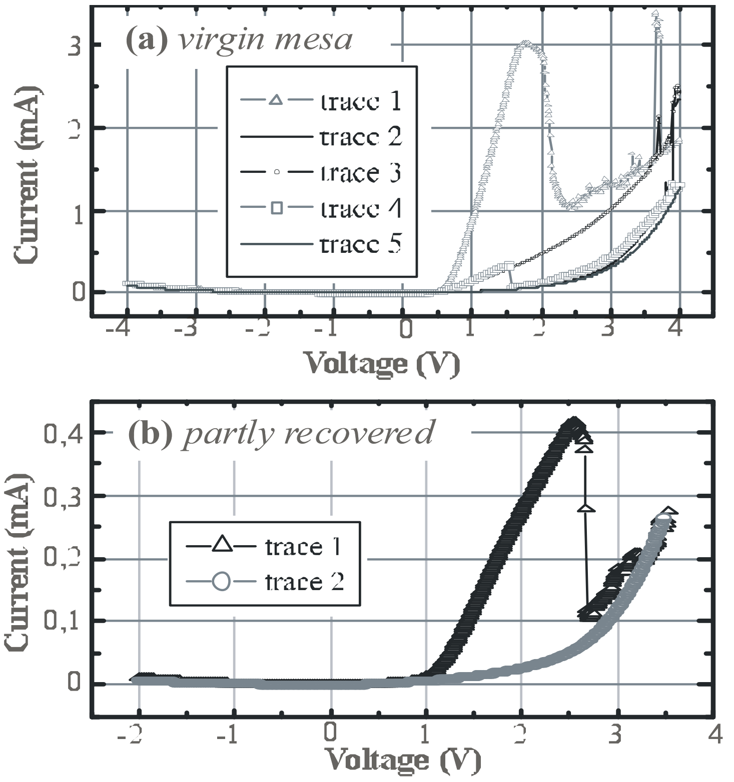

Fig. 3: IV characteristic of a device with d = 6 μm (a) before and (b) after annealing at 350°C in a RTA oven under N_2 atmosphere.

Conclusion

We have shown smooth IVs exhibiting NDR in a voltage interval of ~0.3 V, located in the range 1.2…2.8 V of a GaN based RTD. Decay of this NDR feature after a first measurement and possible recovery by thermal treatment were related to deep electron traps and consequent deformation of the conduction band profile in the double barrier region.

We acknowledge the support by the EU STREP project NITWAVE, the “Gesellschaft für Mikro- und Nanoelektronik” (GMe), and the MNA network.

References

[1] E. Baumann, F. R. Giorgetta, D. Hofstetter, H. Lu, X. Chen, W. J. Scha, L. F. Eastman, S. Golka, W. Schrenk, and G. Strasser, Appl. Phys. Lett. 87, 191102 (2005)

[2] Kikuchi, R. Bannai, K. Kishino, C.-M. Lee, and J.-I. Chyi, Appl. Phys. Lett. 81, 1729 (2002)

[3] E. Belyaev, C.T. Foxon, S.V. Novikov, O. Makarovsky, L. Eaves, M.J. Kappers, and C.J. Humphreys, Appl. Phys. Lett. 83, 3626 (2003)

[4] J.W.P. Hsu, M.J. Manfra, R.J. Molnar, B. Heying, and J.S. Speck, Appl. Phys. Lett. 81, 79 (2002)

[5] C. Skierbiszewski, K. Dybko, W. Knap, M. Siekacz, W. Krupczynski, G. Nowak, M. Bockowski, J. Lusakowski, Z. R. Wasilewski, D. Maude, T. Suski, and S. Porowski, Appl. Phys. Lett. 86, 102106 (2005)

[6] S. Golka, C. Pflügl, W. Schrenk, G. Strasser, C. Skierbiszewski, M. Siekacz, I. Grzegory, and S. Porowski, Appl. Phys. Lett. 88, 172106 (2006)

Second-Harmonic Emission from Quantum Cascade Lasers

M. Austerer, S. Schartner, M. Nobile, W. Schrenk, A. M. Andrews, T. Roch, G. Strasser

Zentrum für Mikro- und Nanostrukturen, TU Wien,
Floragasse 7, A-1040 Vienna, Austria

Introduction

The mid-infrared spectral region can be covered by quantum cascade (QC) semiconductor lasers, where the emission wavelength is tailored by bandstructure engineering. For a detailed review on QC lasers see Ref. [1]. Their emission energy is well below the band gaps of the hosting material system. Typical GaAs QC lasers operate in the mid-infrared regime with corresponding energies of ~100 meV, whereas the GaAs band gap is around 1.4 eV. That makes frequency-doubling inside the laser cavity feasible. Such intracavity second-harmonic (SH) generation is not possible in interband semiconductor lasers, where the SH radiation is strongly absorbed. The principle of nonlinear light generation in QC lasers was firstly demonstrated in 2003 [2], since then a lot of progress in this field has been made, such as the improvement of SH generation [3] and the demonstration of third-harmonic generation [4]. A crucial step was the achievement of phase-matching [5], [6], which was demonstrated by means of modal phase-matching in InP-based QC lasers. Another approach for higher conversion efficiencies is quasi phase-matching by periodically modulating the pump current along the QC laser ridge waveguide [7]. Besides up-conversion, other intracavity nonlinear effects are currently being investigated, such as Raman lasing [8] and anti-stokes [9] emission from QC lasers. The above nonlinear effects are due to higher-order susceptibilities of intersubband transitions. Although InP and GaAs, both of which are commonly used as host materials for QC lasers, have nonzero second-order susceptibilities, there is no resulting second-order polarization in the material for QC lasers. That is due to selection rules for intersubband transitions which allow gain only for TM polarized light, which in turn due to crystal symmetry cannot excite nonlinear polarization in the host material. However it was shown that QC lasers grown on $\langle 111 \rangle$ substrates, show sum-frequency generation due to bulk nonlinearity [10].

Bandstructure Engineering and Results

We have investigated second-harmonic and sum-frequency generation in three-well and bound-to-continuum GaAs based QC lasers. The discussed structures are regrowths of structures presented in Ref. [11] and [12] respectively. The second-harmonic generation in these samples is due to intersubband nonlinearities in the active regions of these devices. The optimization of QC active regions for intracavity second-harmonic generation is always jeopardized by the linear absorption that corrupts the laser operation at the fundamental frequency. However, three-well and bound-to-continuum active regions always have higher lying states that can resonantly enhance the second-order susceptibility of the respective QC active region.

The bandstructures discussed in this paper for the GaAs/AlGaAs material system are similar to the structures used for the InGaAs/InAlAs system. However the

GaAs/AlGaAs system offers the advantage of lattice matching for arbitrary $Al_xGa_{1-x}As$ alloy compositions. The highest Γ-valley conduction band offset can thus be reached for AlAs barriers. AlAs barriers have already been used in the past to improve the performance of QC lasers [13] – [15].

Our structure A uses AlAs barriers in the active region to design resonant intersubband transitions to generate frequency doubled light [16]. The Γ-valley conduction band edge of structure A together with the moduli squared of the relevant wavefunctions is shown in Fig. 1. The portion shown is similar to a typical three-well [11] QC active region, but with four AlAs barriers. The AlGaAs barriers in the injector regions have 45% Al-content. The wavefunctions are calculated in an effective mass approximation, where band non-parabolicity is taken into account by an energy-dependent effective mass. The lasing transition between levels 3 and 2 is calculated to an energy of 117 meV with a matrix element of z_{32} = 1.53 nm. Important nonlinear cascades are the level triplets 2–3–5a, 2–3–5b and 2–3–5c. To estimate the second-order susceptibility all three levels (2, 3, 5) have to be considered.

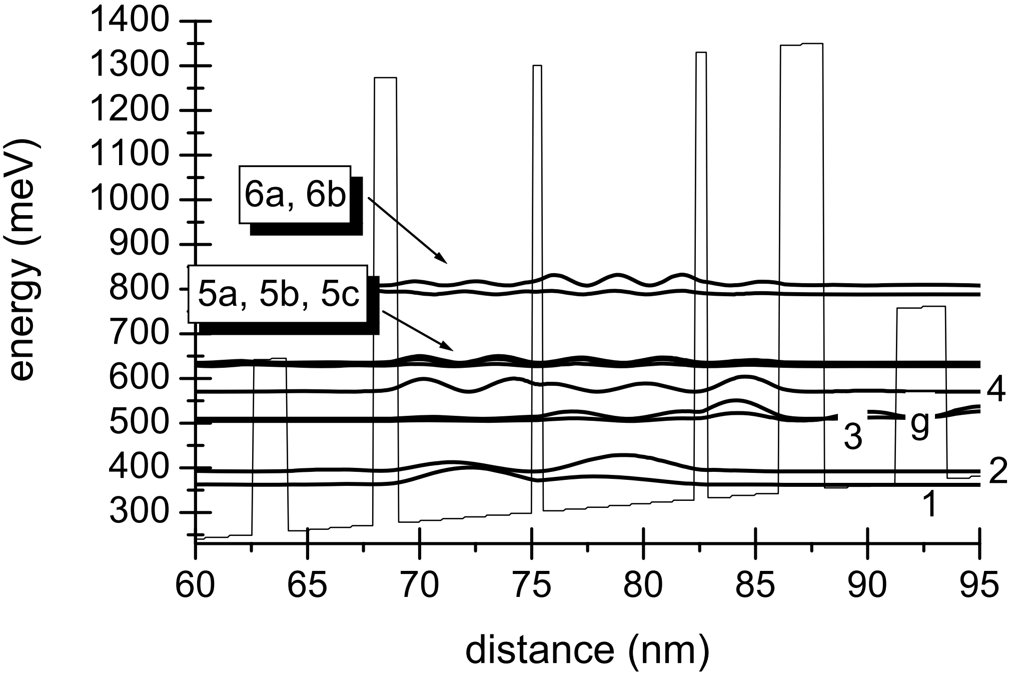

Fig. 1: Conduction band diagram and moduli squared of relevant wavefunctions in the active region of structure A. Important energy levels are labeled “1” through “6” for the active cell and “g” for the injector ground state. The layer thicknesses in nanometers for the GaAs quantum wells and AlAs barriers (italic type) from left to right *1.1*, 6, *0.5*, 6.8, *0.5*, 3.3, *1.9*; The injector bridging regions consist of $GaAs/Al_{0.45}Ga_{0.55}As$ superlattices.

Apart from the QC structure with AlAs barriers in the active region, we also investigated active regions with three-well (structure T) and bound-to-continuum (structure B) active regions, where all the barriers consisted of AlGaAs with 45% Al-content. The bandstructures and moduli squared of the wavefunctions for these structures are plotted in Fig. 2. The lasing transition takes place between states 3 and 2. For a detailed description of the laser properties on the fundamental wavelength please refer to references [11] and [12].

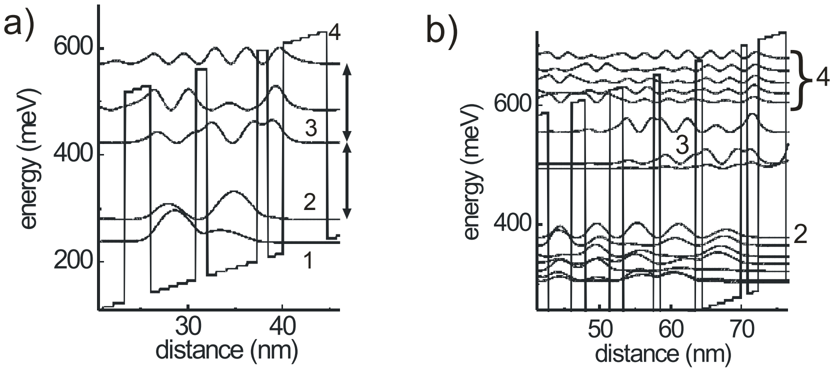

Fig. 2 Portions of the conduction band diagram and the moduli squared wavefunctions of structures a) T and b) B. The most important wavefunctions are labeled 1, 2, 3 and 4. Their functions are described in the text.

So far, SFG was only reported for three-well and two-well design active region QCLs [2], [3], [16]. We demonstrate structure B, where the situation differs qualitatively from these devices. Because the active region of the bound-to-continuum design consists of a superlattice with a thin pre-well, more states significantly contribute to sum-frequency generation. The calculated matrix elements between the involved states (2–4 and 3–4) are in the range of several Å. A feature of this structure, which was already discussed in ref. [12], is the high threshold current density. One reason for this is the strong linear resonant absorption in the active region. In this structure for lower applied fields (<35 kV/cm) the upper states are bound and thus the losses caused by linear absorption are too high to achieve lasing for the fundamental transition 3–2. However, if the electric field is increased these states are shifted towards the border of the barriers, lasing starts and because the states are still close to resonance a high second-order susceptibility is achieved, which leads to efficient sum-frequency generation in these devices.

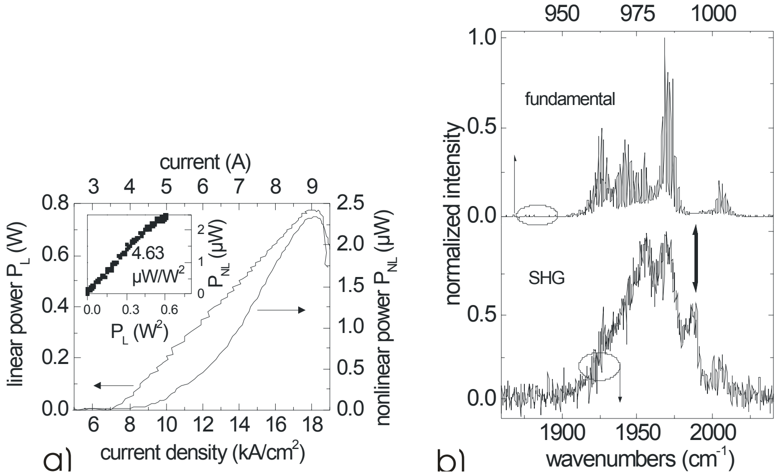

Fig. 3 Light output vs. current characteristics (a) of structure A and the corresponding spectra (b). The sum-frequency signal at 1980 cm^{-1} is indicated by the double-headed arrow.

The fundamental and nonlinear output powers of structure A as a function of drive current are shown in Fig. 3(a). The quadratic dependence of the nonlinear power on the linear power can be clearly seen. When the nonlinear power is plotted as a function of the fundamental power squared, a linear function is obtained with a slope of ~5 $\mu W/W^2$ (see inset of Fig. 3(a)). In the spectra (Fig. 3(b)) we observe not only the frequency-doubled signal, but also a sum-frequency signal at ~1980 cm^{-1}, which arises from the two distinct Fabry-Perot combs at 980 cm^{-1} and 1000 cm^{-1}.

The bound-to-continuum active region shows the best conversion efficiency, possibly due to the multitude of upper states in the nonlinear cascade. Both the three-well designs with AlGaAs and AlAs barriers show approximately the same conversion efficiency, so there is no significant advantage with the additional barrier height provided by the AlAs material.

References

[1] C. Gmachl, F. Capasso, D. L. Sivco, and A. Y.Cho, Rep. Prog. Phys. 64, 1533 (2001)

[2] N. Owschimikow, C. Gmachl, A. Belyanin, V. Kocharovsky, D. L. Sivco, R. Colombelli, F. Capasso, and A. Y. Cho, Phys. Rev. Lett. 90, 043902 (2003)

[3] C. Gmachl, A. Belyanin, D. L. Sivco, M. L. Peabody, N. Owschimikow, A. M. Sergent, F. Capasso, and A. Y. Cho, IEEE J. Quantum Electron. 39, 1345 (2003)

[4] T. S. Mosely, A. Belyanin, C. Gmachl, D. L. Sivco, M. L. Peabody, and A.Y Cho, Opt. Express 12, 2976 (2004)

[5] O. Malis, A. Belyanin, D. L.Sivco, M. L. Peabody, A. M. Sergent and A. Y. Cho, Appl. Phys. Lett. 84, 2721 (2004)

[6] O. Malis, A. Belyanin, D. L. Sivco, J. Chen, A.M. Sergent, C. Gmachl and A. Y. Cho, Electron. Lett. 40, 1586 (2004)

[7] M. A. Belkin, M. Troccoli, L. Diehl, F. Capasso, A. Belyanin, and D. L. Sivco, in Conference on Lasers and Electro-Optics/Quantum Electronics (Optical Society of America, Washington, DC, 2005), QPDA1

[8] M. Troccoli, A. Belyanin, F. Capasso, E. Cubukcu, D. L. Sivco and A.Y. Cho, Nature 433, 845 (2005)

[9] H. Page, C. Becker, A. Robertson, G. Glastre, V. Ortiz, and C. Sirtori, Appl. Phys. Lett. 78, 3529 (2001)

[10] J.-Y. Bengloan, A. DeRossi, V. Ortiz, X. Marcadet, M. Calligaro, I. Maurin, and C. Sirtori, Appl. Phys. Lett. 84, 2019 (2004)

[11] H. Page, C. Becker, A. Robertson, G. Glastre, V. Ortiz, and C. Sirtori, Appl. Phys. Lett. 78, 3529 (2001)

[12] C. Pflügl, W. Schrenk, S. Anders, G. Strasser, C. Becker, C. Sirtori, Y. Bonetti, and A. Muller, Appl. Phys. Lett. 83, 4698 (2003)

[13] L. R. Wilson, D. A.Carder, J. W. Cockburn, R. P. Green, D. G. Revin, M. J. Steer, M. Hopkinson, G. Hill, and R. Airey, Appl. Phys. Lett. 81, 1378 (2002)

[14] M. P. Semtsiv, M. Ziegler, S. Dressler, T.W. Masselink, N. Georgiev, T. Dekorsky, and M. Helm, Appl. Phys. Lett. 85, 1478 (2004)

[15] W. Schrenk, N. Finger, S. Gianordoli, E. Gornik, and G. Strasser, Appl. Phys. Lett. 77, 3328 (2000)

[16] C. Pflügl, M. Austerer, W. Schrenk, and G. Strasser, Electron. Lett. 41, 1331 (2005)

Far Field Investigations on Quantum Cascade Lasers

S. Schartner, M. Austerer, M. Nobile, S. Golka A. M. Andrews, W. Schrenk, G. Strasser

Zentrum für Mikro- und Nanostrukturen, TU Wien,
Floragasse 7, A-1040 Wien

Introduction

Quantum cascade lasers (QCLs) are unipolar semiconductor lasers operating in the mid infrared region. Their emitted wavelength is defined by the separation of intersubband levels which can be tailored by band structure engineering. Due to the fact that the maximum conduction band offset in the GaAs/AlGaAs material system is 380 meV, the lowest directly accessible wavelength is roughly 7 µm. One way to reach lower wavelengths is to use intracavity nonlinearities. With sum frequency (SF) generation or second harmonic (SH) generation respectively it is possible to cover the spectroscopically important band between 3.5 µm and 7 µm. Unlike conventional interband semiconductor lasers QCLs do not suffer from the problem of strong absorption of the frequency doubled light because the emission energies (100 – 300 meV) are well below the band gap of the hosting GaAs (E_{Gap} = 1.4 eV).

Although GaAs has a nonzero second-order susceptibility, there is no resulting second-order polarization for standard QCLs. This is due to the selection rules for intersubband transitions which allow gain only for TM polarized light, which in turn due to crystal symmetry together with the typical <100> growth direction cannot excite nonlinear polarization in the host material. However it was shown that QCLs grown on <111> substrates show sum-frequency generation due to bulk nonlinearity [1]. In our approach we instead use active region designs that include a nonlinear cascade [2], [3]. These artificial nonlinear susceptibilities can reach values comparable to those for the bulk material. The principle of nonlinear light generation in QCLs was actually firstly demonstrated using this intersubband approach in 2003 with the InP material system [4].

Another very interesting topic is intracavity difference-frequency generation in QCLs. It could eventually be used to generate coherent THz radiation in a semiconductor laser at room temperature. Recently THz sideband generation from a THz QCL and a near-infrared diode laser has been shown [5].

An important issue with intracavity SH generation is the optimization of the waveguide for both fundamental and SH frequencies. We show how a double AlGaAs waveguide helps to improve the conversion efficiency compared to a conventional double-plasmon waveguide as used in GaAs based QCLs. We present farfield measurements of the fundamental laser mode and the SH emission that will help investigating modal phase-matching conditions.

Waveguide Design

The nonlinear susceptibility itself is optimized by means of band structure engineering. The external linear to nonlinear conversion efficiency however depends additionally on the waveguide used. Issues like losses, modal overlap and phase-matching have to be considered. Originally the nonlinear active regions were all embedded in a symmetric double-plasmon waveguide that consists of a low-doped core region (GaAs, n_{Si} = $3x10^{16}$ cm^{-3}) and highly-doped cladding layers (GaAs, n_{Si} = $4x10^{18}$ cm^{-3}) (compare Fig. 1(a)). This waveguide is optimized for fundamental laser action using the dramatic drop in refractive index near the plasma frequency for confinement. However, the strong dispersion near the plasma frequency cannot provide satisfactory confinement for the fundamental and SH radiation at the same time. Figure 1(b) is illustrating this fact: a doping level leading to a refractive index sufficient to confine the fundamental mode does not yield in a sufficiently low refractive index for the SH mode. The calculated refractive index for the ~ 5 µm light in the active region is 3.24, whereas it is only 3.14 in the cladding layers. This results in low confinement of the frequency doubled light. Hence, the losses are high, the overlap to the active region is poor and so is the overlap with the fundamental mode. Additionally the refractive indices of the fundamental and the SH light differ strongly and phase-matching cannot be achieved using this kind of waveguide.

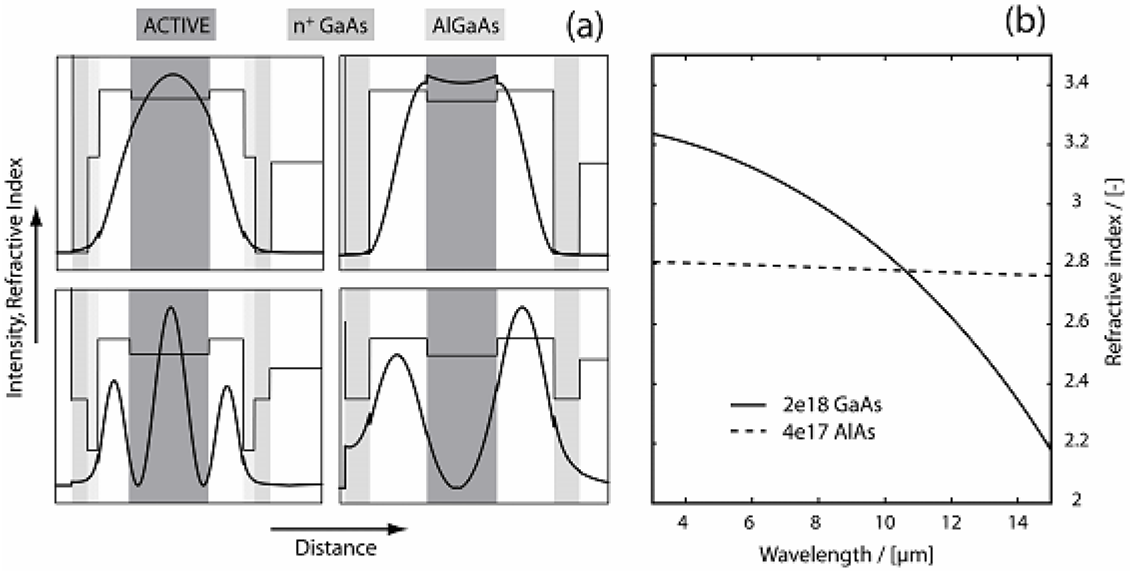

Fig. 1: (a) Mode profiles of the fundamental (upper) and SH (lower) and the line up of the real part of the refractive index are shown for a double-plasmon (right) and a double-AlGaAs (left) waveguide. The combination of a medium doped AlGaAs and a highly doped GaAs layer provides good confinement for both frequencies. (b) The real part of the refractive index calculated with the Drude model for n^+ GaAs and n AlAs.

A waveguide design which substitutes part of the plasmonic cladding with highly Al containing layers can help with these problems. As shown in Fig. 1(a) the fundamental mode is still confined by the thinner n^+ GaAs layer but with support from the AlGaAs spacers. This can even decrease the losses due to the reduced free carrier absorption. However, for the SH mode the AlGaAs actually plays the role of a cladding layer.

Two devices were grown and processed to Fabry-Perot lasers. A bound-to-continuum active region design was embedded in a double $Al_{0.9}Ga_{0.1}As$ waveguide ($n_{(5µm)}$ = 2.86). The layer sequences are 0.3 µm GaAs (n_{Si} = $4x10^{18}$ cm^{-3}), 0.7 µm $Al_{0.9}Ga_{0.1}As$ (n_S = $2.4x10^{17}$ cm^{-3}), 2 µm GaAs (n_{Si} = $4x10^{16}$ cm^{-3}), 60 cascades of bound-to-continuum active cells, 2.2 µm GaAs (n_{Si} = $4x10^{16}$ cm^{-3}), 0.7 µm $Al_{0.9}Ga_{0.1}As$ (n_{Si} = $2.4x10^{17}$ cm^{-3}), 1 µm GaAs (n_{Si} = $4x10^{18}$ cm^{-3}) and n-type GaAs substrate. For this structure we calculate refractive effective indices of 3.185 (fundamental, TM_{00}) and 3.181 (nonlinear light,

TM_{02}). This was calculated for an infinitely wide laser ridge. Using a SiN_x insulation and gold at the side walls, a ridge width dependent fine tuning of the refractive index is possible and phase matching is calculated to occur for laser ridges around 25 µm thickness. This structure further strongly increases the confinement factor, especially for the nonlinear light, where it is increased from 17% to 65%. Besides the improvement in confinement, this waveguide also enhances the overlap of fundamental and nonlinear light.

Results

Depending on the ridge width we were able to increase the conversion efficiency from approximately 15 to 100 $\mu W/W^2$ and achieve nonlinear peak powers exceeding 100 µW. This improved performance is due to a higher confinement and lower losses for the SH light. According to our calculations the overall refractive index difference between the fundamental and SH is also reduced, and it might be possible to achieve modal phase matching in such a waveguide. As shown in Fig. 2 we observe a maximum conversion efficiency of 120 $\mu W/W^2$ for 30 µm wide devices.

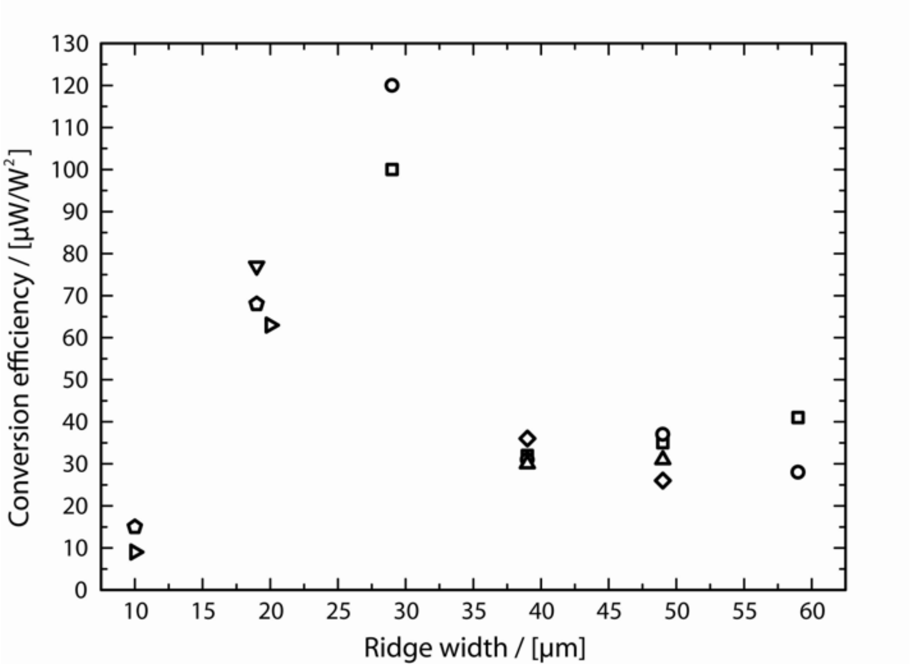

Fig. 2: Conversion efficiencies for lasers of different ridge widths. The conversion efficiency increases starting from thin ridges and falls again after it reaches a maximum around 30 µm. Modal phase matching is calculated to occur for 25 µm wide laser cavities.

To investigate the mode profiles in the laser waveguide we were analyzing their farfields. Fig. 3(a) shows a typical farfield profile of a TM_{00} mode which we observed up to ridge widths of 60 µm for the fundamental light. We attribute this to the lossy SiN_x insulation layer which suppresses higher-order lateral modes. This in turn is not the case for the SH radiation as the waveguide dimensions are roughly scaled by a factor of two, and the SiN_x losses are lower. The two-fold pattern of the SH farfield (Fig. 3(b)) in lateral direction can therefore be explained by a higher-order lateral mode. In growth direction the farfield is split in three lobes of comparable intensity. This pattern cannot be explained by solely one TM_{02} mode, but rather suggests a superposition of at least two modes (TM_{00} and TM_{02}).

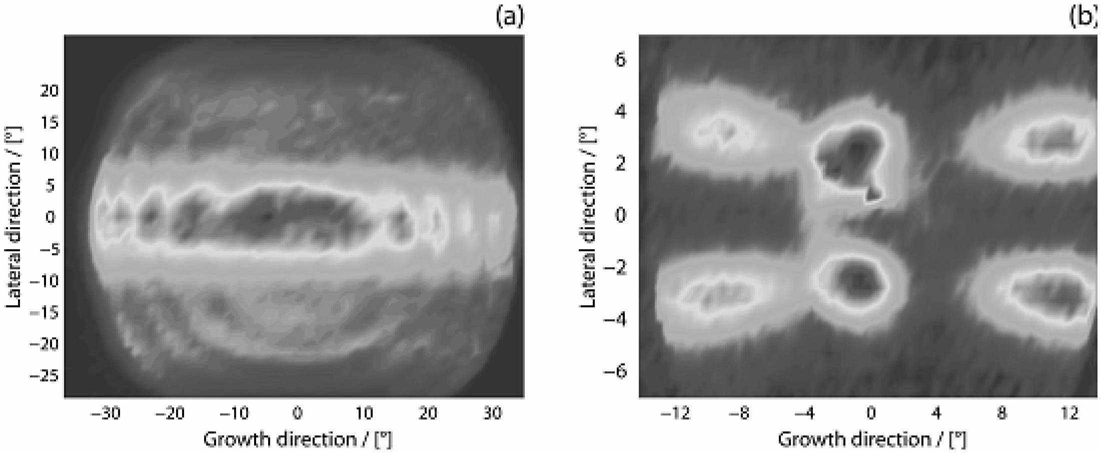

Fig. 3: Farfield profiles of the fundamental (a) and SH (b) modes for a 40 µm wide Fabry-Perot device with double AlGaAs waveguide. The plots were recorded at distances of 100 mm and 50 mm respectively.

Conclusion

We have shown that second-harmonic and sum-frequency emission in GaAs based QCLs grown on <100> substrates can be significantly enhanced with a double AlGaAs waveguide. In order to fully exploit the nonlinear properties of GaAs based QCL structures, appropriate waveguide designs that enable phase matching have to be developed. To reach this goal we performed farfield measurements that allow us insight into the SH modal behavior. Future goals include further enhancement of SH generation and the demonstration of difference-frequency generation.

References

[1] J.-Y. Bengloan et al., Appl. Phys. Lett. 84, 2019 (2004)

[2] C. Pflügl et al., Electron. Lett. 41, 1331 (2005)

[3] C. Pflügl et al., Appl. Phys. B 85, 231 (2006)

[4] N. Owschimikow et al., Phys. Rev. Lett. 90, 043902 (2003)

[5] S.S. Dhillon et al., Appl. Phys. Lett 87, 071101 (2005)

Optimization of MBE Growth Parameters for GaAs-based THz Quantum Cascade Lasers

A.M. Andrews[1,2], T. Roch[2], A. Benz[1], G. Fasching[1], W. Schrenk[2],
K. Unterrainer[1], G. Strasser[2]

[1] Institut für Photonik,
[2] Institut für Festkörperelektronik und Zentrum für Mikro- und Nanostrukturen,
Technical University of Vienna, A-1040 Wien

Introduction

Solid state terahertz (THz) lasers were made possible through the rapid progress in quantum cascade lasers (QCLs) [1]. Despite the advances in mid-infrared (MIR) QCLs [2], THz QCLs remain difficult to fabricate. The tolerances in alloy composition, layer thickness, and doping are lower for THz QCLs than their MIR counterparts. Typical THz structures can require more than a day to grow by MBE and a thickness change of a few percent will result in a non-lasing device.

In our QCL active region design, we use the phonon depletion scheme, shown in Fig. 1, to quickly depopulate the lower lasing level [3], to produce THz lasers that work above the critical liquid nitrogen temperature.

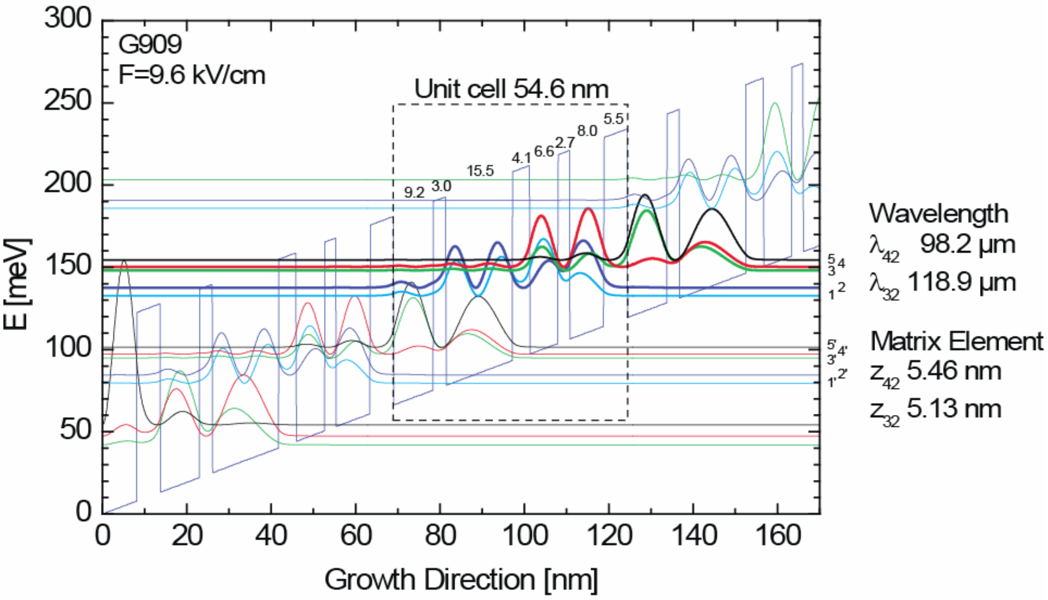

Fig. 1: Schematic of the conduction band structure (GaAs and $Al_{0.15}Ga_{0.85}As$) and electron wave functions in one unit cell of a 15 µm THz QCL active region with 271 cascade periods. This dual-wavelength design, 98.2 and 118.9 µm, results from the laser transitions from level 4 to 2 and 3 to 2. The rapid transition from level 1 to 5' emits one LO phonon.

Experiment and Results

The GaAs-based THz structures [4] were grown by solid-source molecular-beam epitaxy (MBE) in a modular GEN II. The MBE system has a vertical wagon wheel source configuration with four upward and four downward facing cells. Samples were grown on semi-insulating 3-inch GaAs substrates. Typical growth conditions used were substrate temperatures between 590 – 610°C with an As_4 pressure of $8x10^{-6}$ Torr. Original configuration, A, for the system was AC power supplies for all sources with the dual-filament Ga cell in the most upward facing position and the conical Al cell in the least upward facing position, approximately 90° from the Ga cell. The final configuration, B; uses a DC power supply for the Ga and exchanges the conical Al cell with a SUMO Al cell.

Due to the relatively low thickness tolerances, careful attention to growth conditions and their effect on wafer uniformity must be measured. Growth rate calibrations were first determined by reflected high energy electron diffraction (RHEED) oscillations and then further refined by the growth of either a singe superlattice or double superlattice measure *ex-situ* by high resolution x-ray diffraction (XRD). Shutter operations change the heat load of individual sources required to maintain specific cell temperatures by reflecting heat back into the cell. For example, the Ga cell initial growth rate upon opening the shutter was determined to be -10% of the steady state growth rate with a characteristic decay time of around 15 seconds. A second source of thickness error comes into account when growing 10 – 15 µm structures, and that is source material depletion. Due to the relatively low Al content of 15%, only the Ga depletion needs to be determined. By growing a growth rate calibration before and after the THz structure, the Ga depletion was measured to be 1% for every 10 µm of growth.

Due to the orientation of the sources, a non-rotated sample results in a thickness gradient of the desired thickness of +19% at the leading edge of the substrate to -21% at the trailing edge of the substrate for each source. This was confirmed by XRD for the growth of a non-rotated superlattice. Rotating the sample creates a more even thickness distribution across the wafer with a minimum every half rotation. After four rotations per epilayer, the average thickness error is slightly less than -1% at the edge. The total growth rate should be adjusted accordingly to maximize the usable area of the wafer when using epilayers on the order of a few or fractional monolayers.

N-type doping calibrations in the 10^{15} – 10^{16} cm^{-3} range are critical for THz QCLs, so a 4 µm Si-doped GaAs layer is grown on a semi-insulating $Al_xGa_{1-x}As$ barrier and GaAs substrate for each calibration. After 3 – 5 samples are measured, this produces reliable doping profiles with a 10% error.

Initial THz structures were grown with system configuration A, which produced broad peaks in XRD due to poor Ga flux stability, poor reproducibility, and no lasing devices. Two steps were taken to improve the THz structures: a switch to MBE configuration B along with the removal of Ga shutter operations, therefore no growth interrupts. This minimizes the flux variations for both thin layers and for long growths by using the dominant cell (Ga in this case) in steady state. The results are seen in the (002) XRD scan in Fig. 2. A 15 µm active region with 271 cascade periods is reproduced faithfully and what appear to be peak splitting, often seen in unstable long growths, are actually the diffraction peaks from the designed structure.

Table 1 summarizes the performance characteristics of the first four THz laser structures. The original 10-µm structure, 177 cascades, was designed to utilize both a surface plasmon and a double metal [5] waveguide by a 100 nm $Al_{0.55}Ga_{0.45}As$ lift-off layer and 800 nm bottom contact layer. To reduce the waveguide losses from the double-metal cladding and contacts, the active region was increased 50% to 15 µm, 271 cascades, doping reduced to $1.25e^{16}$ cm^{-3}, and the bottom contact layer thickness was reduced to 100 nm. The GaAs-based QCL has a large advantage over other material systems when growing 10-15 µm active regions because lattice matching is not a critical factor.

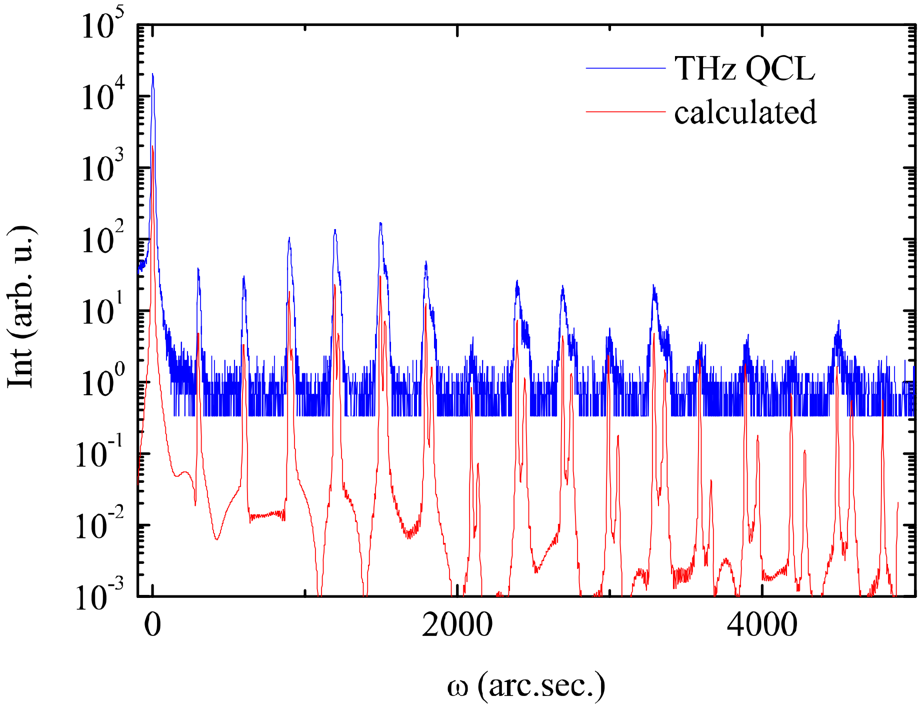

Fig. 2: X-ray diffraction (002) rocking curve of a 15 µm THz QCL active region with 271 cascade periods. The top (blue) curve is the measured scan and bottom (red) curve is the calculated diffraction pattern. What appear to be peak splitting are actually satellite peaks resulting from the designed structure.

Waveguide	**J_{th} (kA/cm^2)**	**T_{max} Pulsed**	**T_{max} CW**	**Active Region**	**Doping (cm^{-3})**
Surface Plasmon	1.88	88 K	-	10 µm	1.9e16
Double Metal	0.993	145 K	-	10 µm	1.9e16
Double Metal	0.506	145 K	25 K	15 µm	1.25e16
Double Metal	0.305	147 K	68 K	15 µm	8.0e15
Double Metal	0.205	133 K	72 K	15 µm	5.0e15

Table 1: Performance Characteristics of THz QCL with Decreasing Si Doping.

The double metal waveguide, due to strong mode confinement, resulted in a dramatic 50% reduction in J_{th} and pulsed operation T_{max}. The first three samples lased up to 145 K with a characteristic T_0 of 33 K. However, the continuous wave (CW) operation of the three samples differed greatly, with CW up to 25 K only in the initial low doped structures. A further reduction in doping resulted in a lower J_{th}, increased CW T_{max} of 72 K, at a cost of a reduction in the current operating range, output power, and pulsed T_{max}.

Conclusion

A 15-µm active region terahertz (2.86 THz) quantum cascade laser was optimized for maximum continuous wave temperature operation. Through the use of high-resolution x-ray diffraction, improved growth rate and doping calibrations, minimization of flux transients, a double-metal waveguide, and optimization of doping the threshold current was reduced from 1.88 to 0.205 kA/cm^2 and a maximum continuous wave operating temperature of 72K was achieved. The tolerable thickness variation in one cascade period was <1.1%.

References

[1] R. Köhler, A. Tredicucci, F. Beltram, H.E. Beere, E.H. Linfield, A.G. Davis, D.A. Ritchie, R.C. Jotti, and F. Rossi, Nature 417, 156 (2002)

[2] C. Pfluegl, M. Austerer, W. Schrenk, S. Golka, G. Strasser, R.P. Green, L.R. Wilson, J.W. Cockburn, A.B. Krysa, and J.S. Roberts, Appl. Phys. Lett. 86; 211102 (2005)

[3] S. Kumar, B.S. Williams, S. Kohen, Q. Hu, and J.L. Reno, Appl. Phys. Lett. 84, 2494 (2004)

[4] G. Fasching, A. Benz. K. Unterrainer, R. Zobel, A.M. Andrews, T. Roch, W. Schrenk, G. Strasser , Appl. Phys. Lett. 87, 211112 (2005).

[5] B.S. Williams, S. Kumar, H. Callebaut, Q. Hu, and J.L. Reno, Appl. Phys. Lett. 83, 2124 (2003).

Polarization Dependence of Photocurrent in Quantum-Dot Infrared Photodetectors

T. Gebhard[1], P.L. Souza[1,2], F.F. Schrey[1], G. Strasser[1], K. Unterrainer[1],
M.P. Pires[3], S.M. Landi[2], J.M. Villas-Boas[4], N. Studart[5]

[1]Photonics Institute and Center for Micro- and Nanostructures,
TU-Wien, A-1040 Vienna, Austria

[2]LabSem, CETUC, PUC-Rio,Rua Marquês de Sao Vicente 225,
Rio de Janeiro, 22451-900, Brazil

[3]Instituto de Física, Universidade Federal do Rio de Janeiro,
Rio de Janeiro, Brazil

[4]Ohio University, USA

[5]Instituto de Física, Universidade Federal de São Carlos,
São Carlos, Brazil

Through polarization dependence measurements of photocurrent together with theoretical calculations we were able to identify different intersubband transitions in InAs/InGaAs/InP quantum dot structures for infrared photodetectors and observe 2D/0D hybrid behavior of the dot structures.

Introduction

The technology to detect infrared photons is dominated by HgCdTe (MCT) photodetectors since about four decades. The major advantage of this material system is the tunability over a large detection range. Their high optical conversion efficiency and the wide-band response are hard to compete with. Despite that, there is still a need to improve handling, reliability, speed and reproducibility of state of the art infrared photodetectors. They are bulky due to cryogenic temperature operation, and the lack of uniformity of the grown material makes them only partially suitable for large focal plain arrays. The ripening process of the MCT technology was accompanied by intensive research efforts for alternative detector concepts for increased temperature operation, reliability and reproducibility. As a consequence of the highly advanced epitaxial growth techniques for III-V semiconductor materials, intersubband photo-detection via quantum wells (QW) showed great potential as a viable alternative. However, theoretical predictions show that quantum well infrared photo-detectors (QWIP) have problems as candidates to rival the MCT technology at higher temperatures, as the dark current in QWIP increases significantly due to inherent thermoionic emission. In addition, selection rules in QW prohibit light incoming parallel to the growth-direction to be absorbed in intersubband transitions. Gratings and random reflectors are needed to circumvent this physical limit. The evolution of quantum devices led to a further reduction of the confinement dimensionality and today self organized growth techniques made the growth of quantum dots (QD) possible for a variety of material systems. Quantum dot infrared photo-detectors (QDIP) are not only able to outperform QWIP [1], but they are also potential candidates to rival or outperform MCT photo-detectors [2]. The reduced phonon-electron interaction in QD results in a long lifetime of excited carriers. The photoconductive gain increases by magnitudes compared to QWIP and also the dark current is theoretically reduced significantly due to suppressed thermoionic emission. The absorption coefficient is also much higher than in QW. QD show the inherent feature to absorb normal incident light [3].

The features of QDIP are very sensitively connected to the degree of control during the growth process, where many different uncertainties lead to reduced reproducibility. The self-organized growth process spreads the dots size inhomogenously, and this decreases the detectivity of the devices. This effect cannot be eliminated, but only minimized technologically. QDIP without blocking layer have still a much higher dark current than QWIP caused by interlayer-dot-tunneling through defects and thermally excited carriers from upper excited states and are therefore far away from theoretically predicted limits.

Hence, real QDs are quite different from ideal. The intraband absorption and the consequently generated photocurrent (PC) in these devices should be fully understood. In particular, there has been some controversy in the literature on the polarization dependence of the PC for QDIP structures [4] – [7]. In this work we investigate the photocurrent (PC) as a function of temperature and polarization produced by QD structures where InAs dots are nucleated on top of an InGaAs QW. The dots are covered with an InP barrier. The observed PC peaks are attributed to different intraband transitions based on the PC data together with theoretical calculations.

Experimental

A doped sample with 20 and an undoped one with 10 dot layers were grown by metalorganic vapor phase epitaxy on semiinsulating (100) InP substrate. The InAs dots were grown on a 8.5 nm thick InGaAs layer lattice matched with InP and capped by 18 nm InP layer. The Si doping density of the 0.4 µm thick InP contact layers is $n = 4\times10^{18}$ cm^{-3} for both samples. The nominal doping level of the QD in the doped sample provides 2 electrons in the ground state per dot. The dot sheet density of about 9×10^{9} cm^{-2} and the median dot height of 9 nm were estimated by atomic force microscopy.

The PC polarization QD samples were investigated by a Fourier transform spectrometer for normal and 45° light incidence. Choosing the TE polarization implies that the electric field is totally in the plane of the layers. However, for the TM polarization, the electric field will have a component perpendicular to the layers.

The measured spectra were corrected by the system response and by the Fresnel refraction coefficients for both polarizations.

Results

A PC signal was detected up to 50 K and 90 K for the doped and undoped sample, respectively. Polarization dependent PC measurements of the undoped sample show a signal around 5.3 µm. Figure 1 shows the PC spectra at 6 K for the undoped sample for different experimental configurations: normal incidence, 45 degrees incidence with TE polarization, 45 degrees incidence with TM polarization, and unpolarized light. Choosing the TE polarization implies that the electric field is totally in the plane of the layers. On the other hand, for the TM polarization, the electric field will have a component perpendicular to them. The same peak is observed for all configurations. However, for the TE polarization the PC signal was expected to be of the same order of magnitude as for the TM polarization, indicating that the energy levels involved have a 0D character.

For the undoped sample the transition around 5.3 µm should depart from the ground state, because only this state is populated due to non-intentional doping. The simple 1D calculation estimate the transition energy from the ground state to the first excited state of about 184 meV; this is a underestimation of about 20% in comparison to the experimental results. Electrons in the first excited state can contribute to the photocurrent due to sequential tunneling, as it has been already observed for these samples [10]. This transition has the highest oscillator strength, so other transitions to the excited states can be excluded.

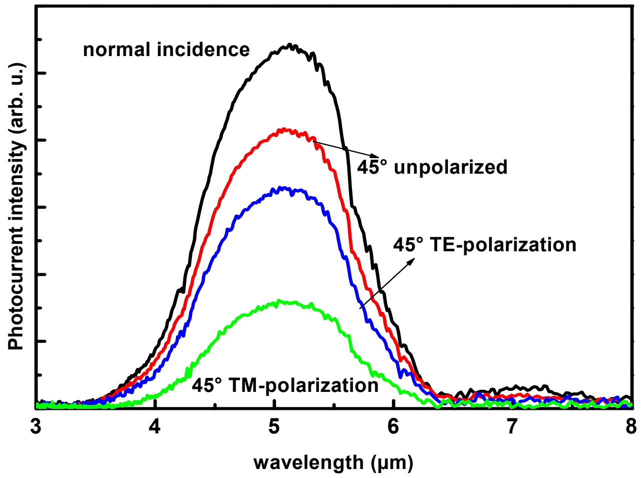

Fig. 1: Polarization dependence of the photocurrent at 6 K for the undoped sample.

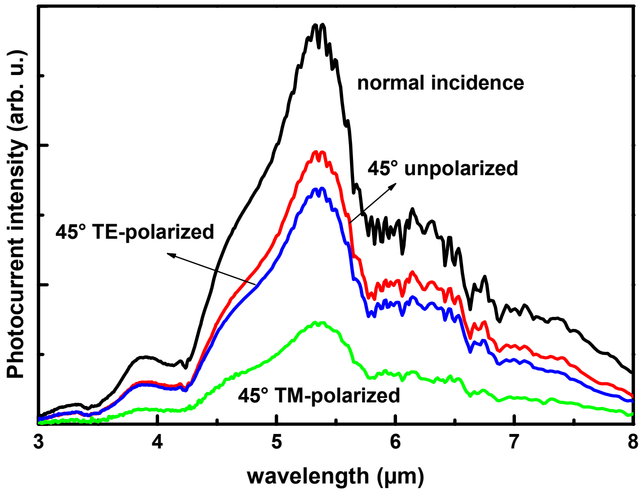

Fig. 2: Polarization dependence of the photocurrent at 6 K for the doped sample.

Equivalent polarization behavior, but noisier signal, is observed for the doped sample, as shown in Fig. 2. The doped sample contains twice as many layers as the undoped does. Even though one would expect a stronger signal, strain builds up more in such a thicker structure leading to more noise in the detected PC. Carefully looking in the spectra one observes that there are three peaks at 4 µm, 5.3 µm and 6.2 µm, corresponding to 310, 234 and 200 meV, in addition to a couple of shoulders. Using a simple 1D effective-mass model [8] for the InP/InGaAs/InAs/InP structure the band- configuration shown in Fig. 3 is obtained assuming a dot height of 9 nm and an InGaAs QW thickness of 10 nm.

For the doped sample additional transitions can also occur from the first and second excited states to the third excited state or to the continuum. The oscillator strength to the continuum is small compared to these to the third excited state. The transitions $E_1 - E_3$ and $E_2 - E_3$ correspond to 5.8 and 8.9 µm, respectively. The theoretical and experimental transition energies are in fairly good agreement, considering that such a simple 1D model was used; the theoretical values being overestimated by about 15%. Results of photoluminescence give further support to these peak assignments [10].

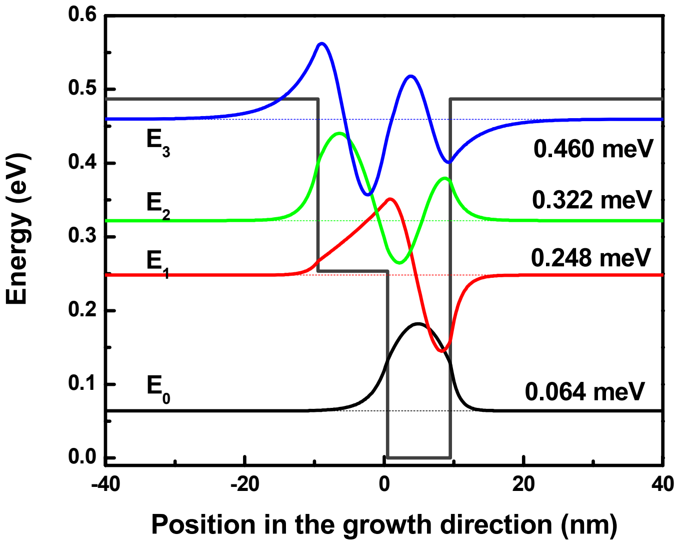

Fig. 3: Band configuration of the investigated samples.

Conclusion

We have performed polarization dependence measurements in InAs/InGaAs/InP quantum dot structures. Based on the difference between doped and undoped sample and the simple theoretical calculations, different transitions were identified. A strong PC-signal for s-polarization was observed as expected due to the 0D character of the QD. But surprisingly the PC for the p-polarization was rather weak showing little evidence 2D/0D hybrid behavior.

Acknowledgements

We acknowledge the financial support from CAPES, CNPq, FAPERJ, FINEP, Wolfgang Pauli Institute, FWF SFB IR-ON and ANSWER.

References

[1] E. T. Kim et al, 84, 3277 (2004)

[2] J. Phillips, J. Appl. Phys., 91, 4590 (2002)

[3] A. Rogalsky, Progress in Quantum Electronics, 27, 59-210 (2003)

[4] L. Chu et al, Appl. Phys. Lett., 75, 3599 (1999).

[5] L. Chu et al, Appl. Phys. Lett., 76, 1944 (2000).

[6] S. Sauvage et al, Appl. Phys. Lett., 78, 2327 (2001).

[7] B. Aslan et al, Appl. Phys. Lett., 82, 630 (2003).

[8] J. Mendoza-Alvarez et al, Physica E, 32, 85 (2006).

[9] A. G. Silva, et al, ICPS2006.

[10] T. Gebhard, et al, ICSNN2006.

Fabrication of Silicon Vertical Taper Structures for Fiber to Chip Coupler by KOH Anisotropic Etching

R. Holly, K. Hingerl

Christian Doppler Laboratory of Surface Optics, Institute of Semiconductor and Solid State Physics, Johannes Kepler University, Altenbergerstrasse 69, A-4040 Linz

R. Merz, P. Hudek, S. Neve, S. Partel, T. Auer

Forschungszentrum Mikrotechnik, FH Vorarlberg, Dornbirn, Austria

In order to exploit the full potential of silicon photonic devices we require an efficient way of coupling light from fibers to integrated photonic circuits. One of the most common solutions to this problem is the use of tapered silicon waveguides. We present a method of vertical silicon taper fabrication using KOH anisotropic etching. The main advantage of this method is the low roughness of the tilted surface, which should lead to a good optical transmission of the tapered waveguide. We successfully created vertical silicon tapers with heights more than sufficient for the use in fiber to chip light couplers.

Introduction

The use of high index contrast waveguides and devices is the key to successful development and fabrication of photonic integrated circuits. Considering the widespread use of silicon technologies and the suitable optical properties of silicon in the infrared range, this material is one of the best candidates for such devices [1]. In order to exploit the full potential of silicon photonic devices we require an efficient way of coupling light from fibers to integrated photonic circuits. One of the most common solutions to this problem is the use of tapered silicon waveguides [2]. However this approach is connected with the problem of creating a vertical taper. The efforts to fabricate such a taper are currently concentrated mainly on various lithography techniques used to create a taper shaped structure in photoresist. The pattern is then transferred to silicon by reactive ion etching. Although silicon taper structures have been already successfully fabricated using grayscale lithography methods [3], this approach introduces an additional non-standard lithography step and may also lead to the increase of the surface roughness, which is critical for the proper function of photonic devices [2].

One of the possibilities to fabricate a vertical taper structure is the use of a silicon substrate with a tilted <111> crystallographic orientation. Such wafers are produced by changing the cutting angle in the silicon wafer production process. In order to fabricate the desired vertical taper structure a very small angle (2 – 5 degrees) between the <111> orientation and the wafer surface is needed.

These substrates can then be used for the creation of a taper by means of anisotropic etching (i.e. etching along preferred crystallographic direction). One of the most suitable chemicals for anisotropic etching of silicon is potassium hydroxide (KOH) water solution. Under suitable process conditions (temperature, KOH concentration) we can achieve a big etching speed difference resulting in the uncovering of <111> planes.

Therefore using a substrate with tilted <111> plane should lead to the formation of vertically tilted surfaces which could be used for the fabrication of vertical taper structures.

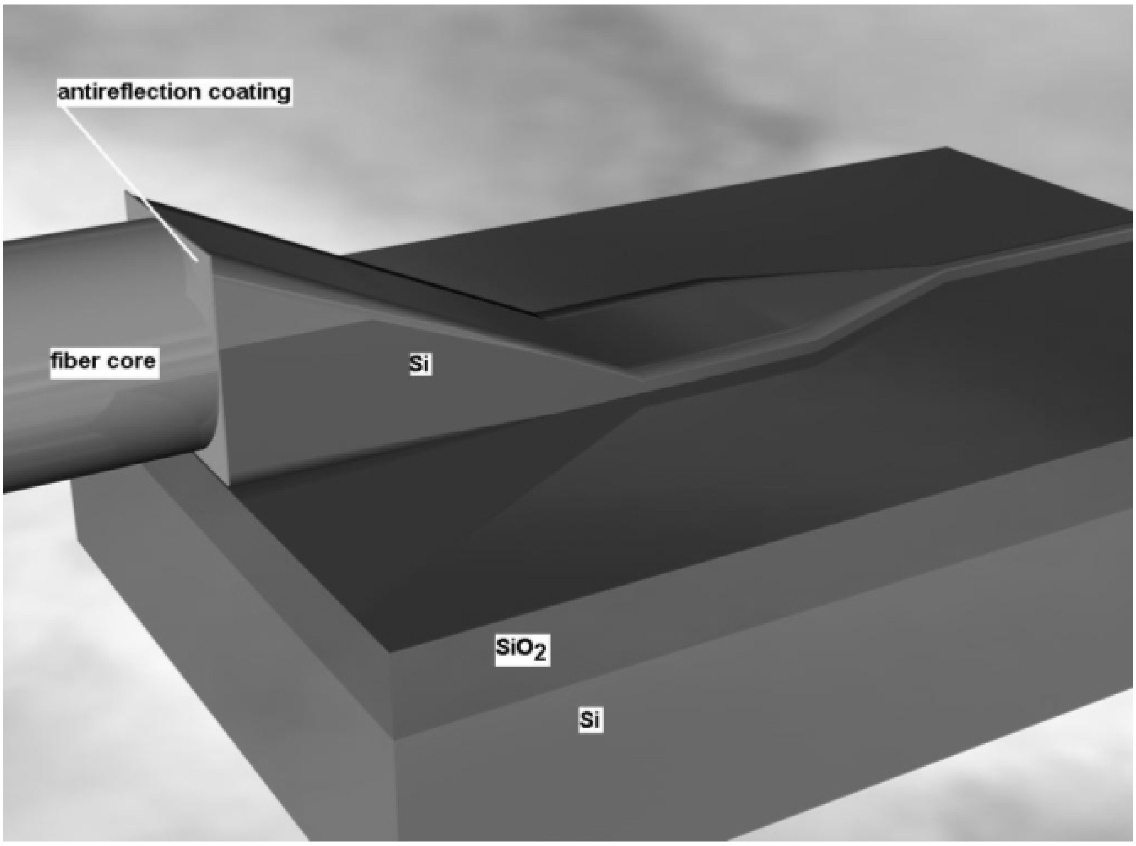

Fig. 1: Fiber to chip interface consisting of two silicon structures - one with vertical and one with horizontal tapering. The optical signal from a fiber core is led to the first taper via an antireflection coating to compensate the refractive index difference. The light propagates through both tapers and finally ends in a single mode silicon waveguide. Dimensions – Start: fiber core 6 µm in diameter; End: Si waveguide 300 x 300 nm; Length = 200 – 400 µm.

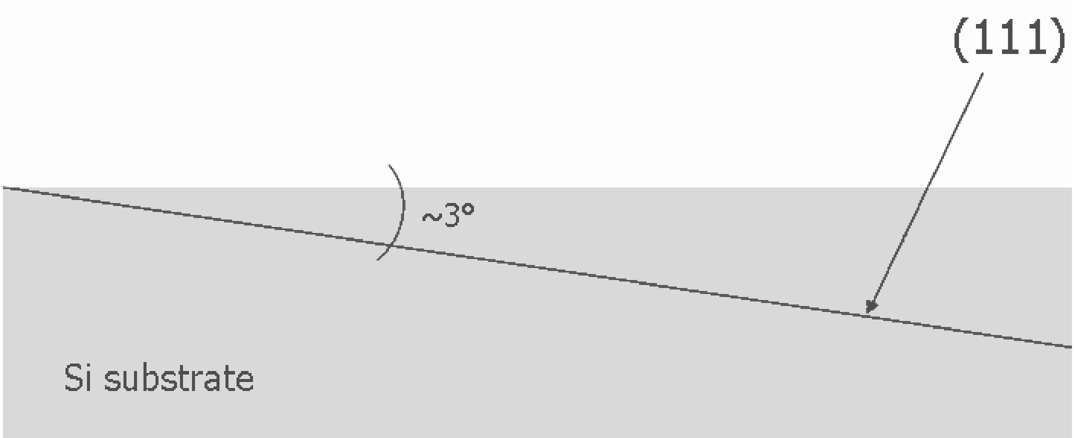

Fig. 2: Silicon substrate with tilted <111> plane.

The main advantages of this process are:

1. Simplicity (KOH wet chemical etching is well known and often used process)
2. Set tilt angle and shape (the angle only depends on the substrate and is not influenced by the process parameters and the shape is always linear)
3. Low roughness of the tilted surface

Experimental

The process of anisotropic silicon etching is influenced by several parameters. Besides etching solution parameters (KOH concentration, temperature), the etching process also depends on the roughness of the silicon substrate. This influence is becoming stronger with the decreasing angle between the <111> orientation and the wafer surface. The main reason for this behavior is the low etching speed of such substrate surfaces caused by the very small tilt angle – the surface plane orientation is very close to <111>. The presence of the surface roughness increases the etching speed, because it offers a possibility of directly etching the silicon in directions much different from the <111> plane. However this process continues only until the <111> planes are revealed and the surface consists of triangle shapes of random sizes. The average size of these triangles is determined by the initial surface roughness of the silicon substrate. Further etching results only in low etching speeds because the surface consists of <111> planes. Because of these obstacles, the fabrication of larger taper structures by simple etching of an unstructured silicon substrate is very difficult.

In order to obtain a larger structure, we can no longer depend on the surface roughness influence or the low etching speed in the vertical direction. Instead of this, we have to take advantage of much faster etching in the direction parallel to the substrate. This can be achieved by structuring the surface before the actual anisotropic etching takes place. One of the possibilities how to do this is to etch trenches or steps to the substrate and thus reveal planes perpendicular to the surface – Fig. 3.

With the structured substrate, we are able to achieve high etching speeds and reveal the <111> planes much faster than in the case of unstructured substrate. The size of the tilted surface obtained from the structured surface is dependent on the structuring depth – the depth of the etched steps / trenches.

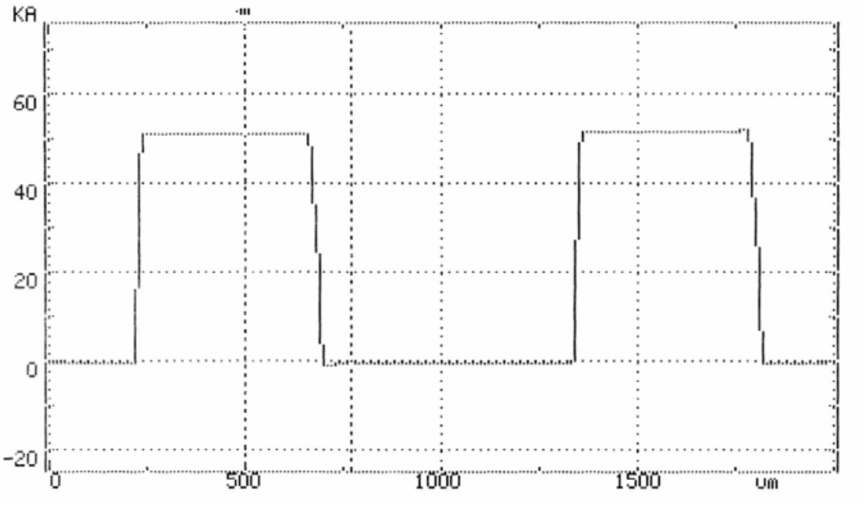

Fig. 3: Structured silicon profile – 5 µm deep trenches etched in silicon by reactive ion etching process.

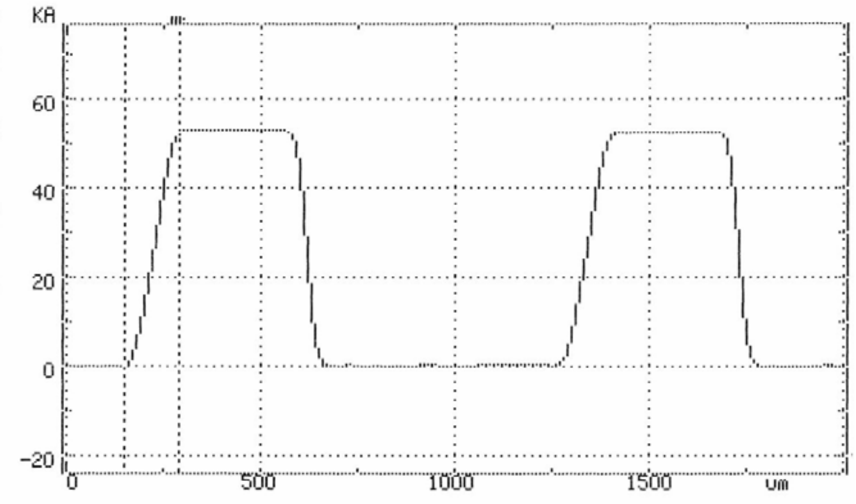

Fig. 4: The profile of the structured silicon after 30 min KOH etching, 47% KOH solution, 80ºC.

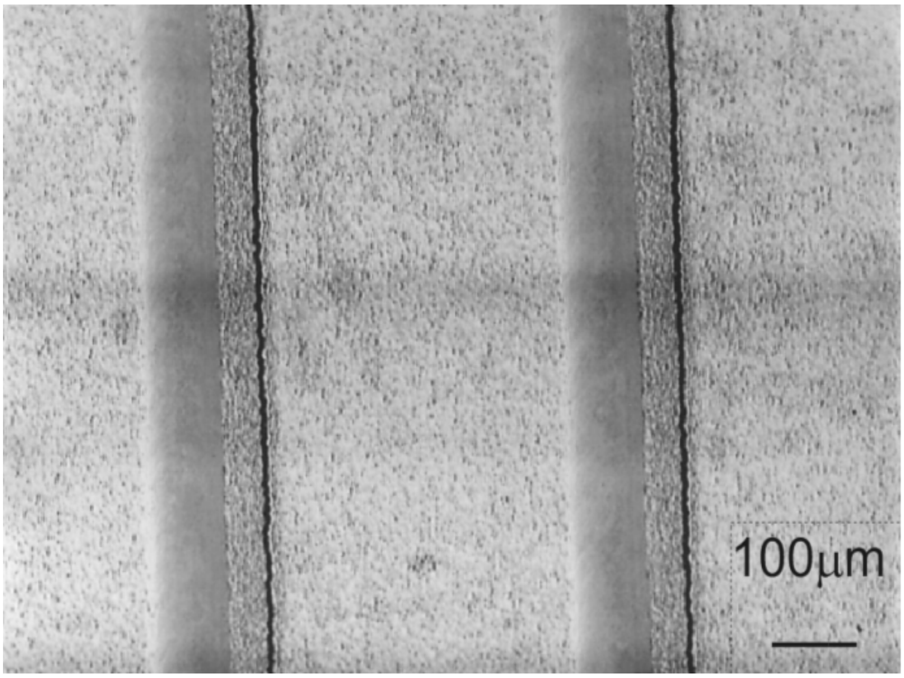

Fig. 5: Structured silicon surface after 30 min KOH etching, 47% KOH solution, 80ºC.

The KOH etching of the Si trenches can be described by two processes:

1. Etching in the direction parallel to the surface. Taper structures are formed mainly by fast etching parallel to the surface (~100 µm/hour). Taper height depends on the initial trench/edge depth or roughness – in the case of unstructured substrate. This process continues only until the <111> planes are revealed.
2. Etching in the direction perpendicular to the surface. This process is slow, results in further increase of the taper height but also increases the surface roughness.

In order to create a vertical taper structure with small surface roughness we need therefore to keep the KOH etching time as short as possible (the etching perpendicular to the surface will be in this case negligible).

Conclusions

Using the anisotropic etching of silicon with tilted <111> plane, we successfully created vertical silicon tapers with heights up to 35 µm and lengths up to 500 µm, which is more than sufficient for them to be used for fiber to chip light coupling.

We furthermore investigated the etching process of structured as well as unstructured silicon substrates and found out, that only the use of reactive ion etching prior to the KOH etching can ensure a well defined shape of the silicon vertical taper. Our experiments indicate a significant time dependence of the etched taper profile. In order to create a structure for the purpose of optical fiber to chip coupling, we need to keep the surface roughness minimal and therefore we have to reduce the time of the anisotropic etching to a minimum.

Basing on our experimental results, we are now able to design a fiber to chip optical interface with low scattering losses and high transmission.

References

[1] Mike Salib, Ling Liao, Richard Jones, Mike Morse, Ansheng Liu, Dean Samara-Rubio, Drew Alduino, Mario Paniccia, "*Silicon Photonics*", Intel Technology Journal Volume 08 Issue 02 (2004).

[2] Roel Baets, Wim Bogaerts, Dirk Taillaert, Pieter Dumon, Peter Bienstman, Dries Van Thourhout, Joris Van Campenhout, Vincent Wiaux, Johan Wouters, Stephan Beckx, "*Low Loss Nanophotonic Waveguides and Ring Resonators in Silicon-on-Insulator*" in *Proceedings of the International School of Quantum Electronics*, 39th course "*Microresonators as building blocks for VLSI photonics*", 709, Italy, p.308-327 (2003).

[3] Anita Sure, Thomas Dillon, Janusz Murakowski, Chunchen Lin, David Pustai and Dennis W. Prather, "*Fabrication and characterization of three-dimensional silicon tapers*", Optics Express Vol. 11, No. 26 (2003).

Two and One Dimensional Light Propagation in Layer-by-Layer Deposited Colloidal Nanocrystal Waveguides

S. Pichler, J. Roither, M. V. Kovalenko, W. Heiss

Institute of Semiconductor and Solid State Physics,
University Linz, A-4040 Linz

P. Feychuk, O. Panchuk

Institute of Organic Chemistry, University of Chernivtsi,
Chernivtsi 58012, Ukraine

Optical waveguides containing high concentrations of colloidal nanocrystals have been fabricated by layer-by-layer deposition on planar and patterned glass substrates. The two- and one dimensional waveguiding in these structures is demonstrated by propagation loss experiments. The experimental results obtained for various film thicknesses and widths of the waveguide stripes indicate that the losses are dominated by surface roughness. The deposition on the structured samples does not lead to any additional losses. This fact and the exceptionally high content of nanocrystals make these structures highly suitable for photonic applications like laser or optical amplifiers.

Introduction

Colloidal semiconductor nanocrystals (NCs) [1] – [3] give a widely size tunable room temperature luminescence [4], [5] with quantum efficiencies close to unity [6], and they are soluble in various organic and inorganic solvents [7]. All these characteristics provide a flexible platform for the development of integrated photonic devices like optical amplifiers and lasers operating at room temperature and over a broad spectral range. The main difficulty in achieving NC-based lasing is the very efficient nonradiative Auger recombination [8], so that laser operation is achieved so far only with pulsed excitation [9] – [11]. Strategies to improve the laser performance are (a), to increase the NC concentration in the active layer in order to increase the gain [12], (b), the use of high-finesse optical feedback structures [9] – [11], and (c), the optimization of the quality of the optical waveguides. Therefore, here we present a systematic investigation of the optical properties of two (2D) and one dimensional (1D) waveguides (WGs) optically activated by strongly luminescent colloidal CdTe NCs. To obtain structures with smooth surfaces and high NC volume fractions the layer-by-layer deposition technique [13] is applied. The waveguiding properties are investigated by propagation loss measurements. These measurements are done for waveguides with different parameters (width, thickness).

Sample Preparation

The NC WGs are fabricated by controlled deposition of CdTe NC/polymer films onto glass substrates by the layer-by-layer assembly method. This makes use of the alternating adsorption of (sub)monolayers of positively charged poly(diallyldimethylammonium chloride) (PDDA) molecules and negatively surface-charged CdTe NCs, each provided in aqueous solutions. The total film thickness is controlled by the number of PDDA/CdTe NC bilayers and by the deposition time for each monolayer. For a film with 40 bilayers we obtain a typical thickness of 120 nm. Since the effective thickness of a PDDA molecule (approx. 1 nm) is several times smaller than that of the used CdTe NCs with a diameter of approximately 3.2 nm [14], the layer-by-layer technique allows to obtain exceptionally high NC concentrations (close to 60% in volume as determined from the optical film density).

For the fabrication of 1D WGs, the NC/polymer bilayer films were deposited on substrates which were patterned with grooves, with a width of 5, 10, 20 and 40 µm and a length of 2 cm. The grooves with a depth of 450 nm were wet chemically etched by a buffered HF solution whereby a 30 nm thick Cr layer was used as etch mask (see inset of Fig 1(g)).

Results and Discussion

The waveguiding properties of the NC/polymer films are studied by propagation loss measurements, making use of the NC luminescence. In particular, an Ar-ion laser was used to excite the NCs from a direction perpendicular to the sample surface while the photoluminescence (PL) emitted in lateral direction is collected from the sample edge by a microscope objective. The PL spectra are recorded as a function of the distance z, measured between the excitation spot, which is moved by a mirror, and the edge of the sample (see inset in Fig 1(c))

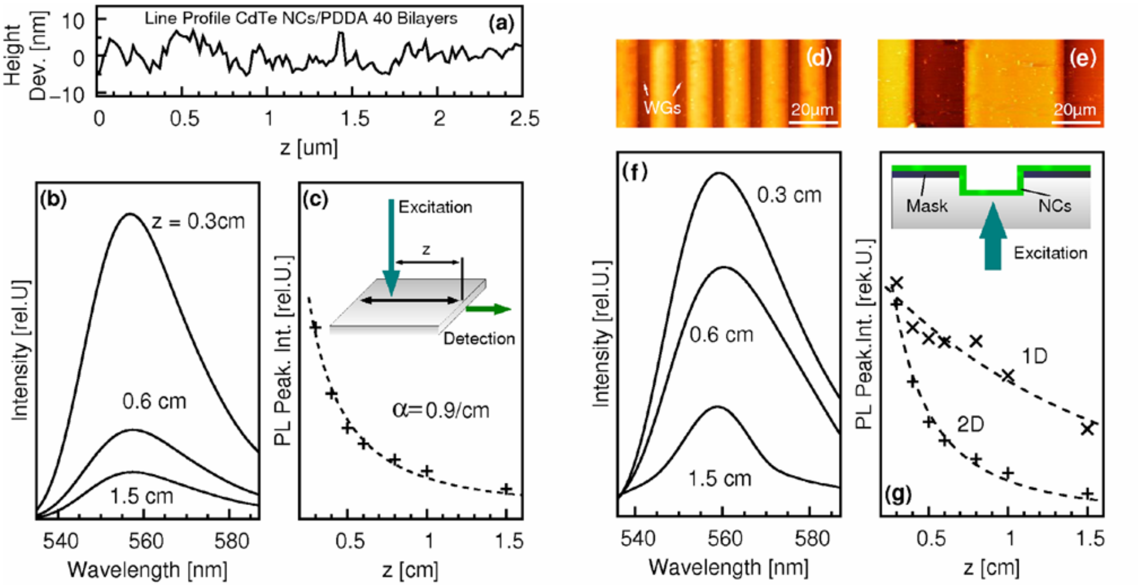

Fig. 1: (a) Surface scan of 2D 40 BL sample, (b) spectra recorded at different excitation distances (2D), (c) PL Intensity over several distances (2D), (d) and (e) AFM micrographs of 1d samples, (f) spectra recorded at different excitation distances (1D), (g) PL Intensity over several distances (1D)

Figure 1(b) shows the PL spectra for various distances z between excitation point and sample edge, revealing that increasing z results in a decrease of the PL intensity, regardless of the emission wavelength. Therefore, it is sufficient to examine the dependence of the peak intensity, as is given in Fig. 1(c). There, the experimental data are fitted by a function which is proportional to $(1/z)e^{-\alpha z}$ (solid line). Here the factor 1/z accounts for the intensity drop of a radial wave, originating from a point source, within a

2D slab. The exponentially decaying part is ascribed to the intensity drop caused by losses in the WG.

The luminescence spectra observed for the NCs in the grooves (Fig. 1(f)) exhibit a very similar shape than those for the planar films. The decay of the PL intensity with increasing propagation distance z, however, is by far smaller as in the 2D case. This is shown in detail in Fig 1(g), where the dependence of the peak PL intensities on z for the 1D and the 2D case are compared. For the 1D in particular, the decay can be fitted by a single exponential one, without the 1/z prefactor, which we quote as an indication for the truly 1D waveguiding of the light in the NC/PMMA film deposited on the patterned substrates. The resulting loss coefficients are the same for 1D and 2D samples, evidencing that purely 1D waveguiding occurs in the patterned samples.

To show that the WG losses are dominated by the surface roughness, we investigated 1D WGs with various layer thicknesses and widths. Reducing the thickness from 40 to 10 NC/PDDA bilayers results in an increase of the loss coefficient by a factor of 2. This is almost independent on the width of the substrate grooves, varied between 5 and 40 µm.

Conclusion

In summary the high potential of layer-by-layer deposited NC/PDDA films for applications in optical devices is demonstrated. In these films, deposited on planar as well as on patterned glass substrates two and one dimensional waveguiding is observed with penetration length of several centimeters.

Acknowledgements

Financial support from the Austrian Science Foundation FWF (Project START Y179 and SFB 25-IRON) is gratefully acknowledged.

References

[1] C. B. Murray, D. J. Norris, and M. G. Bawendi: “*Synthesis and characterization of nearly monodisperse CdE (E=S, Se, Te) semiconductor nanocrystallites*”, J. Am. Chem. Soc. 115, 1993, p. 8706

[2] M. A. Hines and P. Guyot-Sionnest: “*Synthesis and characterization of strongly luminescing ZnS-capped CdSe nanocrystals*”, J. Phys. Chem. 100, 1996, p. 468

[3] A. P. Alivisatos, “*Semiconductor clusters nanocrystals, and quantum dots*”, Science 271, 1996, p. 933

[4] J. M. Pietryga, R. D. Schaller, D. Werder, M. H. Stewart, V. I. Klimov, and J. A. Hollingsworth: “*Pushing the Band Gap Envelope: Mid-Infrared Emitting Colloidal PbSe Quantum Dots*” J. Am. Chem. Soc. 126, 2004, p. 11752

[5] L. Qu and X. Peng: “*Control of photoluminescence properties of CdSe nanocrystals in growth*” J. Am. Chem. Soc. 124, 2002, p. 2049

[6] I. Mekis, D. V. Talapin, A. Kornowski, M. Haase, and H. Weller: “*One-pot synthesis of highly luminescent CdSe/CdS core-shell nanocrystals via organometallic and “greener” chemical approaches*” J. Phys. Chem. B 107, 2003, p. 7454.

[7] M. A. Petruska, A. V. Malko, P. M. Voyles, and V. I. Klimov: *“High-Performance, Quantum Dot Nanocomposites for Nonlinear Optical and Optical Gain Applications*”, Adv. Mater. 15, 2003, p. 610 and Refs. therein.

[8] V. I. Klimov, A. A. Mikhailovsky, D. W. McBranch, C. A. Leatherdale, and M. G. Bawendi: “*Quantization of multiparticle auger rates in semiconductor quantum dots*”, Science 287, 2000, p. 1011,

[9] H.-J. Eisler, V. C. Sundar, M. G. Bawendi, M. Walsh, H. I. Smith, and V. I. Klimov: “*Color-selective semiconductor nanocrystal laser*” Appl. Phys. Lett. 80, 2002, p. 4614,

[10] A. V. Malko, A. A. Mikhailovsky, M. A. Petruska, J. A. Hollingsworth, H. Htoon, M. G. Bawendi, and V. I. Klimov: “*From amplified spontaneous emission to microring lasing using nanocrystal quantum dot solids*”, Appl. Phys. Lett. 81, 2002, p. 1303,

[11] P. T. Snee, Y. Chan, D. G. Nocera, and M. G. Bawendi: “*Whispering-Gallery-Mode Lasing from a Semiconductor Nanocrystal/Microsphere Resonator Composite*”, Adv. Mater. 17, 2005, p. 1131,

[12] V. I. Klimov, A. A. Mikhailovsky, S. Xu, A. Malko, J. A. Hollingsworth, C. A. Leatherdale, H.-J. Eisler, and M. G. Bawendi: “*Optical gain and stimulated emission in nanocrystal quantum dots*” Science 290, 2000, p. 314

[13] G. Decher: “*Fuzzy Nanoassemblies: Towards Layered Polymeric Multicomposites*”, Science 277, 1997, p. 1232 (1997)

[14] W. W. Yu, L. Qu, W. Guo, and X. Peng: “*Experimental Determination of the Extinction Coefficient of CdTe, CdSe, and CdS Nanocrystals*”, Chem. Mater. 15, 2003, p. 2854

Strain Induced Modifications of Optoelectronic Properties of PbSe Nanostructures

M. Simma, D. Lugovyy, T. Fromherz, G. Springholz, G. Bauer

Institut für Halbleiter- und Festkörperphysik,
Universität Linz, A-4040 Linz, Austria

Deformation potentials D_u and D_d for PbSe were analyzed using transmission data of PbSe/PbEuSeTe multi-quantum wells. We use calculations based on a *kp* model to obtain the strain induced intervalley splitting in the quantum wells. For the reduction of the Fabri-Pérot interference fringes of the multilayer structures 480 Å NiCr anti-reflex coating is deposited on top of the multi-quantum wells. At low temperature we found PbSe deformation potentials D_u = -1.97 and D_u = 5.88. The results of the transmission measurements are compared with photo-current spectra measured with self-assembled PbSe/PbEuTe quantum dot superlattices.

Introduction

For the design of heterostructure optoelectronic devices the accurate knowledge of deformation potentials is of crucial importance. In the narrow gap IV-VI semiconductors due to large deformation potentials, even moderate strain values result in significant shift of the band edges. Theoretically [3], [2] and experimentally [8], [5] determined deformation potentials are spread over a wide range, especially the biaxial deformation potentials components. For example, according to Zasavitskii et al. [8] the uniaxial deformation potential component for PbSe D_u varies from -0.2 to -3.7 eV. In addition, most values do not agree with the isotropic deformation potentials, which can be measured with high accuracy from hydrostatic pressure experiments.

Experimental

IV-VI semiconductors are soft materials and therefore, it is rather difficult to produce uniaxial strains by applied external forces. In this work, the strain in PbSe layers result from the lattice mismatch between the constituting materials of epitaxial PbSe/PbEuSeTe multi-quantum well structures (MQW). The heterostructures are grown on (111) oriented BaF_2 substrates in a molecular-beam epitaxy (MBE) system. The 80 periods MQWs were grown on 1.5 µm fully relaxed buffer layers consisting of PbEuSeTe with the same composition as the barrier layers. The strain in the PbSe QWs is caused by the lattice mismatch to the PbEuSeTe buffer and barrier layers. The latter is determined mainly by the Te content in the quaternary layers, for which the lattice constant follows the same Vegards law as for PbSeTe. Thus, for the used quaternary composition of y_{Te} = 6 – 14% the strain in the PbSe QWs varies between $\varepsilon_{||}$ = 0.48 – 1.1%. The barrier height, on the other hand, is mainly determined by the Eu concentration due to the very large bandgap increase with increasing Eu content. For $x_{Eu} \approx 8\%$ used in this work, the energy band gap of the PbEuSeTe barrier layer is about 290 meV larger then that of PbSe. The thin PbSe 40 Å quantum wells (QW) are grown below the critical layer thickness and are pseudomorphically strained. Using this material system we have the possibility to tune the energy gap in the barriers and the strain in the QWs virtually independently by the Eu and Te content of the PbEuSeTe alloy.

Samples with different strain values and similar Eu content were investigated using Fourier transform infrared spectroscopy (FTIR). Transmission spectra of the PbSe/ PbEuSeTe MQWs were measured at temperatures between 6 K and 300 K in the spectral range of 500 cm^{-1} to 6000 cm^{-1} with a resolution of 8 cm^{-1} using a Bruker IFS-113v Fourier transform spectrometer.

Using two spectra measured at slightly different temperatures, we obtain the differential transmission as the logarithm of the ratio between the spectra measured at higher temperature and lower temperature. This approach takes advantage of the very strong temperature dependence of the PbSe and PbEuSeTe bandgaps and consequently, of the energy levels in the QWs, which results in pronounced peaks in the differential transmission spectra at the transition energies. Additionally, the differential spectra show much less pronounced Fabri-Pérot interference fringes caused by the layer refractive index contrast between the transparent BaF_2 substrate ($n \approx 1.5$) and the IV-VI epilayers ($n \approx 4.5$). This is due to the fact that the dielectric constants of the materials in the multilayer structure vary only weakly with temperature. For further reduction of the Fabri-Pérot interference fringes 480 Å NiCr [11] anti-reflection coating was deposited on the multilayer stack of the samples.

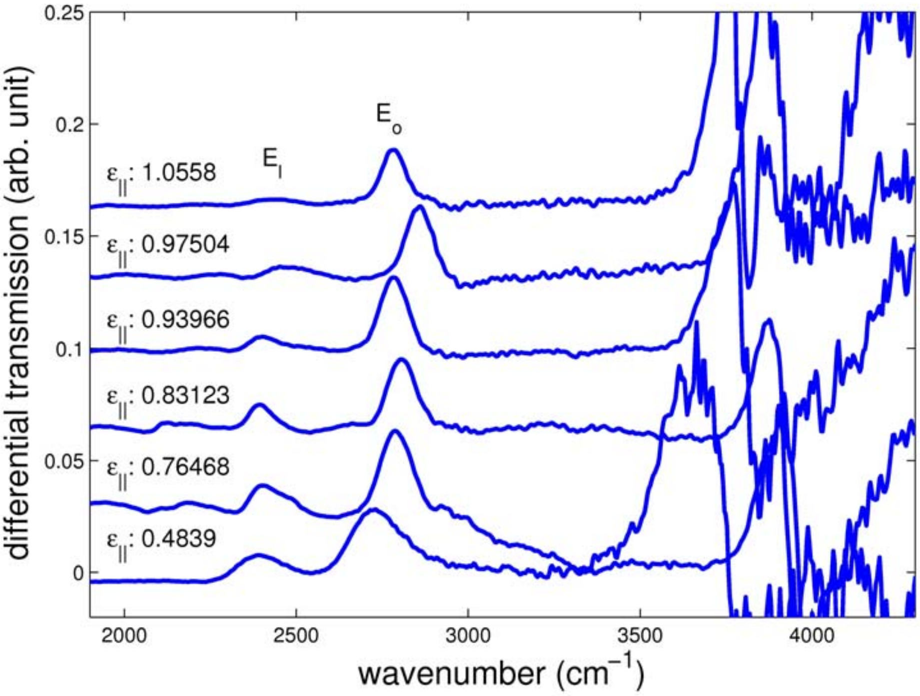

Fig 1: Differential transmission spectra of PbSe/PbEuSeTe MQWs for different strain values. As the strain increases, the L-valley splitting between the longitudinal (E_l) and the oblique valley (E_o) increases.

For each sample, the differential transmission shown in Fig. 1 exhibits three peaks caused by the optical transitions related to the longitudinal (E_l) and oblique L-valleys (E_o) in the PbSe QWs and the PbEuSeTe fundamental absorption in the barrier layers. Because of the narrow 40 Å PbSe well width no transitions to higher energy levels can be observed, indicating that higher energy levels are not confined in the QWs. The peaks related to the longitudinal valley transition show a weaker intensity compared to the peaks of the oblique valleys. This is due to the threefold degeneracy of the oblique valleys. The clearly resolvable L-valley splitting Δ (see Fig. 1) increases with increasing strain. This intervalley splitting is caused on the one hand by the different effective electron and hole masses along the confinement direction of the oblique and longitudinal valleys, on the other hand by the different band gap shifts due to the biaxial strain in the layers. In thick epitaxial layers were the confinement shift of the optical transitions is zero the intervalley splitting is equal [8]

$$\Delta=\delta E_g^N-\delta E_g^O=\frac{8}{9}D_u(\varepsilon_{\perp}-\varepsilon_{\parallel}) \qquad (1),$$

where D_u denotes the uniaxial component of the deformation potentials and $\varepsilon_{\parallel}$ and $\varepsilon_{\perp}$ are the in-plane and perpendicular strains, respectively. In smaller QWs the optical transition energies as well as the intervalley splitting is increased by the quantum confinement effect. Therefore, in order to be able to apply Eq. 1 the confinement energies have to be subtracted from the measured transition energies.

The energy levels in the PbSe quantum wells can be calculated numerically with high accuracy using the envelope function method based on a *kp* model if the confinement energies in valence and conduction band are known. We estimated these confinement energies assuming that the unstrained PbSe/PbEuSeTe band-offsets in valence and conduction bands are equal ($\Delta E_c = \Delta E_v$), due to the mirror like bandstructure [7] of these materials. For the calculation of ΔE_v we used temperature dependent energy gaps of PbEuSe and PbEuTe given in [9] and [10], where the energy gap of PbEuSeTe is linearly interpolated.

The influence of the strain on the band-edge energies is given by the expression

$$\delta E=\sum D_{ij}^{c,v}\varepsilon_{ij}(2) \qquad (2),$$

where $D_{ij}^{c,v}$ is the deformation potential tensor in the conduction and valence band and ε_{ij} denotes the strain tensor. In cubic systems this expression is simplified to two components $D_u^{c,v}$ and $D_d^{c,v}$ i.e., the uniaxial and dilatation deformation potentials and the $\varepsilon_{\perp}$ and $\varepsilon_{\parallel}$ strain components.

The change in the bandgap is then characterized by the deformation potentials Du and Dd which are equal to the difference of the $D_u^{c,v}$, $D_d^{c,v}$ values of the conduction and valence bands. Using deformation potentials given in literature [3] we calculated from the optically measured transition energies the strain induced intervalley splitting. To derive the uniaxial deformation potential constant D_u with the help of Eq. (1) the calculated energy levels are subtracted from the measured transition data. For the 6 K measurement we get for D_u a value of -1.97 eV and at 77 K a value of D_u = -2.39 eV. Using the relation $D_{iso} = 3D_d + D_u$ and D_{iso} = 15.7 eV for the isotropic deformation potential constants [5] we calculated the dilatation deformation potential as D_d = 5.88 eV and D_d = 6.03 eV at 6 K and 77 K, respectively. The measured values for D_u agrees well with the theoretically determined values given in [3], [2].

Assuming a symmetric band offset in the unstrained case and the theoretical deformation potentials values given in Ref. [3], one obtains a rapidly increasing band offset asymmetry with increasing strain in the PbSe layers. In particular a type I - type II band alignment discontinuity transition is expected at strain values larger than about 80% for the given Eu concentration of 8%. Thus, at high strain values the PbSe valence band edge lies energetically below the barrier valence band edge. In this case, the PbSe valence band acts as barrier for the holes. For such a type II band alignment, the spatially indirect optical transitions are much weaker due to the reduced wavefunction overlap. The upper spectra in Fig. 1 resulting from the highly strained MQW structures exhibits a significantly weaker longitudinal valley peak than the spectra of the other samples.

Indications for such a type II band alignment are also obtained from photo-current (PC) measurements on highly strained PbSe/PbEuTe self-assembled quantum dot superlattices. These superlattices were grown by MBE onto (111) BaF_2 substrates [4] on 1.5 µm PbEuTe buffer layers at 340 – 420 °C. On these buffer 5 – 8 monolayers of PbSe were grown followed by a PbEuTe spacer layer with 6% Eu content and a thickness varying between 250 and 650 Å. The strain in the thin epitaxial PbSe layer resulting from the lattice misfit between PbSe and PbEuTe relaxes via island formation. This island formation starts after deposition of 3 ML PbSe [4] which compose a 2D wetting layer. By deposition of many PbSe/PbEuTe bilayers, a highly efficient 3D dot ordering takes place [4]. Using FTIR spectroscopy, we performed spectral resolved lateral photo-current measurements on these self-assembled QD structures.

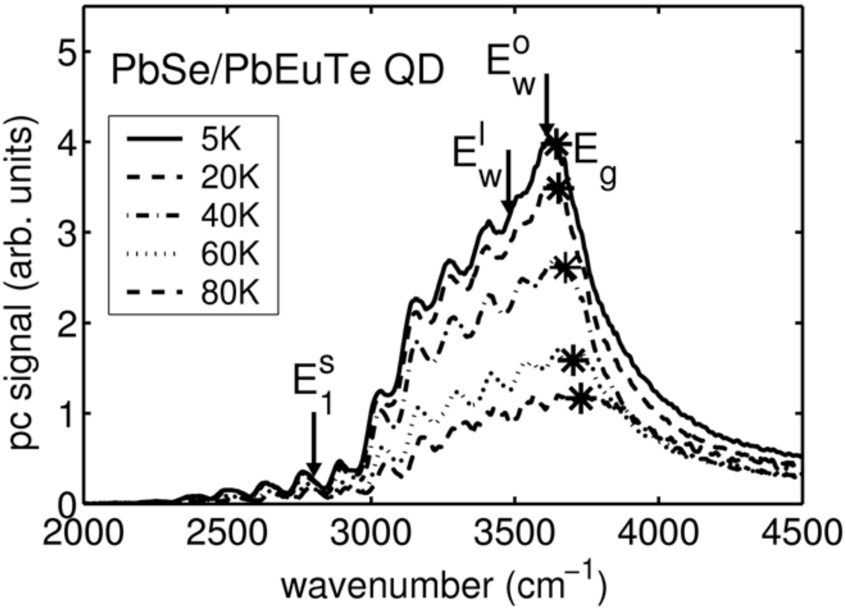

Fig 2: Photo-response of a PbSe/PbEuSeTe QD superlattice for different temperatures. Arrows indicates the optical transitions to different structures in the superlattice: E_1^s PbSe QD, E_w^l and E_w^o longitudinal and oblique wetting layer valley. The barrier bandgap E_g is marked with (*).

For a type I band alignment one would expect a freeze out of the carriers in the QD at low temperature resulting in vanishing lateral pc-signal. Figure 2 shows the photo-response measured at different temperatures performed with 50 Å high QD. The transition energies caused by various structures in the QD structures are marked by arrows. The arrow labeled as E_1^s is related to the QD ground s-state transition. The arrows labeled by E_w^l and E_w^o are the ground state transitions of the longitudinal and oblique valleys in the wetting layer. The quantum size energies in the dots and the wetting layer were calculated with the envelope function method using a *kp* model. For the QDs a simplified spherical shape [1] was assumed. The absorption edge at 3800 cm^{-1} marked by * is caused by the buffer and barrier layer fundamental transition. Clearly the pc-signal is well resolved for all temperatures, in particular, no freeze out of the carriers is observed. This indicates a type II band alignment of the PbSe QD. Assuming a band discontinuity of 120 meV between the PbSe/PbTe valence band edges [6] leads to a type I band alignment in the unstrained case. Using deformation potentials given in [3] shifts the valence band edge of PbSe below the PbEuTe valence band edge. This assumptions result in a type II band alignment which explains the observed pc-signal at low temperatures.

Conclusion

In summary, strained PbSe multi-quantum wells and quantum dot superlattices structures were investigated by FTIR spectroscopy. We deposit a NiCr anti-reflection coating on the MQW samples in order to reduce the Fabri-Pérot interference fringes. Longitudinal and oblique valley subband transitions were observed and from the intervalley splitting the PbSe deformation potentials were determined. For increasing strain in the samples we observe a transition from type I to type II band alignment. Temperature dependent spectrally resolved photo-response of PbSe QD superlattices does not show any freeze out of the carriers. This indicates a type II band alignment of the PbSe dots.

Acknowledgments

Work supported by Öster. FWF Forschung, SFB IRON, Projekt Nr. F2504-N08.

References

[1] M. Califano and P. Harrison: J. Appl. Phys., 86, 5054, (1999).

[2] P. Enders: Phys. Status Solidi B, 129, 89, (1982); 132, 165, (1985).

[3] L. G. Ferreira: Phys. Rev., 137, 1601, (1965).

[4] G. Springholz, V. Holy, M. Pinczolits, and G. Bauer: Science, 282, 734, (1998).

[5] M. V. Valeiko, I. I. Zasavitzkii, A. V. Marveenko, B. N. Matsonashvili, and Z. A. Rukhadze: Superlattices. Microstruct, 9, 195, (1991).

[6] S. H. Wei and A. Zunger: Phys. Rev B, 55, 13605, (1997).

[7] G. Bauer: Narrow Gap Semiconductors: Physics and Applications, Vol. 133, Springer Lecture Notes in Phys., edited by W. Zawadski (Springer, Berlin, 1980), p. 427.

[8] I. I. Zasavitskii, E. A. de Andrada e Silva, E. Abramof, and P. J. McCann: Phys. Rev. B, 70, 115302–1, (2004).

[9] T. Maurice, F. Mahoukou, G. Breton, S. Charat, P. Masri, M. Averous, and R. Bisaro: Phys. Stat. Sol., (b) 209, 523, (1998).

[10] S. Yuan, H. Krenn, G. Springholz, and G. Bauer: Phys. Rev. B, 47, 7213, (1993).

[11] S. W. McKnight, K. P. Stewart. H. D. Drew, and K. Moorjani: Infrared Phys. 27, 327 (1987)

Analytic Methods (Posters)

Ballistic Electron Emission Microscopy/Spectroscopy on Au/Titanylphthalocyanine/GaAs Heterostructures

S. Özcan[1], T. Roch[1], G. Strasser[1], J. Smoliner[1], R. Franke[2] ,T. Fritz[2]

[1] Institut für Festkörperelektronik, TU Wien, A-1040 Vienna

[2] Institut für Festkörperphysik, TU Wien, A-1040 Vienna

In this article Au/titanylphthalocyanine/GaAs diodes incorporating ultra smooth thin films of the archetypal organic semiconductor titanylphthalocyanine (TiOPc) were investigated by Ballistic Electron Emission Microscopy/Spectroscopy (BEEM/S). Analyzing the BEEM spectra, we find that the TiOPc increases the BEEM threshold voltage compared to reference Au/GaAs diodes. From BEEM images taken we conclude that our molecular beam epitaxial (MBE) grown samples show very homogeneous transmission, compared to wet chemically manufactured organic films. The barrier height measured on the Au- TiOPc-GaAs is Vb ~ 1.2eV, which is in good agreement with the data found in reference [1]. The results indicate that TiOPc functions as a p-type semiconductor, which is plausible since the measurements were carried out in air [2].

Introduction

In recent years, organic semiconductors have attracted much interest due to their variety of interesting optical, electrical and photoelectric properties. Photo- and electroactive organic materials have been the subject of recent attention including organic semiconductors, organic light emitting diodes [3], [4], organic field effect transistors [5], [6], or photovoltaic devices [7], [8]. In addition, organic semiconductors are already widely used in xerography, plate making printings and laser printers. Physicists and chemists have focused on the charge transfer phenomena of organic molecules and polymer organic semiconductors in the field of organic solar cells during the past decade. Besides these applied aspects there are important features motivating basic research, namely the interface properties between semiconductors and organic films, e.g. the deformation of the bandstructure at the interface.

Experimental

Ballistic-electron-emission microscopy (BEEM) [9], [10] is a three terminal extension of scanning tunneling microscopy (STM) [11], [12], where electrons tunnel between the STM tip and a thin Au film evaporated on a semiconductor surface such as Si or GaAs. If the electron energy is high enough to overcome the Schottky barrier height at the metal-semiconductor interface the electrons can penetrate ballistically into the semiconductor. This causes a current, which is measured with the third electrode on the backside of the sample. By sweeping the applied tip voltage BEEM current spectra can be obtained. By mapping the BEEM current for a constant tip bias while scanning the sample surface, images can be taken with a spatial resolution of about 1 nm. Over the last two decades BEEM became a well-established technique to determine Schottky barrier heights (SBH) and subsurface band offsets. An overview of this technique can be found in detail [13] – [15]. To guarantee good internal sample resistance and optimized BEEM signals, molecular beam epitaxial (MBE) grown GaAs samples were used as substrates. In detail, low doped (*N*D ~ 1 x 10^{16} cm^{-3}) GaAs layers (*d* ~ 1µm) were grown on an *n*+-wafer. On these substrates, TiOPc-films (*d* ~ 6 monolayers) were grown with organic MBE. Finally, a 7 nm Au layer was evaporated on top of it.

Results and Discussion

Figure 1(a) shows the topographic STM image and Fig. 1(b) the corresponding BEEM image of our Au/TiOPc/GaAs sample. The BEEM image was obtained simultaneously at a tip bias (V_t) of 1.4 V and a tip current (I_t) of 5 nA, with a scan area of 500 nm x 500 nm. The STM constant current image shows the typical or characteristic granular structure of Au. In the corresponding BEEM image, brighter areas indicate an enhanced electron transmission. Features visible in the BEEM image correlate exclusively with the granular structure and the topographic features of the Au-film and can not be correlated to the organic film underneath.

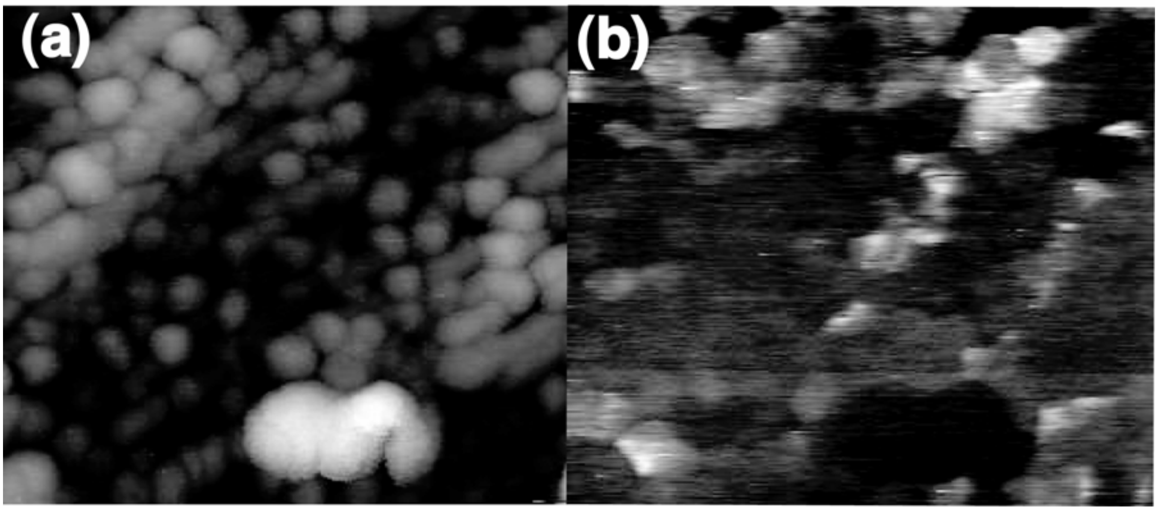

Fig. 1: (a) STM topographic image of Au/TiOPc/GaAs heterostructure, recorded at T = 300 K, I_t = 5 nA, V_t = 1.4 V. (b) Corresponding BEEM image (recorded simultaneously with the STM image, color scale corresponds to 0 . . . 1 pA .

To investigate the transmission behavior of TiOPc, we systematically measured ballistic electron spectra on various positions of our sample.

To extract the barrier height, i.e. the onset voltage, from the measured data, we use a quadratic power law fit (see, e.g. [13]). The Bell-Kaiser model was not used because already the straightforward power law, despite of its simplicity, fits our data very well and is completely sufficient for our purposes. The barrier height values gained from the power fit are 1.24 eV and 1.18 eV for sample A and B. The histograms of the two samples are in Fig. 2 and 3. We measured an effective barrier height of Au/TiOPc/GaAs. It must be pointed out that at present, we can not decide if the measured barrier height is the barrier of the Au-TiOPc interface or the barrier of the TiOPc-GaAs interface or a combination of both. It is clear that is not the Schottky barrier height of Au/GaAs interface, because the onset we measured is significantly higher then 0.9 eV.

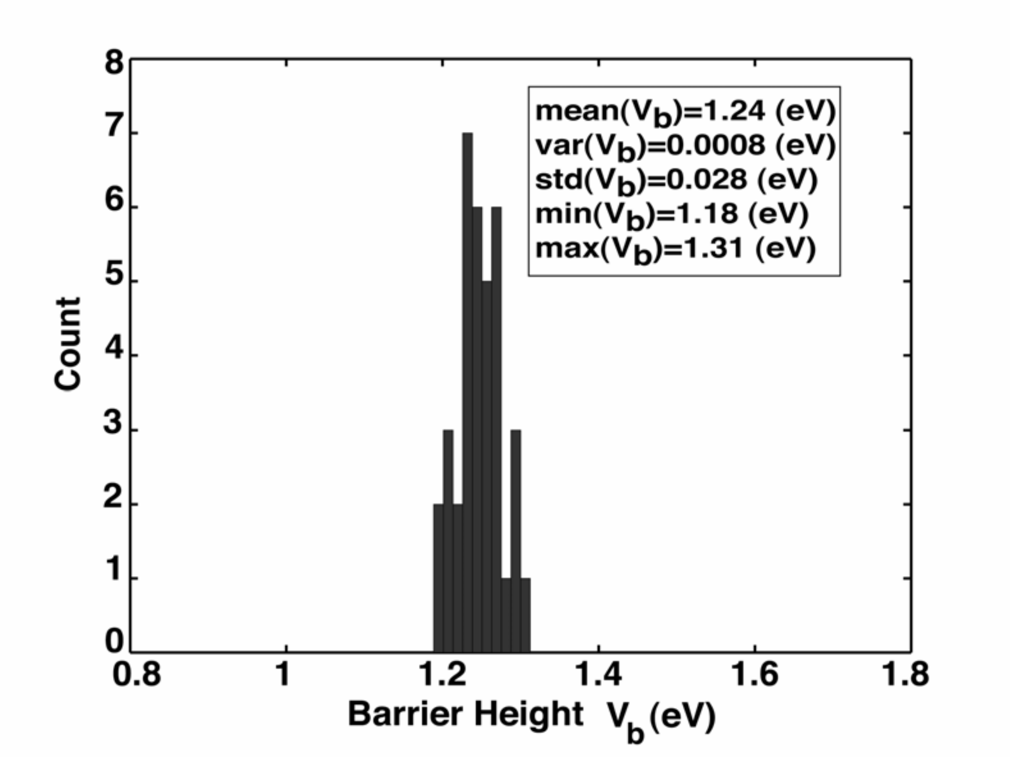

Fig. 2: Histogram of the measured barrier height of Au/TiOPc/GaAs (sample A).

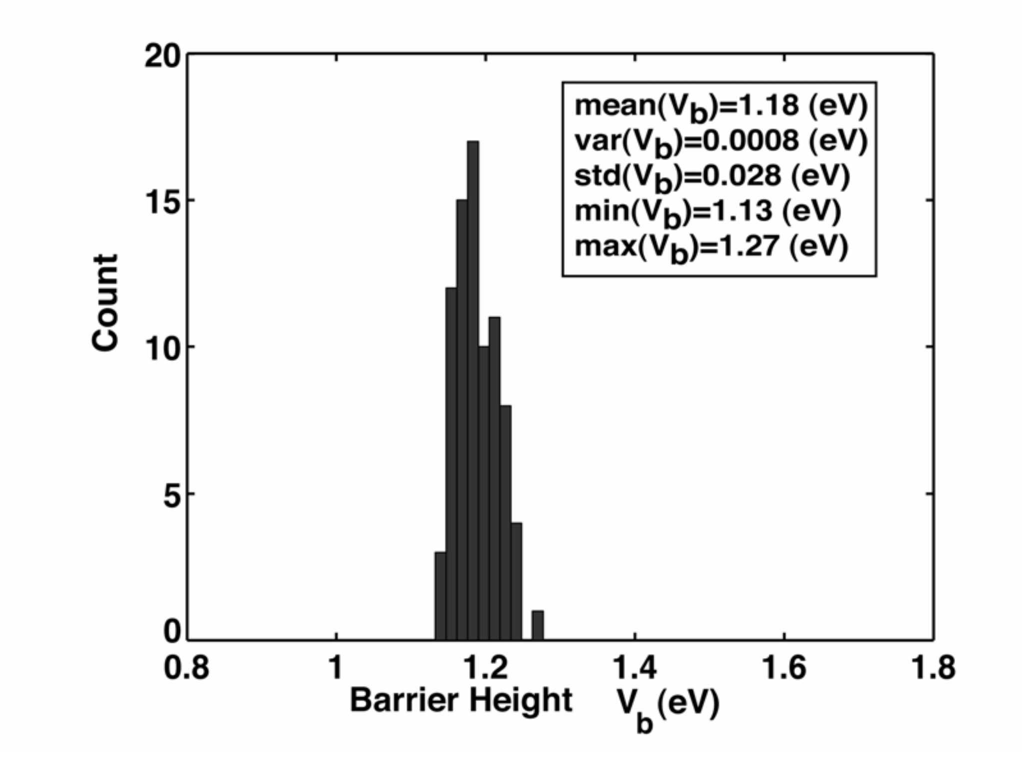

Fig. 3: Histogram of the measured barrier height of Au/TiOPc/GaAs (sample B).

The solid line in Fig. 4 shows averaged BEEM spectra (I_t = 5 nA, T = 300 K) and the dashed line is its first derivative taken of over 100 individual BEEM spectra. The spectra are taken over a voltage-range of 0.8 to 2.3 V. Above the onset several features are visible, three steps at the points: 1.34, 1.52 and 1.61 V. The same behavior of metal-organic interfaces was also found in [16] – [18]. Besides these features there are two significant peaks at 1.7 and 1.85 V. Above 2.3 V the data were not reliable, because of the increased signal to noise ratio.

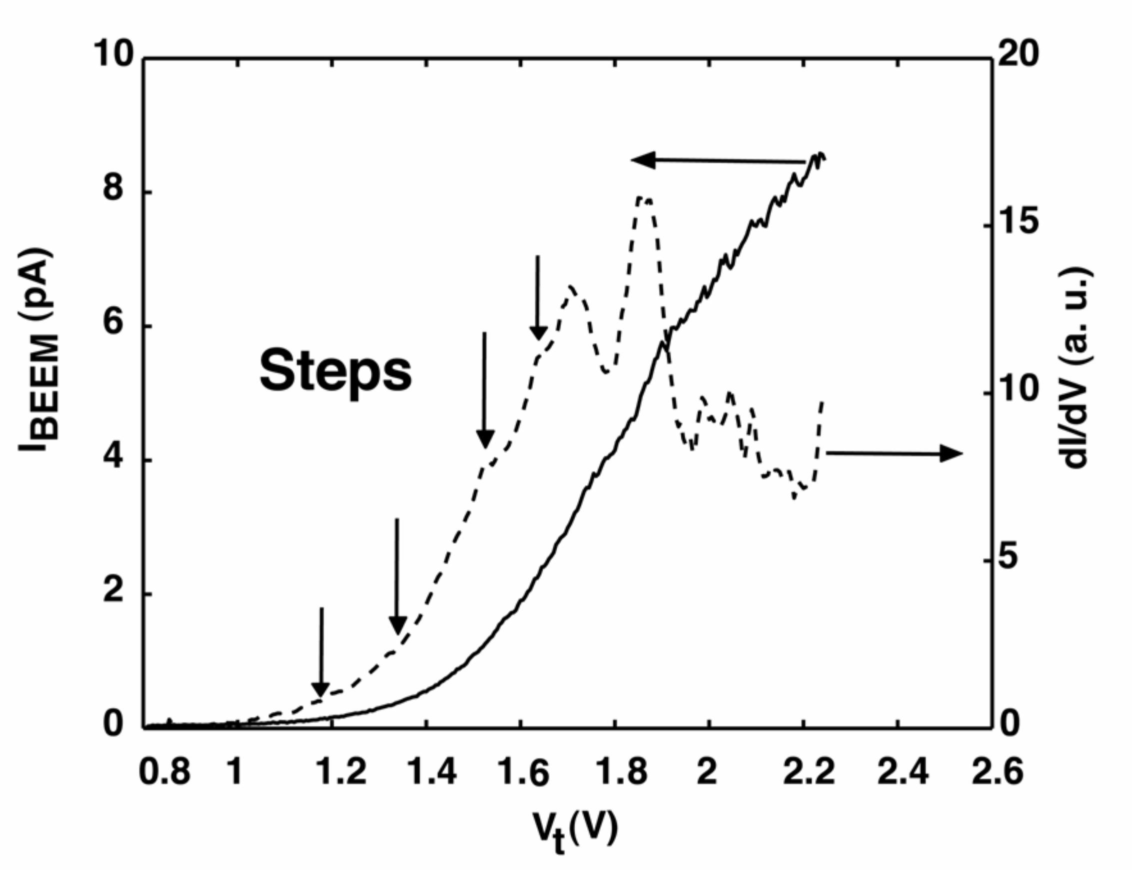

Fig. 4: Averaged BEEM spectra (solid line) and its first derivative (dashed line) from Au/TiOPc/GaAs. Multiple features are clearly visible in the first derivative.

Conclusion

Due to the BEEM images, it can be concluded that the samples are very homogeneous, in comparison to wet chemically manufactured organic films. All features visible in the BEEM images of our samples correlate exclusively with the granular structure and the topographic features of the Au-film and cannot be correlated to the organic film underneath. Analyzing the BEEM spectra we find that the TiOPc increases the BEEM threshold voltage compared to reference Au/GaAs diodes, which was also found in [19], where a BEEM study on a Au/Molecule/n-GaAs diode was done. The barrier height measured on the Au-TiOPc-GaAs is V_b ~ 1.2eV, which is in good agreement with the data found in references [1]. The results indicate that TiOPc functions as a p-type semiconductor, which is plausible since the measurements were carried out in air [2]. In addition, the derivative of the BEEM spectra shows multiple features in the energy regime above the LUMO level [2]. Possible origins of these features are currently under investigation.

Acknowledgments

The work presented here was financially supported by ”Fonds zur Förderung der wissentschaftlichen Forschung” (FWF), Project No. P16337N08 and the ”Gesellschaft für Mikro- and Nanoelektronik” (GME).

References

[1] T. Nishi, K. Tanai, Y. Cuchi, M. R. Willis, and K. Seki *Chem. Phys. Lett.*, vol. 414, pp. 479–482, 2005.

[2] K. Walzer, T. Toccoli, A. Pallaori, R. Verucchi, T. Fritz, K. Leo, A. Boschetti, and S. Iannotte *Surf. Scie.*, vol. 573, pp. 346–358, 2004.

[3] S. A. Jenckhe and J. A. Osaheni *Science*, vol. 265, p. 765, 1994.

[4] G. Yu, J. Gao, J. C. Hummelen, and A. J. Heeger *Science*, vol. 270, p. 1789, 1995.

[5] A. Dodabalapur, Z. Bao, A. Makhija, G. Laquindanum, V. R. Raju, Y. Feng, E. Katz, and J. Rogers *Appl. Phys. Lett.*, vol. 73, p. 142, 1998.

[6] C. J. Drury, C. M. L. Mutsaers, C. M. Hart, and D. M. Leeuw *Appl. Phys. Lett.*, vol. 73, p. 108, 1998.

[7] C. W. Tang *Appl. Phys. Lett.*, vol. 48, p. 183, 1986.

[8] T. Tsuzuki, Y. Kuwabara, W. Noma, Y. Shirota, and M. R. Willis *Jpn. J. Appl. Phys.*, vol. 35, p. 4, 1996.

[9] W. J. Kaiser and L. D. Bell *Phys. Rev. Lett.*, vol. 60, p. 1408, 1988.

[10] L. D. Bell and W. J. Kaiser *Phys. Rev. Lett.*, vol. 61, p. 2368, 1988.

[11] G. Binning, G. Rohrer, C. Gerber, and E. Weibel *Phys. Rev. Lett.*, vol. 49, p. 57, 1982.

[12] G. Binning, G. Rohrer, C. Gerber, and E. Weibel *Phys. Rev. Lett.*, vol. 50, p. 120, 1983.

[13] M. Prietsch *Phys. Rep.*, vol. 253, p. 163, 1995.

[14] V. Narayanamurti and M. Kozhevnikov *Phys. Rep.*, vol. 349, p. 447, 2001.

[15] J. Smoliner, D. Rakoczy, and M. Kast *Rep Prog. Phys.*, vol. 67, p. 1863, 2004.

[16] C. Troadec, D. Jie, L. Kunardi, S. J. O’Shea, and N. Chandrasekhar *Nanotech.*, vol. 15, p. 1818, 2004.

[17] C. Troadec, L. Kunardi, and N. Chandrasekhar *Appl. Phys. Lett.*, vol. 86, p. 072101, 2005.

[18] L. Kunardi and C. Troadec *J. Chem. Phys.*, vol. 122, p. 204702, 2005.

[19] W. Li, K. L. Kavanagh, C. M. Matzke, A. A. Talin, F. L´eonard, S-Faleev, and J. W. P. Hsu *J. Phys. Chem. B*, vol. 109, p. 6252, 2005.

In-situ X-Ray Diffraction during MOCVD of III-Nitrides: an Optimized Evaluation Algorithm

C. Simbrunner[1], K. Schmidegg[1], A. Bonanni[1], A. Kharchenko[2], J. Bethke[2], K. Lischka[3], H. Sitter[1]

[1] Institute of Semiconductor and Solid State Physics, University Linz, A-4040 Linz

[2] PANalytical B. V., Almelo, The Netherlands

[3] Department of Physics, University of Paderborn, Germany

Presently, we are able to measure in situ x-ray diffraction and spectroscopic ellipsometry simultaneously on rotating samples during the deposition process in our MOCVD reactor using a commercial available PANalytical Cu ceramic tube as x-ray source. Due to the natural wobbling of the rotating sample a compensation algorithm is used before adding up single spectra in order to improve signal to noise ratio before fitting procedure. In this paper we present an improved compensation algorithm based on a symmetric peak shape enabling the calculation of the peak symmetry axes from the centre of weight.

Introduction

Gallium nitride (GaN) and its alloys promise to be key materials for future heterojunction semiconductors devices aimed at high frequency, high power electronic applications [1]. However, manufacturing of such high performance products is challenged by reproducibility and material quality constraints that are notably higher than those required for optoelectronic applications. To meet this challenge, we already implemented, to our knowledge the first time, in situ x-ray diffraction (IXRD) for the metalorganic chemical vapor deposition (MOCVD) of III-nitrides as a real-time process tool using a standard x-ray source [2].

Presently, we are able to measure IXRD on rotating samples during the deposition process and in order to improve the signal to noise ratio a summation of single spectra is done. Because of the natural wobbling effects in MOCVD, all the single spectra are shifted with respect to each other. Therefore, a correction has to be done before adding up the channel intensities.

The algorithm used so far is based on peak maxima detection and the maximum intensity is interpreted as the peak centre defining the relative correction shift. In this paper we present a novel algorithm which takes into account also the surrounding of the peak maxima and results in more precise information on growth rate, composition and crystal quality.

Experimental Procedure

GaN and AlGaN layers are grown on c-plane sapphire substrates in an AIXTRON AIX 200~RF-S horizontal flow MOCVD reactor using standard techniques [3]. The substrate is rotating in the gas flow (about 15 rotations per minute) in order to improve the homogeneity of the growing layer.

On the reactor shell two Be windows enable the incidence of the x-rays focused by a Johansson monochromator and the detection of the diffracted beam. The x-ray setup consists of a PANalytical Cu x-ray source and a commercially available multichannel detector of the type X'Celerator [4]. Furthermore, an in-situ multi-wavelength spectroscopic ellipsometer (SE) provides additional information during growth.

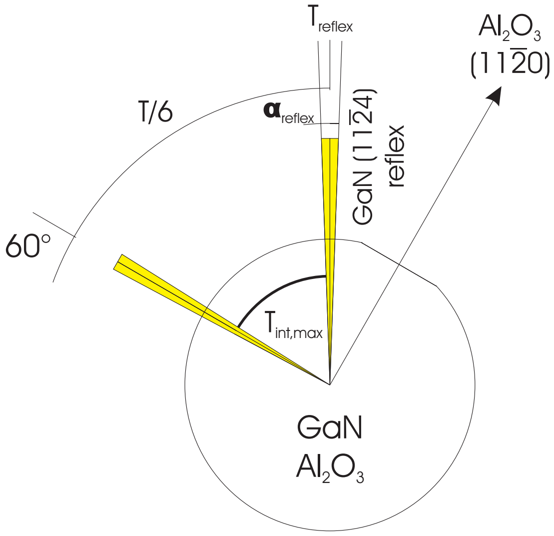

Fig. 1: Principal geometry of detected GaN (11-24) reflex (top view on the substrate).

The hexagonal GaN layer grows in the (0001) direction. The incident beam and the detector are adjusted in order to be sensitive to the (11-24) reflection of hexagonal GaN. Due to the hexagonal symmetry, the detector is illuminated six times per rotation period by a reflex which has an angular size defined by the angle α_{refl}. In connection with the rotation time of the sample (T) the time during which the reflex is visible for the detector (T_{refl}) is calculated by equation 1. To avoid a blur of the acquired spectrum only one GaN reflex must be included and this situation can be guaranteed by choosing a lower integration time than the critical integration time ($T_{\text{int,max}}$) which is defined by equation 1.

$$T_{\text{int,max}} = \frac{T}{6}\left(1 - T_{\text{reflex}}\right) = \frac{T}{6}\left(1 - \frac{\alpha_{\text{refl}}}{60}\right) \tag{1}$$

On the one hand the use of integration times (T_{int}) below the critical time $T_{\text{int, max}}$ ensures that never more than one reflex is included in the resulting spectrum. On the other hand the reduction of the integration time leads to an increase of the probability (p_{empty}) to get empty spectra, decreasing in this way the efficiency of the system. Equation (2) defines p_{empty} as being proportional to T_{reflex} and the chosen integration time T_{int}.

$$p_{\text{empty}} = 1 - \left(T_{\text{reflex}} + T_{\text{int}}\right)\frac{6}{T} \tag{2}$$

For the growth experiments, a constant integration time of about 90% of $T_{\text{int,max}}$ was used in order to ensure that only one reflex is included in the acquired spectrum, even if an increase of the rotation speed due to pressure or temperature changes in the growth chamber would take place.

In order to increase the signal to noise ratio, the single spectra have to be added up because of the unavoidable wobbling of the sample and due to the rotation during growth the spectra are shifted by an unknown angle in respect to each other. Previous works [2] report on an algorithm based on finding the maximum peak position (Pos_M) interpreted as the peak center and the point of reference. The results could be reasonable fitted at high enough spectral intensity expected at large layer thickness. An improved algorithm, working also at lower intensities, would represent a direct step toward an improved thickness resolution of the IXRD system.

For the results presented in this paper, we made use of a novel algorithm based on the fact that the reference peak has a symmetric shape. With this assumption the symmetry centre (Pos_{cw}) can be calculated from equation (3) by using the centre of weight of the reference peak. The detected maximum intensity of the spectrum (Pos_M) is taken as a first estimation of the centre of weight. The region around the maximum which should be included in the calculation can be defined by a constant (dk).

$$Pos_{cw} = \left(\sum_{k=Pos_M-dk}^{Pos_M+dk} I_k . x \right) \Bigg/ \left(\sum_{k=Pos_M-dk}^{Pos_M+dk} I_k \right) \qquad (3)$$

After compensation, the spectra are summed up and fitted by standard procedures [2].

Results and Discussion

By using the data acquired during a standard AlGaN growth process typical spectra are analyzed by both rotation compensating algorithms. After growing a GaN buffer on Al_2O_3 an $Al_{0.21}Ga_{0.79}N$ layer of about 500 nm is deposited and an IXRD spectrum is taken every 1.6 s. In order to improve the fitting results, 20 single spectra have been added after wobbling compensation and analyzed with both algorithms.

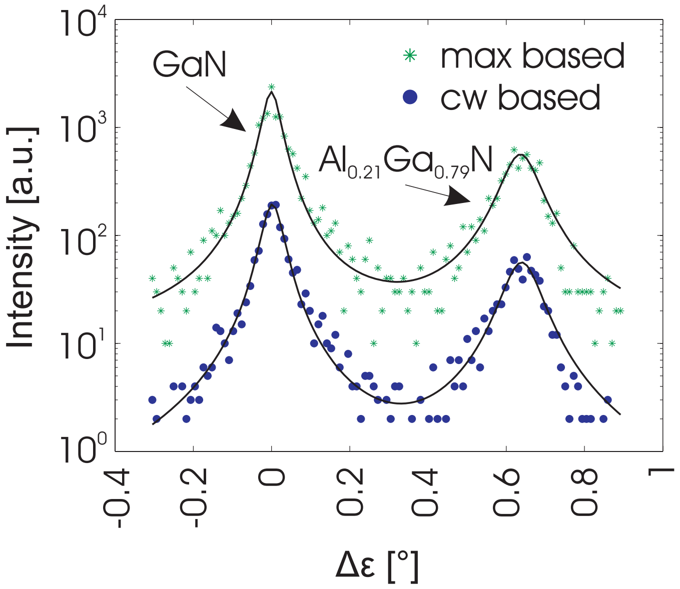

Fig. 2: 20 single spectra added up and fitted using the maximum based algorithm (star) and center of weight based algorithm (circles) as a function of angle Δε.

Figure 2 shows the intensity as a function of the diffraction angle of the scattered beam Δε relative to the GaN reference peak. A fit of the experimental points has been carried out by employing Pseudovoigt functions (solid lines).

For the top spectrum which is shifted for clarity by one order of magnitude represents the result by using the maximum based compensation algorithm. The fact that the channel with the maximum intensity is always shifted to $\Delta\varepsilon = 0$ results in a clearly visible overestimated peak intensity at this point. The lower spectrum (full dots) is the result of using the novel center of weight based algorithm which is not dominated by the previous described anomalous peak shape.

Summary

During MOCVD growth *in-situ* XRD spectra are acquired on rotating samples. In order to improve the signal to noise ratio the single spectra have to be added up before fitting procedure. Due to natural wobbling of the samples all single spectra are shifted in respect to each other which has to be compensated by an algorithm to avoid a blur of the added up spectra. We presented a new rotation compensation algorithm which is based on the symmetry of the peak all spectra are relatively shifted to. As a consequence the novel algorithm, taking into account also the surrounding of the peak maxima, results in a more precise information on growth rate, composition and crystal quality. Furthermore, the algorithm is more sensitive to small peak intensities, yielding an improved thickness resolution. The actual composition of the AlGaN layers could be determined already on a thickness of about 20 nm.

The obtained accuracy and the improved performance of the in-situ XRD setup represent a substantial step forward in the perspective of an effective closed-loop control of the MOCVD growth process.

Acknowledgements

The research was supported by the Austrian Foundation for Advancement of Scientific Research project P17169, and by PANalytical, Almelo, Netherlands. Part of the laboratory infrastructure was funded by the Austrian Gesellschaft für Mikroelektronik (GMe).

References

[1] S. C. Jain, M. Willander, J. Narayan, R. Van Overstraeten, J. Appl. Phys. 87 (3), 965-1006 (2000)

[2] C. Simbrunner, K. Schmidegg, A. Bonanni, A. Kharchenko, J. Bethke, J. Woitok, K. Lischka, H. Sitter, Phys. stat. sol. (a), (2006)

[3] A. Bonanni, D. Stifter, A. Montaigne-Ramil, K. Schmidegg, K. Hingerl, H. Sitter, J. Cryst. Growth 248, 211-215 (2003)

[4] A. Kharchenko, K. Lischka, K. Schmidegg, H. Sitter, J. Bethke, J. Woitok, Rev. Sci. Instrum. 76, 033101 (2005)

Technology
(Posters)

Comparative Study on the Impact of TiN and Mo Metal Gates on MOCVD-Grown HfO_2 and ZrO_2 High-κ Dielectrics for CMOS Technology

S. Abermann[1], G. Sjoblom[2], J. Efavi[3], M. Lemme[3], J. Olsson[2],
E. Bertagnolli[1]

[1] Institut für Festkörperelektronik,
Technische Universität Wien, A-1040 Wien, Austria

[2] Solid State Electronics Division, Uppsala University,
SE-752 37 Uppsala, Sweden

[3] Advanced Microelectronic Center, Aachen, AMO GmbH,
52074 Aachen, Germany

Introduction

The reduction of the equivalent oxide thickness (EOT) of the gate oxide has emerged as one of the most difficult tasks addressing future CMOS technology. In order to overcome gate tunneling, the introduction of so-called high-κ materials will be necessary [1]. Hafnium dioxide, HfO_2 [2], zirconium dioxide, ZrO_2 [3], and their silicates are assumed to be the most promising candidates to fulfil the crucial demands necessary for a successful integration of high-κ dielectrics into CMOS devices.

Along with the introduction of high-κ dielectrics, metal gates are anticipated to be introduced [1] to circumvent polysilicon-gate depletion [4] and high gate-resistance. *Mid-gap-metal* and *dual-work-function gate technology* are the two main concepts addressing the implementation of metal gates. Whereas TiN is a promising candidate to be applied as mid-gap metal gate [5], Mo is a suitable candidate for a single-metal, tunable dual-work-function technology [6].

By this work, we present a comprehensive study on Mo- and TiN MOS capacitors, including MOCVD-deposited ZrO_2 or HfO_2 as gate isolator, and the impact of annealing on slow and fast interface traps.

Experimental

As substrates we used boron-doped (100)-silicon wafers with a resistivity of 0.04 – 2.0 Ωcm. The substrates were subjected to a modified RCA-clean and a finalizing HF-dip immediately prior to deposition. ZrO_2 and HfO_2 thin films were deposited by MOCVD in a horizontal hot-wall reactor equipped with a bubbler system. Post-deposition annealing (PDA) of the samples was done in forming gas atmosphere (FGA) at 650°C. Subsequently, ~100 nm thick gate metals – in which the gate metal patterning was done by a lift-off process – were deposited on the high-κ dielectrics without capping to complete metal-oxide-semiconductor (MOS) capacitors. Finally, post-metallization annealing (PMA) in FGA and in some cases additionally high temperature annealing (RTA) in N_2 atmosphere has been applied.

Capacitance-Voltage (C-V) and Current-Voltage (I-V) characterizations have been performed, prior and after to the different annealing steps to evaluate electrical characteristics, respectively. To eliminate any parasitic series resistance in accumulation, all C-V curves have been corrected [7], and consequently EOT and Flatband voltage V_{FB} were deduced from quasistatic C-V measurements.

Results

Results for HfO_2 or ZrO_2 as gate dielectric are in general similar and comparable to each other. They revealed that PMA in FGA is effective in annealing out interface traps located in the Si bandgap in all investigated devices. Additionally, oxide charges are neutralized, as can be concluded from a shift of V_{FB} to more positive values in the C-V characteristics. The leakage current slightly rises due to PMA and we suppose thermodynamical reactions within the dielectrics during the thermal treatment to be responsible for this behavior.

The RTA treated samples exhibit a clearly decreased oxide charge density, but also an increase of C_{oxide} in accumulation, as well as an undesirable high leakage current. We therefore assume a crystallization process of the gate oxide that takes place during RTA and changes the bulk characteristics. High resolution-Transmission electron microscopy (HR-TEM) measurements, which reveal interfacial SiO_2 that might form already during PDA, support this assumption.

Titanium-Nitride Gate

Figure 1 shows C-V and I-V (inset) measurements for various frequencies for a TiN/ZrO_2/p-Si capacitor after PMA at 450°C in FGA. Only a small hump around ~0.25 V due to interface traps in the silicon bandgap can be seen. Up to at least 450°C, this gate stack shows thermodynamical stability.

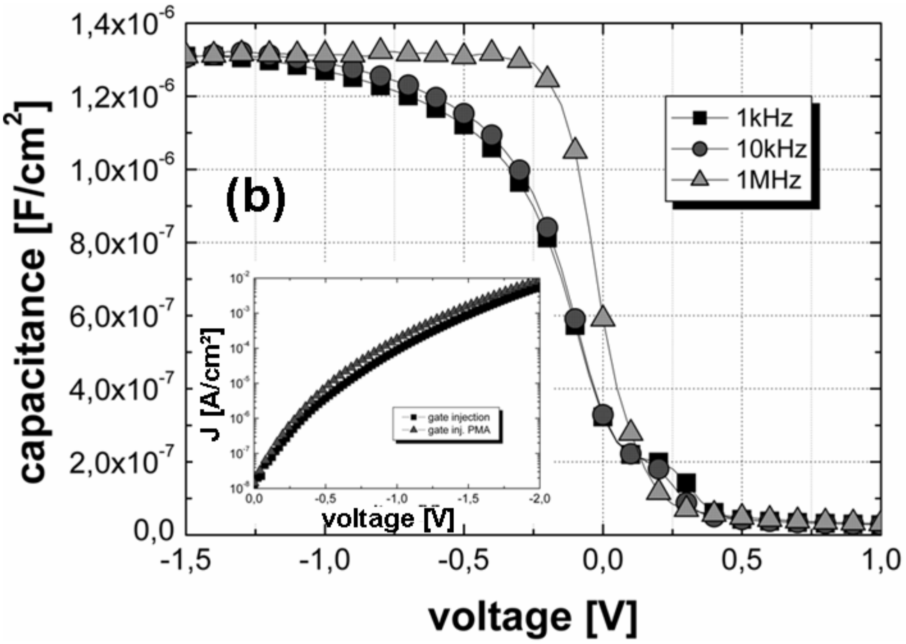

Fig. 1: C-V and I-V (inset) measurements of a TiN/ZrO_2/p-Si capacitor after PMA in FGA.

Molybdenum Gate

C-V and I-V (inset) measurements for various frequencies for a $Mo/HfO_2/p\text{-}Si$ capacitor are shown in Fig. 2. Thermal treatment included PMA at 450°C in FGA and RTA at 950°C in N_2. A hump around ~0.0 V due to interface traps in the silicon bandgap can be seen. Leakage current after RTA is undesirably high, probably due to crystallization of the gate oxide during annealing.

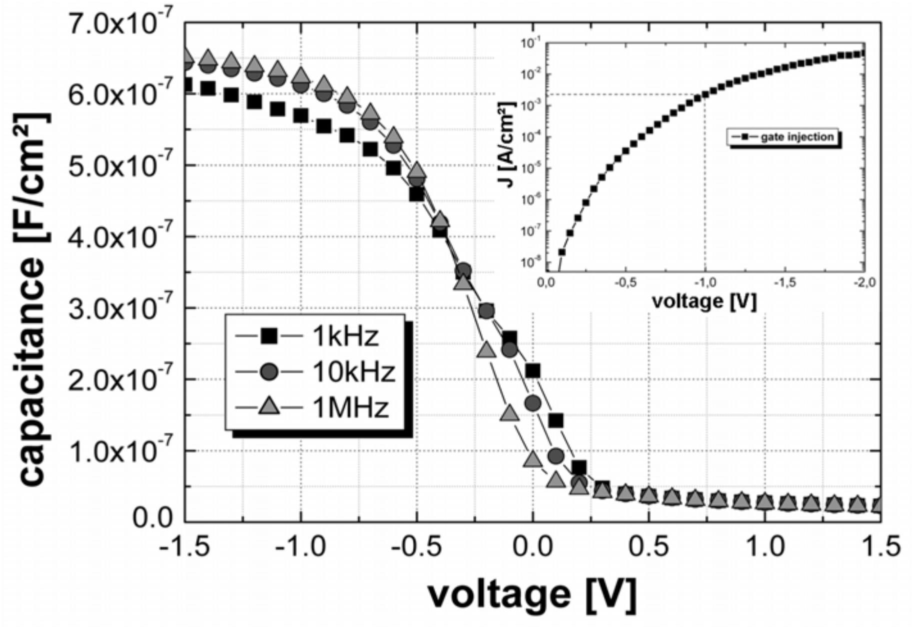

Fig. 2: C-V and I-V (inset) measurements of a $Mo/HfO_2/p\text{-}Si$ capacitor after PMA in FGA and RTA in N_2.

Summary

A summary of the investigated gate stacks is shown in table 1. The V_{FB} values for the TiN- and Mo-capacitors indicate mid-gap pinning of the metal gates. One can see that the values of κ do not correlate with the corresponding EOT; a trade-off between EOT and κ is observed. This might be due to different contributions of an unintentional interfacial SiO_2 layer forming during the growth process and its further increase during post deposition annealing treatments.

Gate material:	TiN (PMA)	Mo (PMA+RTA)
EOT [nm]:	2.0	3.4
Diel. constant κ [1]:	12	23
Flatb. Volt. V_{FB} [V]	-0.05	-0.16
Ox. Dens. Q_0 [cm^{-2}]	1.1E+12	1.2E+10

Table 1: Summary of TiN- and $Mo/ZrO_2/Si$ stacks.

Acknowledgements

This work is supported by the *Network of Excellence SINANO*. The *Gesellschaft für Mikro- und Nanoelektronik*, *GMe*, as well as the *Zentrum für Mikro- und Nanostrukturen*, *ZMNS*, are gratefully acknowledged for support.

References

[1] *International Technology Roadmap for Semiconductors*, 2005 Edition, http://public.itrs.net/.

[2] Y.-S. Lin, et al., *Appl. Phys. Lett*. 81, 2041 (2002).

[3] S. Lysaght, et al., *J. Non-Crystal. Solids* 303, 54 (2002).

[4] S. Youn, et al., *Vac. Sci. Technol. A* 19(4), 1591 (2001).

[5] M. Lemme et al., *Microel. Reliability* 45, 953 (2005)

[6] Q. Lu et al., *Symp. on VLSI Technology* 72-73 (2000)

[7] K. Kwa,et al., *Semic. Sci. & Tech.* 18, 82 (2003).

Structuring of Organic Semiconductors by Optical Lithography

K. Forberich[1], T. Fromherz[2], K.Hingerl[1], M. Morana[3], C.Brabec[3]

[1] CD-Labor für Oberflächenoptische Methoden, Institut für Halbleiter- und Festkörperphysik, Altenbergerstraße 69, A-4040 Linz

[2] Institut für Halbleiter- und Festkörperphysik,
Altenbergerstr. 69, A-4040 Linz

[3] Konarka Austria, Konarka Austria Forschungs und Entwicklungs GmbH,
Altenbergerstraße 69, A-4040 Linz

Introduction

Organic semiconductors are now in wide use for devices such as OFETs, OLEDs and organic solar cells. However, the transport properties like for example the carrier mobility of these materials are not completely understood. Carrier mobility is usually determined from the dependence of the saturation current on the applied gate voltage of a field effect transistor (FET). These results reflect the mobility under large electric fields. Information about the low field mobility can be extracted from Hall measurements, which have been done for small molecule organic semiconductors [1], but not for conjugated polymers. In order to produce the well-defined Hall bar that is necessary for these measurements, we developed a process to structure a thin layer of an organic semiconductor. In the development of this process, care was taken to protect the semiconductor from oxygen and UV-radiation. In order to monitor the residual influence of the process on the organic semiconductor, FET structures were fabricated by the same process. In addition, Structuring organic semiconductors can also be useful for other applications, for example in a FET where a well-defined structure would reduce the leakage current, or for the definition of pixels in an organic photodetector.

Experimental

Sample Preparation

We start with silicon substrates with a 230 nm oxide layer. Gold contacts are applied by lithography, evaporation and subsequent liftoff (Fig. 1). The organic semiconductor Poly(3-hexyl)thiophen (P3HT) is then spin-coated onto this structure. As the next step, three additional layers are applied on top: photoresist (~1.4 µm), gold (~50 – 100 nm) and a second layer of photoresist (~1.8 µm). The top layer of photoresist is structured by optical lithography and the gold that is not covered by the remaining photoresist is removed by wet chemical etching.

Subsequently, the samples are etched in an oxygen plasma so that all the exposed organic materials are removed. The remaining gold layer acts as an etch mask. In addition, the gold protects the semiconductor form the detrimental influence of UV radiation and oxygen during the whole process. After the etching, the photoresist and gold on top of the polymer layer are removed in a liftoff step with acetone. The smallest feature size that was demonstrated with this process is about 10 µm.

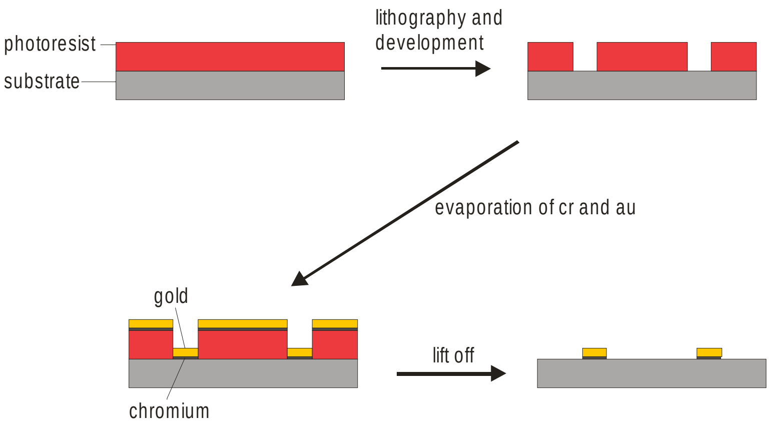

Fig. 1: Process steps for the contacts.

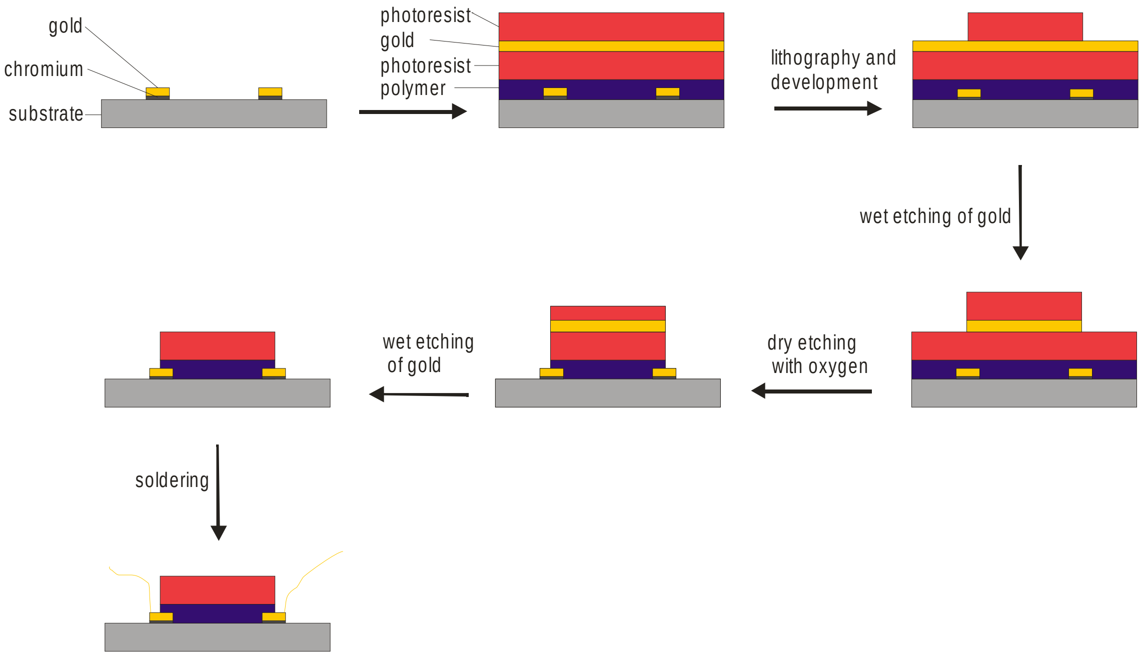

Fig. 2: Process steps for the structuring of the organic semiconductor.

Measurements

To examine the influence of the process steps on the electrical properties of the organic semiconductor, one of the structures on our samples was an OFET geometry with a channel length of 10 µm and a channel width of 1 cm. The transistor characteristics were measured before and after the structuring of the semiconductor layer, the results are shown in Figs. 3 and 4.

These measurements show that the conductivity of the P3HT-layer was increased by one to two orders of magnitude as a consequence of the process steps. The dependence of the source-drain-current on the applied gate voltage decreases accordingly. We interpret these results as being caused by unintentional doping of the P3HT during one of the process steps in spite of the protective gold layer. Up to now, it is not clear during which of the process steps sketched in Fig. 2 the oxygen doping predominantly occurs. The identification and improvement of this step has to be the subject of future work.

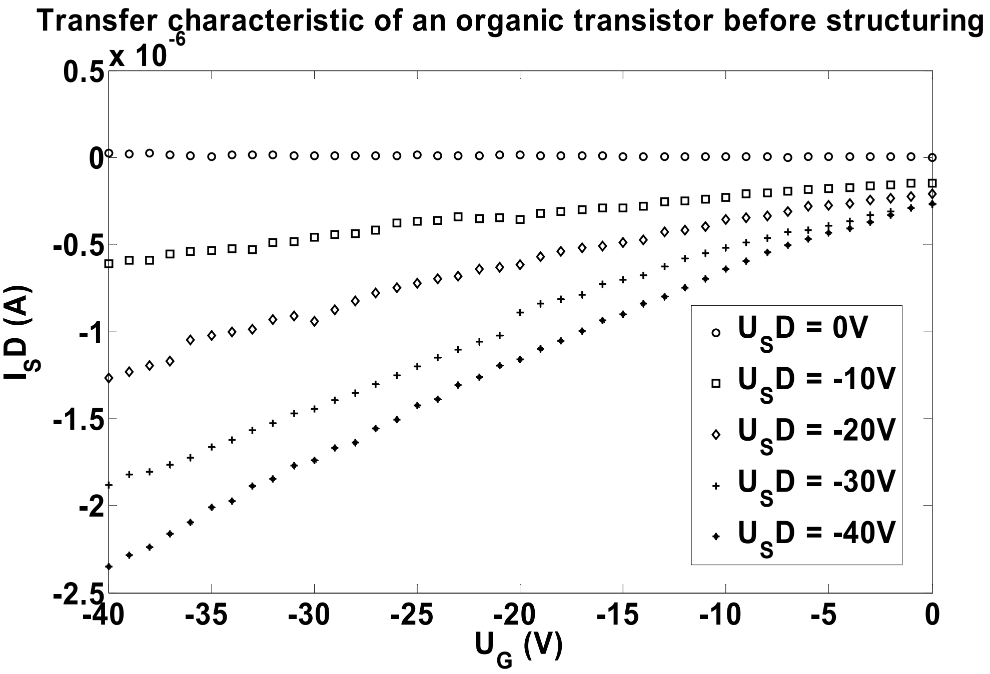

Fig. 3: Transfer characteristics of an organic field effect transistor before structuring the semiconductor.

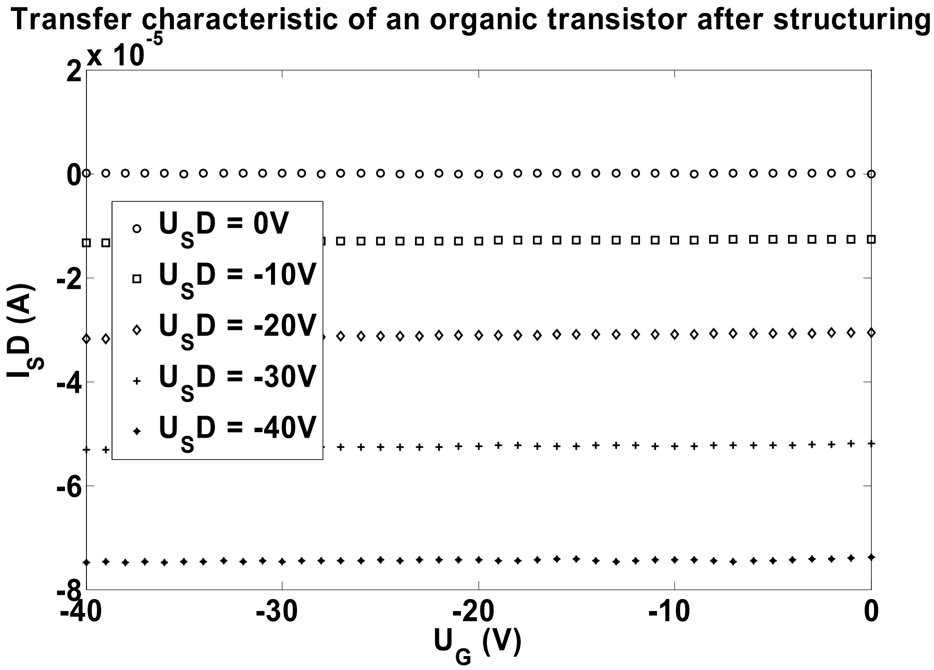

Fig. 4: Transfer characteristics of an organic field effect transistor after structuring the semiconductor.

Conclusion

We have shown that organic semiconductors can be structured by a combination of optical lithography and oxygen etching. Reference measurements on a transistor showed that the semiconductor was doped by oxygen during the process. The influence of the particular process steps has yet to be examined carefully, so that those steps can be modified in order to prevent or reduce the doping of the semiconductor. The experiments were done for P3HT. In principle, this process can be applied to any organic semiconductor, but the influence of the process on the electrical properties of the semiconductor might differ.

References

[1] V. Podzorov et al., *PRL* **95**, 226601 (2005)

Nanodots, Nanowires, and Nanocrystals (Posters)

Focused Ion Beam Induced Nanodot, Nanocrystal and Nanofiber Growth

C. Schoendorfer, A. Lugstein, E. Bertagnolli

Vienna University of Technology, Department for Solid State Electronics,
Floragasse 7, A-1040 Vienna, Austria

Introduction

Ion beams focused to diameters in the range of several tens of nanometers offer an interesting opportunity for maskless processing in the nanoscale regime. Under certain sputter conditions a periodic height modulation in the form of ripples and dots on a submicron length scale develops during broad beam ion exposure as observed for semiconductor materials [1] – [4], metals [5], [6], insulator surfaces [7], and semimetals (e.g., graphite [8]). To gain full use of FIB techniques a fundamental understanding of the interaction of ion beams with the substrate material is required.

In this paper, we investigate the impact of FIB irradiation on GaAs, InAs, GaSb and Sb substrates and discuss the surface evolution. We will show, that under proper FIB adjustment of beam energy, beam diameter and beam current dots, crystals and fibers form due to selective etching and catalytic growth processes.

Experimental

Sample Preparation

In a twin lens FIB system Ga^+ ions are extracted from a liquid Ga source, followed by acceleration up to 50 keV. The beam scanning in discrete steps across the sample surface leads to an ion bombardment of a defined area. Controlled FIB exposure of the sample is achieved by variation of some basic parameters such as the beam diameter, the beam current, the distance between two discrete steps along the scanning path and the dwell time which is the time the beam remains on each spot. The experiments are carried out with various ion fluences at normal incidence and at room temperature.

Our setup offers the possibility to image the focal plane during FIB processing. Therefore the surface evolution can be observed in-situ by FIB-SEM imaging. Furthermore, the nanopatterns are investigated by atomic force microscopy (AFM), Auger electron spectroscopy (AES), high resolution transmission electron microscopy (HRTEM) and X-ray diffraction.

GaAs Substrates

The exposure of GaAs to the FIB leads to an excess of Ga on the substrate surface due to preferential sputtering of As [9]. Because of the surface tension the Ga agglomerates dots. Therefore, a formation of Ga-rich liquid droplets in the ion exposed area as shown in the SEM image in Fig. 1(a) can be observed. *In-situ* monitoring shows that these dots move around on the surface as long as this area is exposed to the FIB. Topography investigations by AFM have shown agglomeration of the droplets due to gathering at lower levels of the roughened surface which is displayed in Fig. 1(b). The chemical composition of the dots has been analyzed by AES which confirmed that the droplets consist of nearly pure Ga.

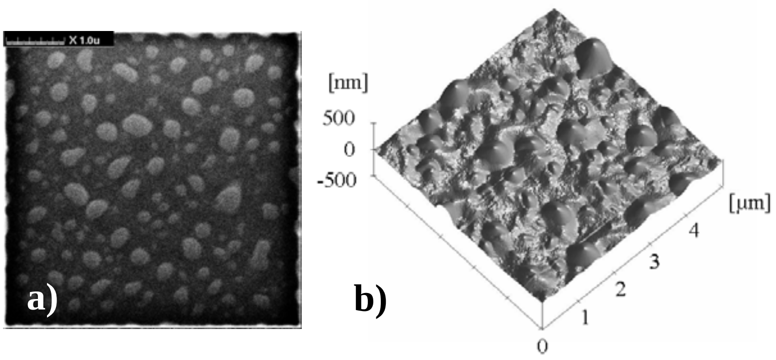

Fig. 1: (a) FIB-SEM image of a GaAs surface after FIB exposure of a 5 µm x 5 µm box with 50 keV Ga ions, (b) AFM topography of the GaAs sample after milling.

InAs Substrates

Figure 2 shows SEM images of the InAs surface after 50 keV FIB exposure with different ion fluences. For an ion fluence of 1.25x10^{16} ions/cm^{2} randomly distributed nanograins are formed on the InAs surface (Fig. 2(a)). The extension size of these grains ranges from 30 to 120 nm and their typical number density is in the order of about 2x10^{9} cm^{-2}. For an ion fluence of 2.5x10^{16} ions/cm^{2} the size of the protrusions increases while the surface density decreases (Fig. 2(b)). For the highest investigated ion fluence of 5x10^{16} ions/cm^{2} the grains grow further and emerge as well separated crystallites with obvious facets (Fig. 2(c)).

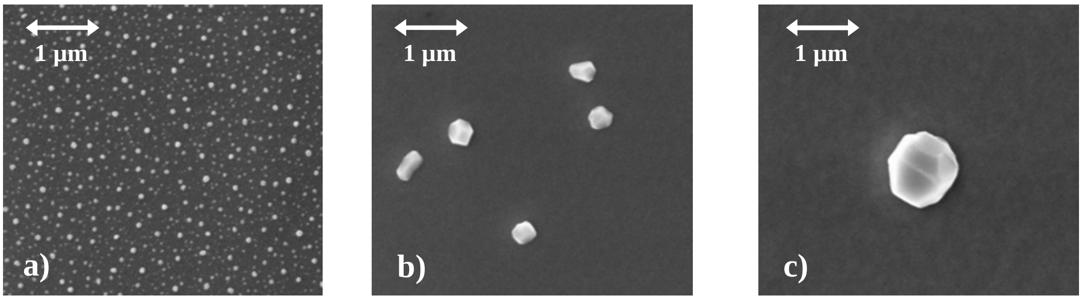

Fig. 2: Ion fluence dependency of pattern evolution on InAs exposed by the Ga FIB. The SEM images show the InAs surface after exposure fluences of (a) 1.25x10^{16} ions/cm^{2}, (b) 2.5x10^{16} ions/cm^{2} and (c) 5x10^{16} ions/cm^{2}.

An explanation for this effect of an excess of In on the surface can be found in the different sputter rates of In and As. The mass difference implies that indium is sputter ejected at a much lower rate than arsenic which in addition to that is highly volatile when being in an atomic state. Due to this preferential sputtering of arsenic during FIB bombardment an excess of indium is formed on the exposed InAs surface. We assume that these excess indium atoms presumably diffuse on the ion-impacted surface, coalescing into islands or crystallites somewhere on the surface. To prove the assumption of In crystallite formation due to FIB exposure X-ray diffraction measurements are carried out, where the three most intense reflections of crystalline In are clearly visible.

Relative intensities and d spacings of these reflections are in good agreement with reference material [10].

GaSb Substrates

The impact of the Ga FIB depositing different ion fluences on GaSb substrates can be retraced by the SEM images in Fig. 3. At the beginning of the exposure process beneath a thin surface layer a structure consisting of many hollow cells like a honeycomb is built. This is a result of the conglomeration of voids in the subsurface induced by the implanted Ga ions [11]. Ongoing milling leads to a transformation of the comb structure into a sponge-like network consisting of Ga and Sb in the same ratio including some Ga-rich precipitations on top of this fiber network. We assume that a catalytic growth process similar to the vapor-liquid-solid growth process [12] occurs, whereby the Ga droplets act as the needed catalytic particles.

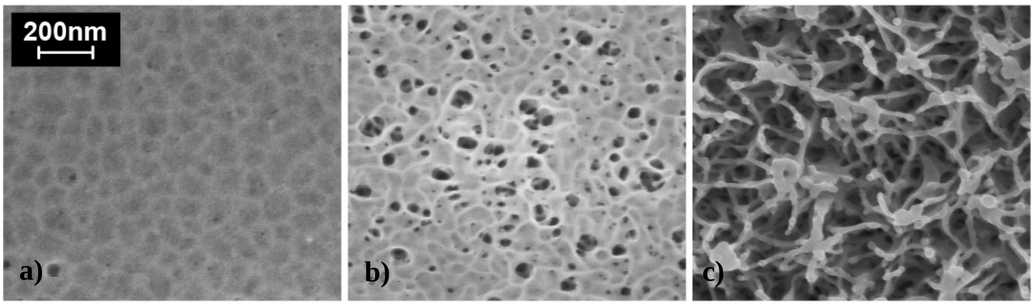

Fig. 3: GaSb surface evolution driven by ion fluence: depositing an ion fluence of $3x10^{13}$ ions/cm² (a) leads to generation of hollow combs under a thin surface layer, increasing the fluence to $6x10^{13}$ ions/cm² (b) results in a more and more porous layer and finally at an ion fluences of $3x10^{14}$ ions/cm² a transformation into a sponge-like network built up of GaSb fibers with diameter in the range of 25 nm and Ga-rich precipitations takes place.

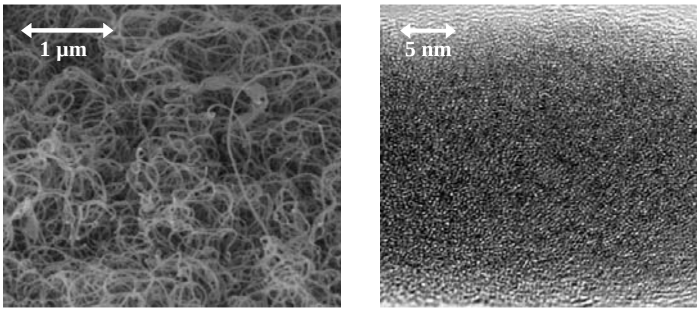

Fig. 4: The SEM image shows FIB generated Sb nanofibers with diameters in the order of 20 nm (a) and the HRTEM image of an individual Sb nanofiber proves that the as-grown nanofiber is completely amorphous even in the nanometer scale.

Sb Substrates

The results of GaSb substrates exposed to the FIB lead to the idea that fibers growth could also occur using pure Sb as substrate. The catalyst material needed for the growth may be provided by the focused Ga beam. In Fig. 4(a) a SEM image of an FIB milled box on metallic antimony using 50 keV Ga ions at an ion fluence of 2×10^{16} ions/cm² is given. The Sb nanofibers similar to those found on GaSb show diameters of few tens of nanometers and seem to grow in slops beginning and ending at the substrate surface. HRTEM (Fig. 4 (b)) and AES investigations show that these fiber structures are completely amorphous and consist of pure Sb.

Summary

In summary, investigation of FIB bombardment of several substrates is done. It is demonstrated that FIB parameters and the chemical composition of the substrates show a great influence on the surface evolution. Various effects which lead to different appearance in the sample surface evolution, such as Ga droplets on GaAs, In nanocrystals on InAs and nanowires with diameters in the range of few tens of nanometers on GaSb and metallic Sb, are studied by SEM and AFM. In addition to that the resulting nanostructures are investigated in detail using HRTEM, AES and XRD techniques to gain more information about the chemical composition and crystallographic structure. Thus, e.g. the In nanostructures can be considered to be crystalline and the as-grown Sb nanowires to be completely amorphous and to consist of pure Sb.

Acknowledgements

This work is partly funded by the Austrian Science Fund (Project No. 18080-N07). The authors would like to thank the Center for Micro- and Nanostructures (ZMNS) for providing the clean-room facilities, Christian Tomastik for AES measurements and Johannes Bernardi for HRTEM investigations. The financial support from the Austrian Society for Micro- and Nanoelectronics (GMe) is gratefully acknowledged.

References

[1] E. Chason, T. M. Mayer, B. K. Kellerman, D. T. McIlroy, and A. J. Howard, Phys. Rev. Lett. 72, 3040 (1994).

[2] G. Carter and V. Vishnyakov, Phys. Rev. B 54, 17647 (1996).

[3] Z. X. Jiang and P. F. A. Alkemade, Appl. Phys. Lett. 73, 315 (1998).

[4] J. Erlebacher, M. J. Aziz, E. Chason, M. B. Sinclair, and J. A. Floro, Phys. Rev. Lett. 82, 2330 (1999).

[5] S. Rusponi, C. Boragno, and U. Valbusa, Phys. Rev. Lett. 78, 2795 (1997).

[6] S. Rusponi, G. Costantini, C. Boragno, and U. Valbusa, Phys. Rev. Lett. 81, 4184 (1998).

[7] T. M. Mayer, E. Chason, and A. J. Howard, J. Appl. Phys. 76, 1633 (1994).

[8] S. Habenicht, W. Bolse, K. P. Lieb, K. Reimann, and U. Geyer, Phys. Rev. B 60, R2200 (1999).

[9] J. G. Pellerin, D. P. Griffis, P. E. Russell, J. Vac. Sci. Technol. B 8, 1945 (1990).

[10] The Powder Diffraction File, International Centre for Diffraction Data, 12 Campus Boulevard, Newton Square, Pennsylvania 19073-3273, USA.

[11] N. Nitta, M. Taniwaki, Y. Hayashi, T. Yoshiie, J. Appl. Phys. 92, 1799 (2002).

[12] R. S. Wagner, W. C. Ellis, Appl. Phys. Lett. 4, 89 (1964).

Fabrication of Narrow Split Contacts for Nanocrystal Investigations

M. Niedermayr, G. Pillwein, W. Heiss, G. Brunthaler

Institut für Halbleiter- und Festkörperphysik, Johannes-Kepler-Universität, A-4040 Linz

A simple method for producing metallic electrodes with gaps below 10 nm is presented. The fabrication of these electrodes is achieved by electron beam (e-beam) lithography and shadow evaporation. Thereby the gap width can be adjusted directly by the exposure time in the lithography process. At the moment we can create gaps as small as 4 nm. In later investigations such electrodes will be used for electrical transport studies of nanocrystals made of different materials and sizes.

Introduction

Using colloidal techniques, nanocrystals can be made of different materials [1]. The size of these nanocrystals can be easily changed via the fabrication conditions. The size is e.g. ranging from 5 to 15 nm for IV-VI semiconductors. For investigation of electrical transport properties it is necessary to have electrodes with different gap sizes fitting to the size of the nanocrystals. One way of producing them is by e-beam lithography using a scanning electron microscope (SEM) combined with shadow evaporation.

A single electron transistor can be fabricated with a nanocrystal in between two electrodes and in combination with an additional gate [2] (see Fig. 1). Such a device has the same behavior as common quantum dots produced by lithography processes [3]. In this case, the electrons tunnel one by one from the source electrode to the nanocrystal and from the nanocrystal to the drain electrode. This current is switched on and off by the applied gate voltage from the conducting p-Si substrate which is isolated with the oxide layer from the contacts.

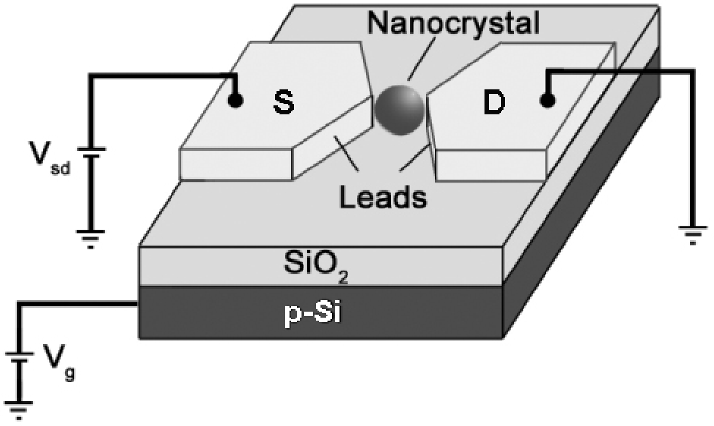

Fig. 1: Schematic picture of a nanocrystal single electron device consisting of two side contacts and an underlying conducting substrate as a plunger gate.

Experimental

The used high-doped Si substrates have a 100 nm thick SiO_2 cover layer. First they are consecutively cleaned in acetone, trichloroethylene, acetone and methanol in an ultrasonic bath for 5 minutes each. The positive photoresist Allresist AR-P 671.04 950K is spun onto the substrates at 6000 rpm for 1 minute. The photoresist is made of a solution of 4% 950K PMMA in chlorobenzene. Therewith a uniform layer with a thickness of 250 nm is achieved. The coated substrates were annealed at 160 °C for 60 minutes. Afterwards the samples are exposed with a Leo 35 scanning electron microscope. The required mask was designed with the ELPHY Plus software. In order to find the ideal mask design, different contact tip shapes were tested. We get the best results with obtuse tip shapes.

After exposure the contact electrode shape is created in the photoresist layer by putting it into a developer and a stopper for 2 minutes and 30 seconds, respectively. The samples are evaporated with an 8 nm Cr layer and a 50 nm Au layer, where the Cr layer ensures a good mechanical contact between SiO_2 and gold. In a lift-off process, the residual photoresist together with the metallic layers on top of it is removed at 75°C for 2 hours.

To apply an external voltage to the contact electrodes bonding pads are required. These pads are produced by optical lithography using the photoresist Shipley S1813 at 4000 rpm for 1 minute, baking at 90°C for 10 minutes and UV-exposure through a mask. After resist development, a 300 nm Al layer is deposited and the remaining resist is removed again. We could produce electrodes with gaps as small as 10 nm with this method.

Because of electron scattering an undercut is formed into the photoresist. Between the two electrodes the resist is so small that the undercuts are overlapping and we get a kind of bridge (Fig. 2(a)).

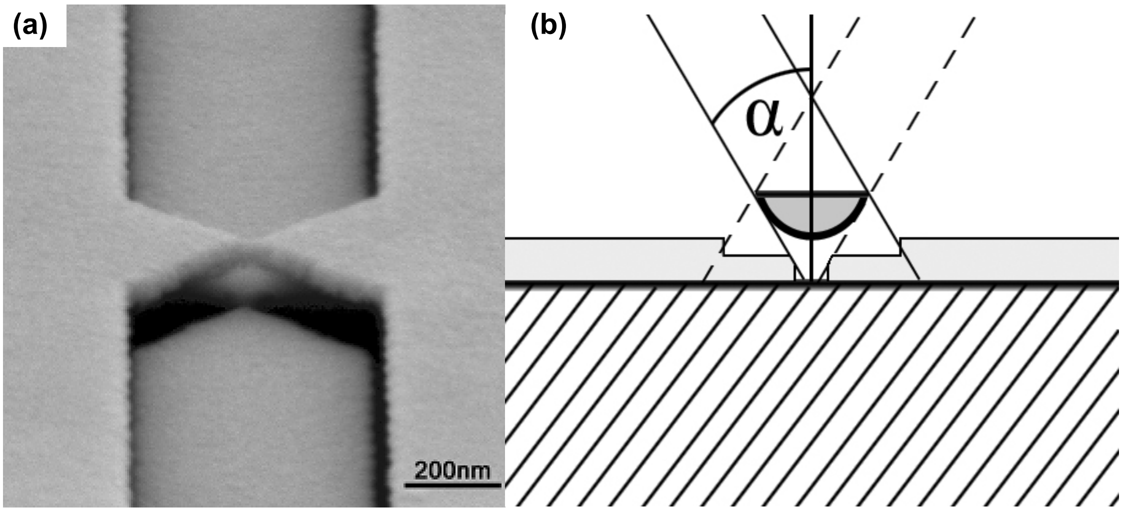

Fig. 2: (a) SEM picture of two electrodes after evaporation and before lift off; you can see the photoresist bridge covered by the Cr and Au layer; (b) schematic picture of cross section of the photoresist bridge during shadow evaporation; the first layer is deposited from right at angle of -α, the second one is deposited from left at angle α

By using shadow evaporation we can reduce the width of the gap. For this we deposited two gold layers with a thickness of 25 nm at α = +/- 6.67° instead of one 50 nm layer at normal incidence (Fig. 2(b)). With this technique gaps up to 4 nm are possible (Fig. 3).

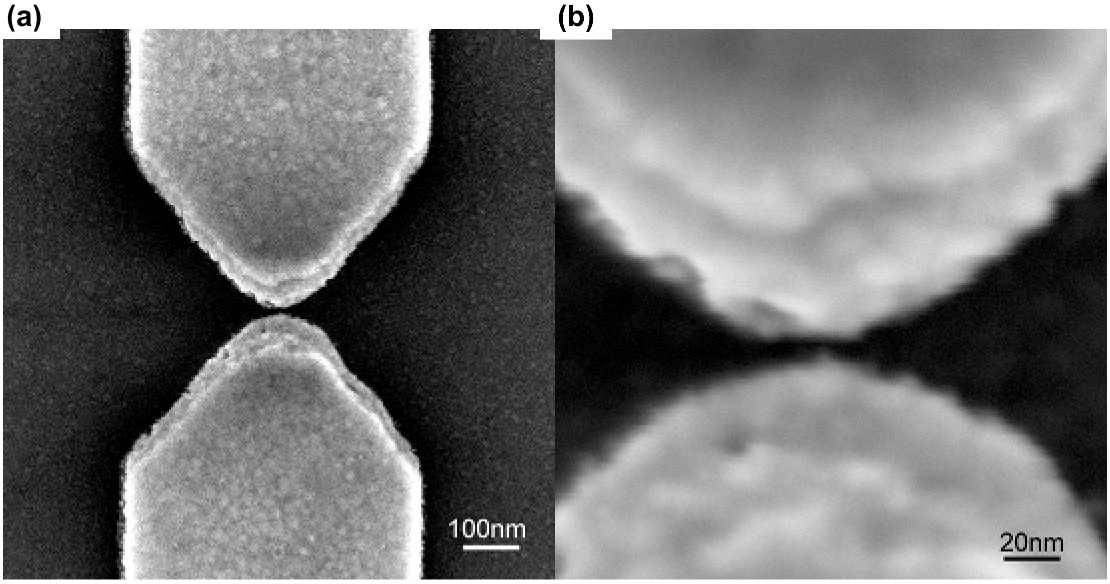

Fig. 3: SEM pictures of a pair of electrodes with different magnifications; gap width: 5.5 nm

To get the nanocrystal onto the substrate, the drop casting method is used (Fig. 4). You can see in picture Fig. 4(b), there are a lot of crystals between the electrodes. However, for general transport studies, and especially studies on the nanocrystal-SET, we just want charge transport through one single nanocrystal. However the tunneling exponential decay length is very small. A simple estimation determines this length to 1 Å. Thus, the electrons can only tunnel into well placed nanocrystals.

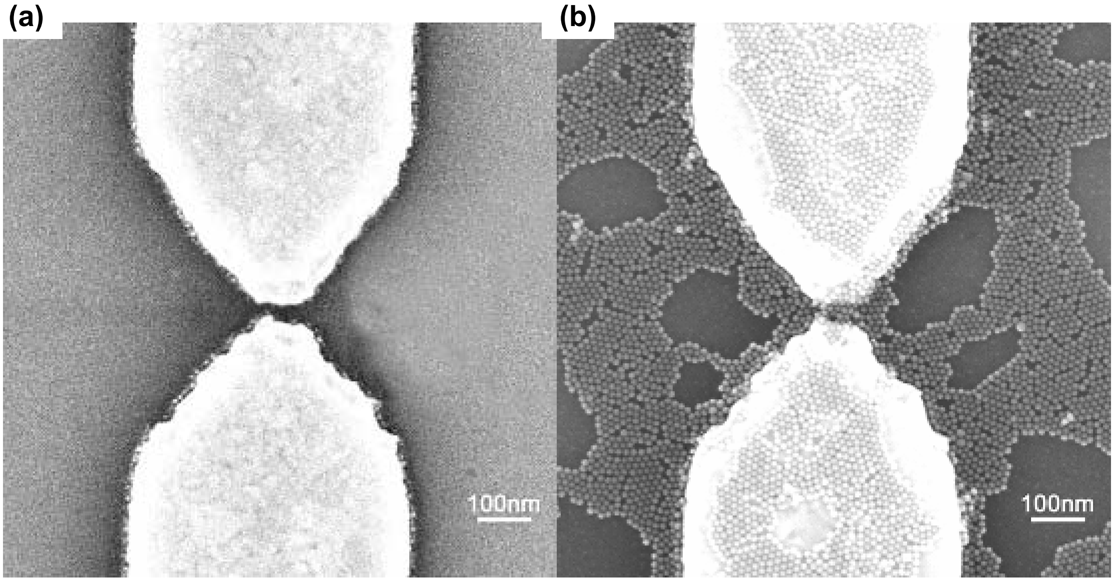

Fig. 4: SEM picture of a pair of electrodes; (a) before drop casting (b) after drop casting FeO nanocrystal (d = 12nm)

Conclusion

A simple technique has been developed to fabricate electrodes with sub-10 nm gaps. In future experiments these electrodes will be used to investigate electrical transport through nanocrystals and SET made of nanocrystals with Si substrate as back gate.

Acknowledgements

Work was supported by “Fonds zur Förderung der wissenschaftlichen Forschung” (Austrian Science Fonds) Project P16160.

References

[1] M. Kovalenko, E. Kaufmann, D. Pachinger, J. Roither, M. Huber, J. Stangl, G. Hesser, F. Schäffler, W. Heiss : “Colloidal HgTe Nanocrystals with Widely Tunable Narrow Band Gap Energies: From Telecommunications to Molecular Vibrations”, J.Am.Chem.Soc., 128, 3516-3517 (2006)

[2] D. L. Klein, R. Roth, A.K.L. Lim, A.P. Alivisatos, P.L. McEuen : “A single-electron transistor made from cadmium selenide nanocrystal”, Nature, 389, 699-701 (1997)

[3] U. Meirav E.B. Foxman, “Single-Electron Phenomena in Semiconductors”, Semicond. Sci. Technol. 10, 255 (1995).

Au-free Epitaxial Growth of $InAs_{1-x}P_x$ Nanowires

B. Mandl, J. Stangl, M. Brehm, T. Fromherz, G. Bauer

Institute for Semiconductor and Solid State Physics,
University of Linz, A-4040 Linz

T. Mårtensson, L. Samuelson, W. Seifert

Department for Solid State Physics, S-221 00 Lund University, Sweden

InAs and $InAs_{1-x}P_x$ nanowires have been grown by the use of a metal-organic vapor phase epitaxy. The nanowire growth is initiated by a thin SiO_x layer deposited on the substrate prior to growth. The wires exhibit a non-tapered shape with a hexagonal cross section. Further the growth of InAs on Si is demonstrated as well as the growth on a pre-patterned InP (111)B substrate.

Introduction

Semiconductor nanowires as one-dimensional structures and building blocks for nanodevices have received increased attention in recent years. Controlling the one-dimensional growth on a nanometer scale offers unique opportunities for combining materials, manipulating properties, and designing novel devices. We present a general method to produce epitaxial nanowires of InAs, without using Au-particles as catalyst. It has been shown that InAs nanowires can easily be contacted and gated. With inbuilt barriers (e.g. InP), the functionality of such structures in single electron transistors [1] and resonant tunneling devices [2] has been demonstrated.

Moreover, InAs has a high potential to be used complementary in combination with Si for high-mobility applications. For this purpose, however, nanowires grown Au-assisted impose severe restrictions due to the introduction of deep-level defects into Si. We show in this report that InAs nanowires can be obtained epitaxially on various substrates without any metal catalyst when one covers the substrates by a thin layer of SiO_x ($x \approx 1$) prior to InAs growth. X-ray diffraction measurements indicate that the wires form in part in the wurtzite modification and grow spontaneously in c-direction [000.1], equivalent to the cubic [111] direction.

Experimental

For wire-growth we used low pressure metal organic vapor phase epitaxy (LP-MOVPE) at a pressure of 10 kPa, with trimethylindium (TMI), arsine (AsH_3), and phosphine (PH_3) as precursor materials, transported in a flow of 6000 ml/min of H_2 as carrier gas. For the precursors typical molar fractions of 2×10^{-6} for TMI and 2×10^{-4} for AsH_3 were used. For TMI also higher molar fractions were tested, but had no significant effect on the growth rate. The molar fractions for PH_3 were varied between 3.5 and 15×10^{-3}. As substrates we used epitaxy-ready III/V wafers and Si wafers. In case of Si substrates, the native oxide was removed by an HF dip. Before loading the substrates into the growth chamber, a thin SiO_x layer was sublimated onto the surface. The substrates were then heated to the growth temperature between 520 °C and 680 °C in H_2 atmosphere. As soon as growth temperature was reached, the precursors were switched on simultaneously. The growth was stopped by switching off the TMI source, and the samples were cooled under AsH_3 flow, or for $InAs_{1-x}P_x$ deposition, under additional PH_3 flow. To characterize the wires we employed scanning electron microscopy (SEM) and x-ray diffraction (XRD). SEM investigations were performed using a JEOL 6400 and a LEO 150 microscope. From SEM we obtain the length, orientation, shape, and density of the wires.

XRD experiments have been performed at beamline 10B (Troïka II) at the ESRF in Grenoble, to get information on the orientation of the wires relative to the used substrate and relative to each other, about the lattice constant and the crystalline structure of the wires. SEM images of InAs wires grown at different temperatures on InP (111)B surfaces, covered by 1.3 nm SiO_x prior to growth, are presented in Fig. 1. We observe the following trends:

(i) The wires grow spontaneously on the InP(111)-surface and appear epitaxially oriented, i.e., they are standing vertically on the surface and grow in continuation of the substrate [111]B orientation. Remarkably, the wires are homogeneously thick, i.e., in contrast to typical MOVPE wire growth [3], [4], we cannot determine any measurable tapering and also no thickening at the wire foot/substrate connection.

(ii) In general, the growth temperatures are much higher than for Au-assisted growth of InAs nanowires in MOVPE, where growth suddenly ceases when the temperature exceeds 500 °C. The wire length is not a linear function of time: in parallel investigations, not presented here, we have seen that the length growth rate starts with a high value and decreases then over time according a power law $R \sim t^n$ ($n \approx -0.5$). This fact can be seen as a hint on the growth mechanism.

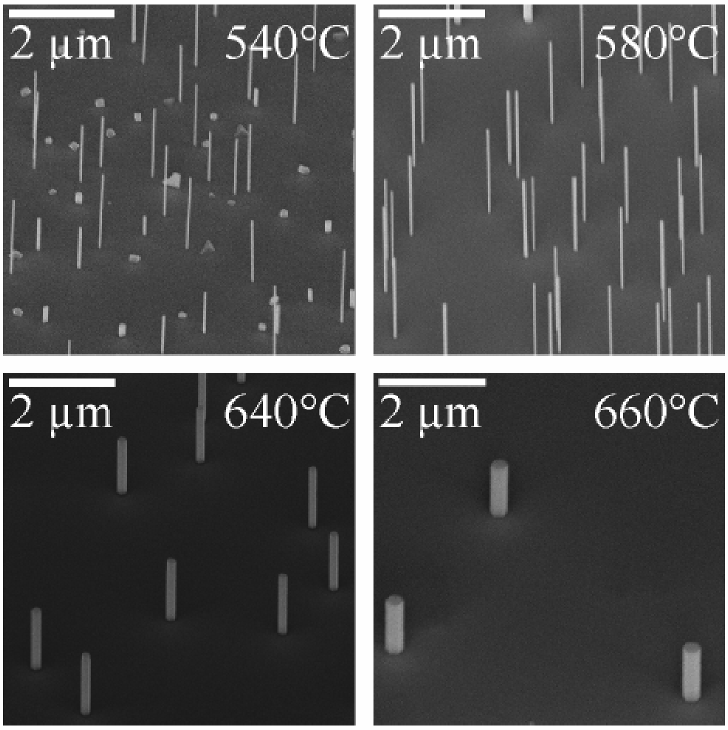

Fig. 1: SEM images (45° tilt) of InAs wires grown on InP (111)B at different temperatures, growth time was 60 s [5].

(iii) The wire density is also a function of growth temperature. In general, the density decreases with increasing temperature. This indicates that there are relations to the general laws which govern the nucleation kinetics of clusters on surfaces, where the density ρ of critical nuclei follows the general proportionality $\rho \sim R/D(T)$, with R the deposition rate and D(T) the temperature-dependent coefficient of surface diffusion. This result indicates that clusters may be involved in pre-stages of wire growth. At higher temperatures these clusters grow anisotropically and form one-dimensional wires. At lower temperature only a part of the clusters adopts this growth mechanism, others grow by isotropic expansion instead. In fact, we find that at low temperatures the wires compete with InAs-clusters on the surface (see the 540 °C sample in Fig. 1).

(iv) In parallel to the decreasing density, the aspect ratio length/width of the wires decreases with increasing temperature: At higher temperatures the radial growth on the side facets gets more and more important. At the highest growth temperature of 680 °C, the aspect ratio dropped down to below 1 and we obtained epitaxially grown hexagonal platelets.

(v) The morphology of the nanowires is rod-shaped with a regular hexagonal cross-section. The top of the wires is flat, visible at least in case of the thicker wires grown at higher temperatures. From x-ray diffraction experiments performed at ID01 at the ESRF Grenoble it follows that the structure of the wires is in part wurtzite, which is the thermodynamically metastable modification of InAs.

By using different materials as substrate, the influence of the lattice mismatch on the wire growth was investigated. For this study different epiready III-V (111)B substrates (InAs, InP, GaAs, and GaP) as well as Si (001) substrate are used. With these substrates, a range of lattice mismatches up to 12% (InAs/Si) is covered, with all substrates, epitaxial wire growth along [111]B could be demonstrated, indicating that the lattice mismatch poses no restriction for the wire growth.

Position controlled nucleation of InAs nanowire is demonstrated when using a pre-patterned InP (111)B substrate. The pattern is defined by electron beam lithography, SiO_x and a subsequent e-beam resist lift-off. For structured substrates, a slightly different growth sequence was used, in that the precursors are activated at 500 °C during the heating of the samples to 580 °C, wires are growing on the positions defined by the SiO_x patches. Such a patterned nucleation can be seen in Fig. 2(a). It has to be mentioned that the wires are nucleated by patches remaining on the substrate surface, in difference to processes where openings in a SiO_2 layer are used to control the growth position of III-V nanowires [7].

Another result of this study is the successful growth of InAs nanowires on Si (001) and Si (111), nucleated using a 1.3 nm thick SiO_x layer instead of Au as nucleation centers [8]. Before the deposition of the SiO_x layer, the native oxide is removed by a HF etch. The wires grow in the four incline [111] directions on the Si (001) substrate. For the growth on such substrates, the exposure of the substrate to Oxygen prior to the growth is critical. Such a growth mechanism opens the possibility to use InAs as high mobility semiconductor on Si, without making use of Au particles that are detrimental for the performance of Si based electronics.

Further, the growth of $InAs_{1-x}P_{x,}$ as a III-V alloy is demonstrated. The growth is done similar to InAs, on a InP (111)B substrate with a 1.3 nm thick SiO_x layer. As precursor material Phosphine is used in addition to TMI and Arsine. The growth results in wires very similar to those of InAs, with a constant diameter, showing no tapering and no thickening at the wire foot/substrate interface and show a hexagonal cross-section, again the wires grow in the <111>B direction, continuing the substrate orientation. The wires are shown in Fig. 2(a). In photoluminescence and XRD measurements a change of the energy gap and the lattice constant as a function of the Phosphine flux is found, demonstrating a significant phosphorus incorporation into the wires [9]. The maximum concentration of P in the wires so far achieved is estimated to be $x = 0.17$.

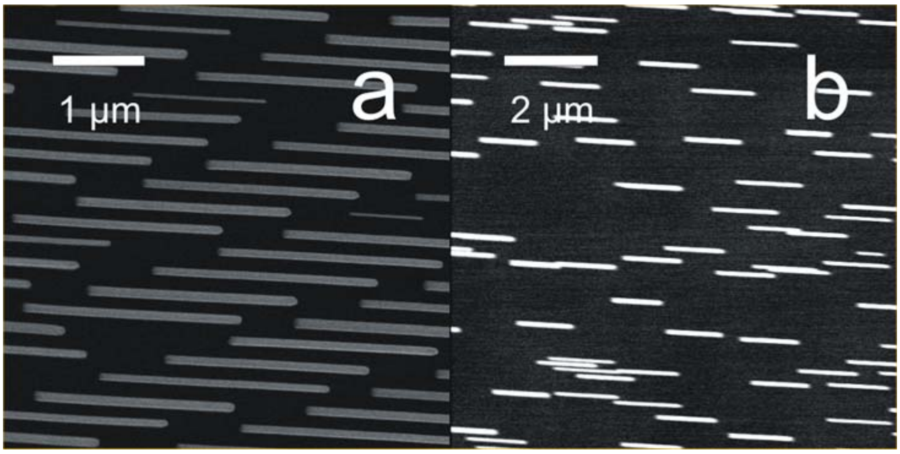

Fig. 2: 45° tilt SEM images of a) InAs nanowires grown using a pre-patterned SiO_x layer on an InP (111)B substrate. b) SEM image of $InAs_{1-x}P_x$ nanowires (45° tilt) grown at InP (111)B at 620 °C for 60 s [9].

Conclusion

We demonstrate a novel mechanism for the growth of InAs and $InAs_{1-x}P_x$ nanowires which relies on a SiO_x layer deposited at the substrate surface. This growth mechanism shows epitaxial grown wires with homogeneous shape. The wire growth rate is depending on the growth temperature and growth time. Also, the density of the wire nucleation is depending on the growth temperature indicating a growth initialized by clusters formed on the substrate prior to wire formation. In addition the wire length to width ratio is found to be temperature dependent. From XRD measurements the existence of a wurtzite phase together with the zinkblende phase is found for the wire crystal structure. Additional to the growth on InP, various III-V and even Si substrates were used, showing no influence of strain on the wire growth. The demonstrated growth of InAs wires on Si substrates in the absence of metal catalysts opens a promising route for integrating III-V high mobility devices with standard Si based electronics. In addition, the growth of wires on a pre-patterned substrate is demonstrated with a high yield for the wire nucleation on pre defined positions. Also, the growth of $InAs_{1-x}P_x$ wires is demonstrated, opening the possibility to grow additional III-V materials and heterostructures by this method.

References

[1] M. T. Björk *et al.*, Nano Letters **2**, 87 (2002)

[2] C. Thelander *et al.*, Appl. Phys. Lett. **83**, 2052 (2002)

[3] K. Hiruma *et al.*, J. Appl. Phys. **77**, 447 (1997)

[4] W. Seifert *et al.*, J. Cryst. Growth **272**, 211 (2004)

[5] K. A. Dick *et al.*, Nano Letters **5**, 761 (2005)

[6] B. Mandl *et al.*, Nano Letters **6**, 1817 (2006)

[7] M. Inari *et al.*, Physica E **21**, 620 (2004)

[8] T. Mårtensson *et al.*, Nano Letters **4**, 1987 (2004)

[9] B. Mandl *et al.*, ICPS conference proceedings (in press)

Si/SiGe (Posters)

Stranski-Krastanov Growth of Tensely Strained Si on Ge (001) Substrates

D. Pachinger, H. Lichtenberger, F. Schäffler

Institut für Halbleiter- und Festkörperphysik,
Johannes-Kepler-Universität Linz, A - 4040 Linz

Introduction

In the Si/SiGe heterosystem self-organization schemes based on Stranski-Krastanov (SK) growth were mainly investigated for compressively strained Ge layers on Si substrates, which offer hole confinement in the islands. Due to the Type II band alignment, electron confinement requires tensely strained, Si-rich dots, which can be realized on Ge substrates or pseudosubstrates. Very little is known about SK growth of Si on Ge, but there are strong indications that dot formation is kinetically hampered, if the epilayer is under tensile strain [1]. On the other hand, SK growth is driven by total energy minimization, and since the elastic energy depends quadratically on strain, close to thermal equilibrium 3D island formation is not expected to depend on the sign of the lattice mismatch. Indeed, SK growth has already been observed in tensely strained layers, e.g. in the PbSe/$Pb_{1-x}Eu_xTe$ heterosystem [2].

Here, we report on MBE growth conditions for Si island formation on Ge(001) substrates. Buffer layer growth was optimized and Si island formation was investigated in the temperature range between 550 and 750 °C for 5 to 15 ML Si coverage. Seeded nucleation was observed after carbon pre-deposition on a Ge buffer layer. Finally, Ge substrates were pre-structured to offer suitable nucleation sites for the Si islands.

Experimental

Substrates used in this study were Ga-doped Cz-Ge(100) wafers with a resistivity of about 8 Ωcm. Pieces of 17,5 x 17,5 mm were chemically pre-cleaned [3] and loaded into our Riber SIVA45 MBE system via a load lock system, followed by an *in-situ* thermal oxide desorption step at 750 °C for 15 minutes.

AFM measurements were carried out for the characterization of buffer and island growth. Surface orientation maps extracted from these AFM images were used for facet analysis.

Pre-structuring of the Ge substrates was realized by e-beam lithography with a Leo Supra 35 FE-SEM at 20 kV and subsequent reactive ion etching in an Oxford Plasmalab 80 reactor with 100 % CF_4. (50 sccm CF_4 flow, 30 W, 50 mTorr pressure). The etch rate was about 100 nm/min for the chosen parameters.

Results

After oxide desorption a Ge buffer layer was deposited to smoothen the roughness of the substrate. By systematically varying its deposition temperature, we found that a 50 nm thick Ge buffer grown at 400 °C offers the lowest mean-root-square roughness of about 0.1 nm (Fig. 1).

A nearly ideal surface with large terraces separated by one- and two-atomic height steps is created.

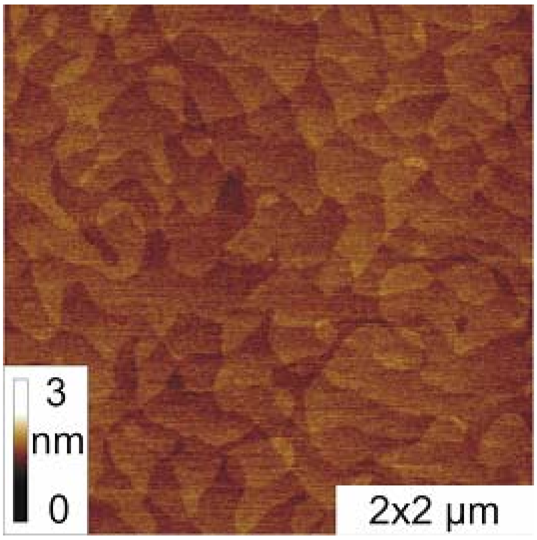

Fig. 1: AFM image of a 50 nm thick Ge buffer layer on a Ge (001) substrate grown at 400 °C providing a mean-root-square roughness of about 0.1 nm. Flat areas seen in the image are separated by one- and two-atomic height steps.

On this buffer we deposited 5 – 15 ML of Si at temperatures between 550 °C and 750 °C. Island formation was observed at the highest deposition temperature (Fig. 2(A)), but these islands were almost complete alloyed with the Ge substrate. Lowering the growth temperature to 550 °C leads to a drastic reduction of the dot density and to a pronounced trench around the islands (Fig. 2(B)).

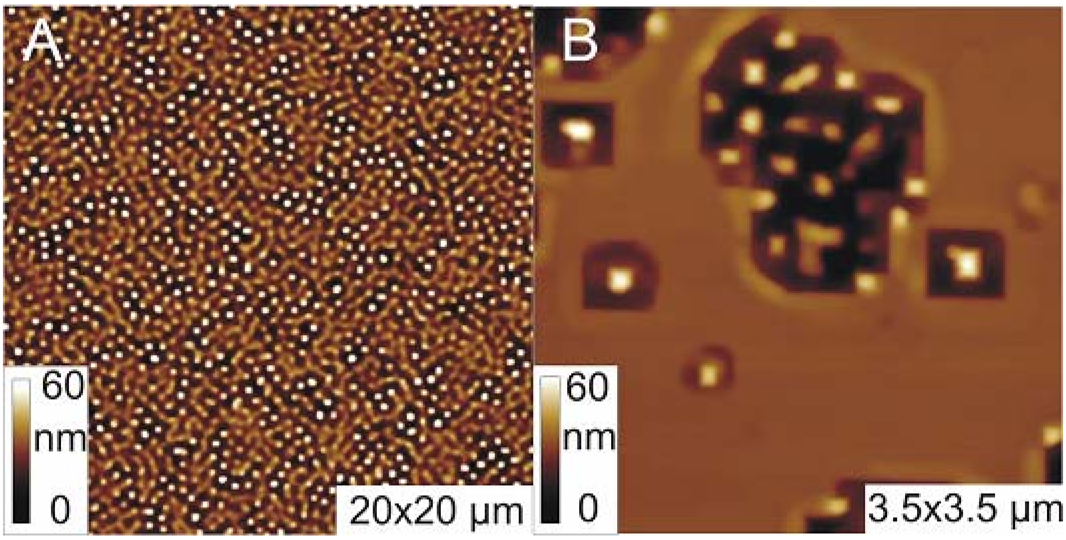

Fig. 2: (A): AFM images of 10 ML Si grown on a 50 nm Ge buffer layer at 750 °C showing a dot density of $4x10^8$ cm^{-2}; (B): AFM images of 10 ML Si grown on a 50 nm Ge buffer layer at 675 °C, showing coupled and uncoupled trenches enclosing the dots; dot density is $3x10^8$ cm^{-2}

These experiments confirm the kinetically restricted nucleation of Si islands at lower growth temperatures, which is, in our case, the only temperature range where alloying with the buffer layer can be efficiently suppressed. It is therefore essential to enhance island formation in tensile strained films by providing suitable nucleation centers. For this purpose we deposited a fraction of a ML of carbon onto the Ge buffer layer just prior to Si deposition. With carbon pre-deposition varying from 0.05 to 0.5 ML, Si island growth could be observed over the whole range of growth temperatures investigated (Fig. 3).

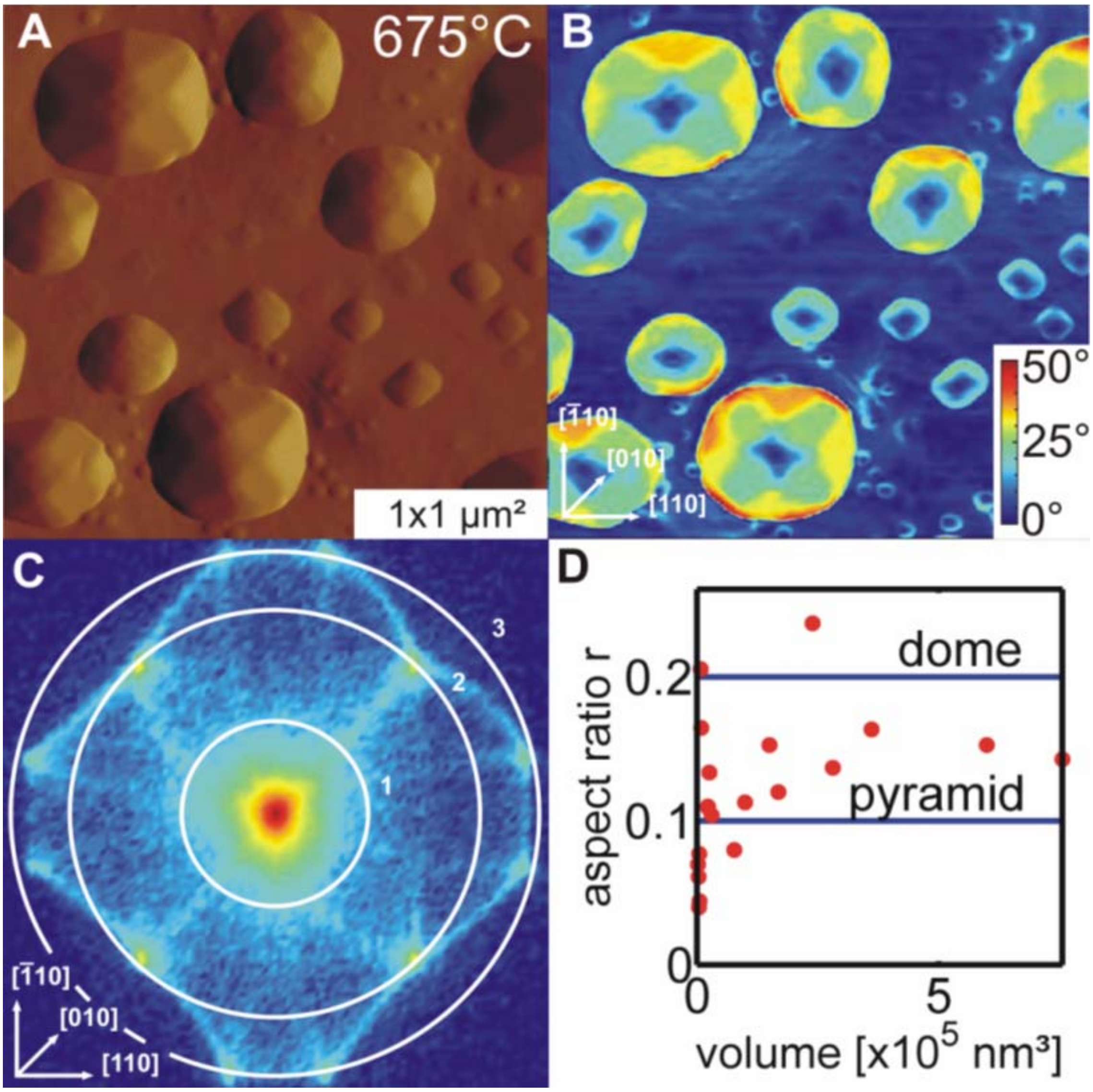

Fig. 3: (A): AFM image in the derivative mode of 15 ML Si grown on 50 nm Ge buffer layer at 675 °C after 0.1 ML carbon predepostion on the buffer layer; (B): Surface angle plot and surface orientation map extracted from figure (A) show 1: {105}, 2: {113} and {15 3 23} facets, which are the same characteristic facets found for dome-shaped and pyramidal-shaped Ge dots on Si (figure (B) and (C)). Aspect ratio distribution of the sample grown at 675°C can be seen in Fig. (D).

Extracting surface orientation maps from the AFM images we found for both growth conditions Si-rich islands with {105}, {113} and {15 3 23} facets (Fig. 3 (B)). These are the same characteristic facets found for SiGe islands on Si, indicating that Si also forms the well-known dome-shaped and pyramid-shaped islands [4]. Especially the appearance of the {105} facet, which can clearly be seen on the topmost parts of the dome-shaped islands in Fig. 3(A), is somewhat surprising, because it is usually associated with a facet that appears only on compressively strained SiGe and Ge layers [5], [6].

As a further step to enhance island nucleation and order, pit- and trench-structures with a periodicity of 800 and 400 nm were realized by reactive ion etching with CF4. The overgrowth of the pit-structures with a 500 nm Ge buffer layer at a temperature of 400 °C leads to pits of about 80 nm depth showing {105}, {113} and {15 3 23} facets (Fig. 4(A) and (B)).

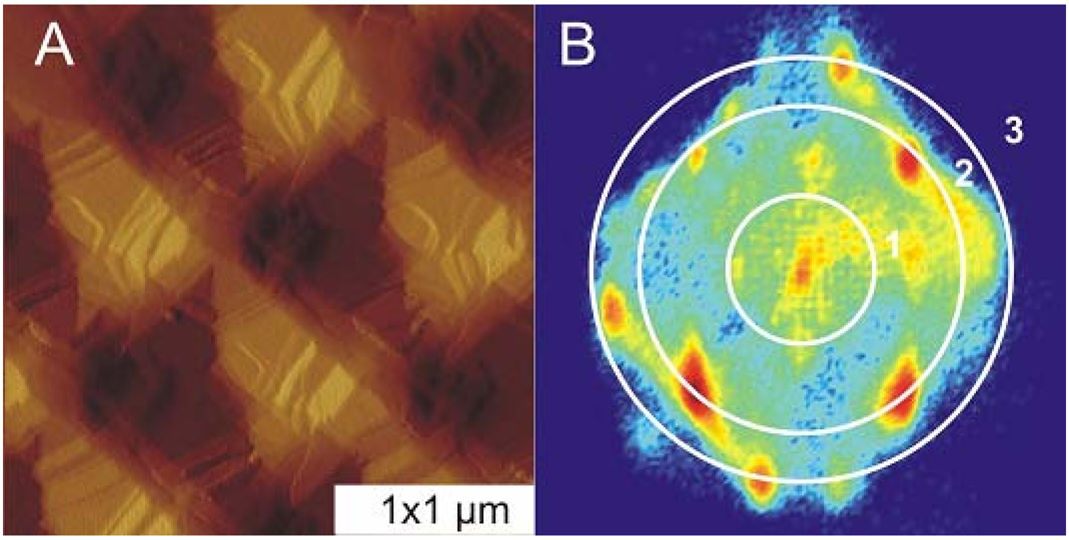

Fig. 4: (A): AFM image in the derivative mode of a 50 nm thick Germanium buffer layer on a pre-structured Ge (001) substrate grown at 400 °C; (B): Surface Orientation Map of A, showing 1:{105}, 2:{113} and 3:{15 3 23} facets.

On these templates we already observed preferential Si island formation, indicating that these structures offer suitable nucleation centers.

References

[1] Y.H. Xie et al., Phys. Rev. Lett. 73, 3006 (1994)

[2] G. Springholz et al., Phys. Rev. Lett. 84, 4669 (2000)

[3] Okumura et al., Appl. Surf. Sci. 125, 125-128 (1998)

[4] Z. Zhong et al., Appl. Phys. Lett. 84, 1922 (2004)

[5] P. Raiteri*, D. B. Migas, and Leo Miglio, A. Rastelli, H. von Känel, Phys. Rev. Lett. 88, 256103 (2002)

[6] Guang-Hong Lu, Feng Liu, Phys. Rev. Lett. 94, 176103 (2005)

Lateral Quantum Dot in Si/SiGe Realized by a Schottky Split-Gate Technique

**T. Berer, D. Pachinger, G. Pillwein, M. Mühlberger, H. Lichtenberger,
G. Brunthaler, F. Schäffler**

**Institut für Halbleiter- und Festkörperphysik, Johannes-Kepler-Universität
Linz, A-4040 Linz**

Introduction

Single electron transistors (SET) in silicon/silicon-germanium heterostructures are of great current interest because of their envisaged use as elements for quantum computation [1]. Recently, several SETs in silicon/silicon-germanium have been reported [2] – [5]. However, none of these were achieved by the classical split-gate technique that is necessary for the coupling of quantum dots and for high integration. Furthermore, it was argued that a SET realized only with Schottky gates is not feasible because of excessive gate leakage currents which were attributed to threading dislocations. We report on the first Coulomb blockade measurements of a SET formed by the split gate technique on a modulation doped SiGe heterostructure.

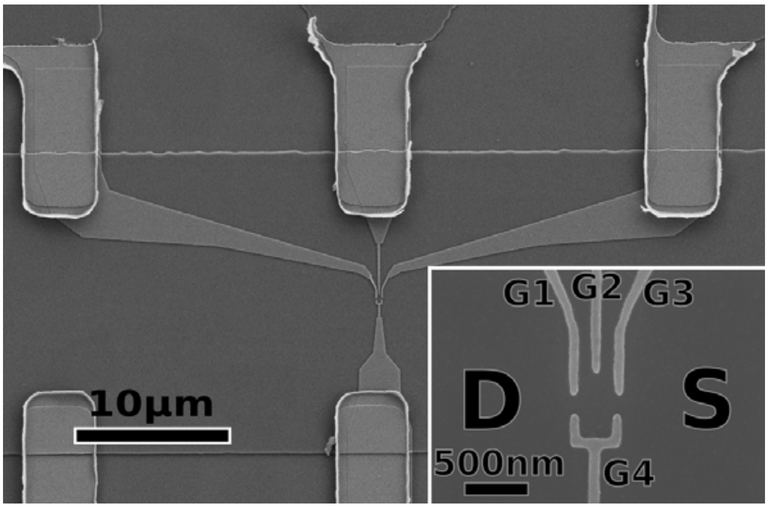

Fig. 1: Scanning electron micrographs of the palladium split gate arrangement on a mesa-etched Hall bar. The main image shows the complete area of the Pd gates including the leads to the bond pads. Insert shows the active SET region defined by the four split gates G1 – G4. The half-pitch of the upper gates is 90 nm.

Sample Preparation

The sample was grown in a Riber SIVA 45 Si molecular beam epitaxy (MBE) apparatus. The 2DEG is formed at the upper interface of a 150 Å thick strained Si channel grown on a 3 µm relaxed step graded buffer ($Si_{0.95}Ge_{0.05}$ to $Si_{0.75}Ge_{0.25}$). A 150 Å thick

$Si_{0.75}Ge_{0.25}$ spacer layer separates the channel from a 150 Å thick antimony doped $Si_{0.75}Ge_{0.25}$ layer. Finally a 450 Å thick layer $Si_{0.75}Ge_{0.25}$ and a 100 Å Si cap were grown. Electrical measurements at 1.5 K showed an electron mobility of 150000 cm^2/Vs at an electron density of 3.2 x 10^{11} cm^{-2}.

Ohmic contacts were formed by deposition of Au/Sb and subsequent annealing at 350 °C for 60 sec. A Hall bar structure was prepared by reactive ion etching (RIE) with SF_6. Subsequently the split gate structures were written by e-beam lithography with a LEO Supra 35 SEM in PMMA. Finally the split gates were fabricated by using a lift-off technique after depositing a layer of Pd. The final structure is shown in Fig. 1. The pitch between the upper gates is 185 nm.

Experiments

As the feasibility of a Schottky-gate approach for SET applications on Si/SiGe heterostructures was generally questioned [2], [3], [6], we carefully characterized the I-V characteristics of the Schottky gates. For testing the worst-case condition, all four gates were connected in parallel to maximize possible leakage currents. The total gate area for the connected gates was about 150 µm². Down to a voltage of about –3 V the total leakage current is below 20 pA (Fig. 2), which is on the lower limit of our experimental setup [7]. Since the measurements we report below are observed at gate voltages between –1.6 V and –1.46 V, we stay safely within the non-conducting part of the diode characteristics.

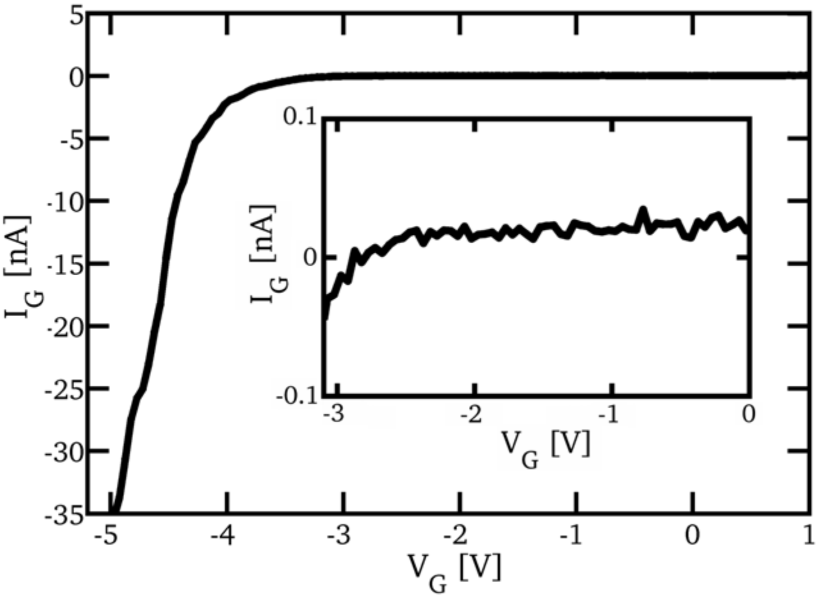

Fig. 2: I-V-characteristics of all gates connected in parallel to maximize possible leakage currents. Down to about –3 V the leaking currents are below the measurement accuracy. The insert shows a zoom-in of the non-conducting range of the diode characteristics.

By applying negative voltages to the gates the underlying 2DEG can be depleted and a quantum dot (QD) is formed. Negative voltages applied to gates G1 and G4, and G3 and G4 define the tunnel barriers, on the drain, and source side, respectively. The QD is controlled by the voltage applied to the plunger gate G2, and the voltage on G4. In the SET operation mode conductance between source and drain is measured as a function of the plunger gate voltage. For this purpose, we utilized a standard low frequency lock-in technique [8]. The experiments were performed in a 3He/4He dilution refrigerator at a temperature of 30 mK. By scanning the voltage V_G, which was here applied to both gates G1 and G2 typical conductance oscillations where recorded (Fig. 3).

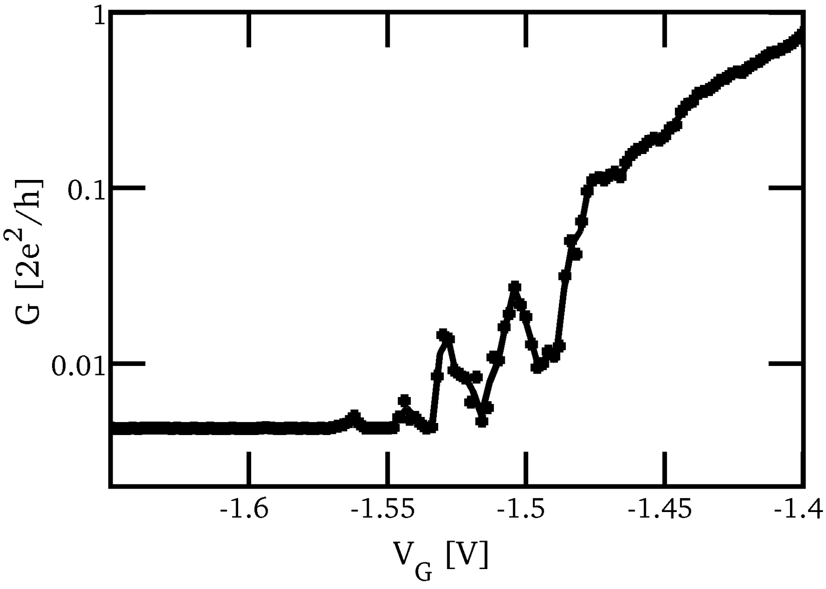

Fig. 3: Conductance oscillations measured at 30 mK by changing the gate voltages of gates G1 and G2 with fixed gate voltage at G3 and G4. One can distinguish different conductance peaks separated by vanishing conductance in the Coulomb-blockade regions. Lines are guides to the eye.

By measuring the conductance as a function of the plunger gate voltage and an additional DC voltage VDS applied between source and drain contacts, one can obtain the quantum dot spectrum, resulting in Coulomb blockade ''diamonds''. Figure 4 shows well resolved Coulomb blockade diamonds. Such experiments reveal the stability of the SET with regard to the number of electrons on the dot [8]. During the measurement time of about 70 h no indication for any transient in the number of electrons was found. Well-behaved Coulomb blockade diamonds were measured up to a temperature of 1.5 K, which was the maximum reachable temperature in the measurement apparatus.

By analyzing the distance between neighboring Coulomb diamonds and their confining slopes we estimated the gate and drain capacity to be $C_G = 6.5$ aF and $C_D = 18$ aF, respectively, and the total dot capacity to be C = 40 aF which results in a Coulomb charging energy of about 4 meV. Assuming the dot to be a metallic disc with radius R we estimated the dot radius to be about 50 nm, which corresponds to a maximum number of about 25 electrons on the dot and an estimated single particle energy spacing of 0.16 meV.

Conclusion

Our experiments demonstrate that Schottky-barrier reducing mechanisms can be overcome by adequately designed Si/SiGe heterostructures and that SET functionality can be achieved in modulation-doped Si/SiGe heterostructures with a standard split-gate approach that can easily be integrated into an array of coupled SETs as suggested in Ref. 1.

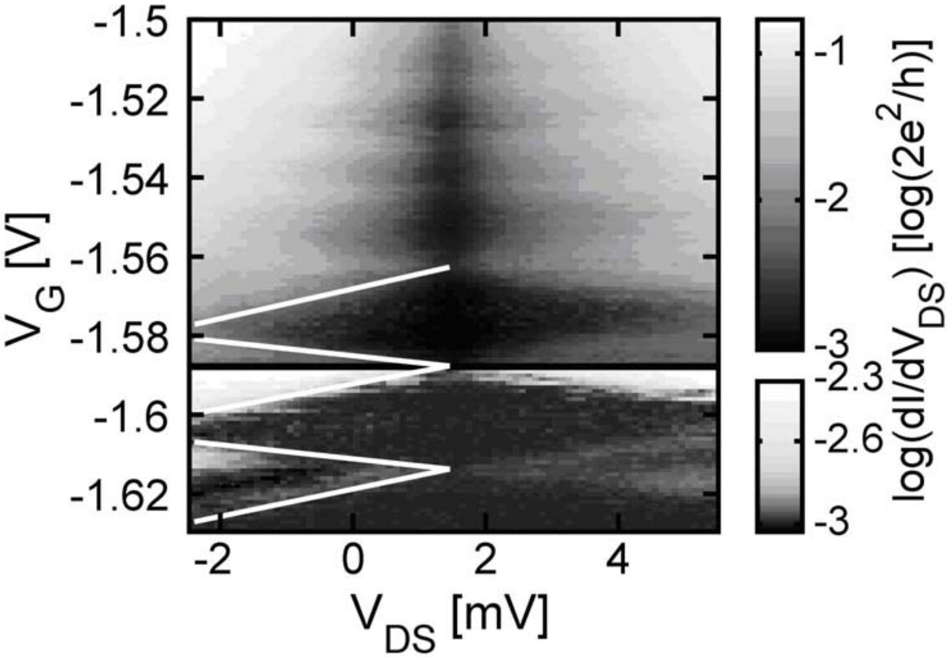

Fig. 4: Stability plot at 30 mK of the differential conductance through the dot as a function of the dc voltage V_{DS} between drain and source, and the gate voltage V_G applied to gates G1 and G2. Seven stability diamonds are clear visible.

References

[1] M. Friesen, P. Rugheimer, D. E. Savage, M. G. Lagally, D. W. van der Weide, R. Joynt, and M. A. Eriksson, Phys. Rev. **B 67**, 1213010 (2003)

[2] A. Notargiacomo, L. Di Gaspare, G. Scappucci,G. Mariottini, F. Evangelisti, E. Giovine and R. Leoni, Appl. Phys. Lett. **83**, 302 (2003)

[3] L. J. Klein, K. A. Slinker, J. L. Truitt, S. Goswami, K.L. M. Lewis, S. N. Coppersmith, D. W. van der Weide, M. Friesen, R. H.Blick, D. E. Savage, M. G. Lagally, Charlie Tahan, R. Joynt, M. A.Eriksson, J. O. Chu, J. A. Ott, and P. M. Mooney, Appl. Phys. Lett. **84**, 4047 (2004)

[4] P. W. Li, W. M. Liao, D. M Kuo, S. W. Lin, P. S. Chen, S. C. Lu, and M.-J. Tsai., Appl. Phys. Lett. **85**, 1532 (2004).

[5] K. A. Slinker, K .L. M.Lewis, C. C. Haselby, S. Goswami, L. J. Klein, J. O. Chu, S. N. Coppersmith, R. Joynt, R. H. Blick, M. Friesen, and M. A. Eriksson, New J. Phys. **7**, 246 (2005)

[6] S. Kanjanachuchai, T.J. Thornton, J.M. Fernandez, and H. Ahmed, Semic. Sci. Technol. **13**, 1215 (1998)

[7] T. Berer, D. Pachinger, G. Pillwein, M. Mühlberger, H. Lichtenberger, G. Brunthaler, and F. Schäffler, Appl. Phys. Lett. **88**, 162112 (2006)

[8] J.Weis, R.J.Haug, K.v.Klitzing, and K.Ploog, Phys. Rev. **B 46**, 12837 (1992), and Phys. Rev. Lett. **71**, 4019 (1993)

Sensor Systems (Posters)

PCR Microsystem for Fast Cycling

G. Hairer[1], M.H. Mansfeld[2], C. Nöhammer[2], M.J. Vellekoop[1]

[1] Institut für Sensor- und Aktuatorsysteme, Technische Universität Wien,
A-1040 Wien

[2] Molekulare Diagnostik, ARC Seibersdorf research GmbH,
A-2444 Seibersdorf

In this paper we present the design, fabrication and test of silicon-glass based PCR chips which amplify specified DNA strands. The design of the chip was optimized to ensure a fast PCR process in terms of thermal cycling speed, biocompatibility, size of reaction chamber and simplicity of fabrication. First tests using a conventional setup for thermocycling show successful DNA amplification in the micro PCR chip.

Introduction

A lot of effort is put into the development of integrated microsystems for analyzing blood and especially DNA. The aim of the integration is to design small devices for fast and cost efficient analysis. Polymerase Chain Reaction (PCR) is a proven technique for amplifying DNA. This method allows multiplying a single DNA molecule up to a billion times. The DNA of the target gene is copied leading to an exponential increase of the number of the gene. The whole process consists of 20 to 50 heat cycles. One PCR cycle contains three different temperature steps. First, the double stranded DNA is heated up to 95 °C to break up the hydrogen bonds (denaturation) and separate the two DNA strands from each other. Next, at a temperature of approximately 55 °C (annealing) gene-specific oligonucleotide primers, which flank the DNA region to be amplified, hybridize to the single strands. Finally these DNA strands are extended in the presence of the thermostable Thermus aquaticus polymerase (Taq) and deoxynucleotide triphosphates (dNTPs) at a temperature of 72 °C (extension) [1].

After first tests on a silicon-glass PCR chip where the filling ports were fabricated in the silicon part, in this paper a modified design of silicon-glass PCR chips is demonstrated and tested. The PCR chip is a single chamber chip with filling ports through the glass. The realization of the filling ports through glass has the advantage that a heating unit can be attached on the silicon side, which improves the thermal behavior of the device and simplifies the injection and extraction of the PCR sample from the chip. Practical issues related to chip design, fabrication process and PCR tests will be discussed in the next sections.

Concept and Design

Several different PCR microsystems have been published [2], which are generally grouped into two principles; (i) the continuous flow PCR microsystems and (ii) the micro chamber PCR systems. In the continuous flow PCR microsystems the reaction mixture is moved between three well-defined temperature zones. The mixture is transported in rotary, serpentine or back and forth motion. In the micro chamber PCR systems the reaction mixture is kept stationary, while the temperature of the reaction chamber is cycled between three different temperatures. Advantages of the chamber PCR are the freedom in the number of cycles to be made and the possibility to test the device in a conventional thermocycler. This allows first PCR tests of the device without any heating and sensing elements on chip and the conventional PCR results can be compared with those of the PCR chip. Therefore, we decided in favor for the chamber PCR concept. To achieve high recovery of the PCR sample the chamber has to be constructed like a channel, where the filling ports are located near the chamber walls. In Fig. 1 on the left hand side the designed PCR chip is shown. The chamber consists of a (wide) channel with funnel shape at the side of the filling ports. The volume of the chamber is 25 µl. The chip dimensions are 15 x 20 mm and the distance between the two filling ports is about 13 mm. The access holes are drilled in the Pyrex glass with a diameter of 1 mm. The reason for realizing the filling ports through glass is that a heating unit can be attached on the silicon side for thermocycling the chamber, which, because of the better thermal conductivity of silicon compared to glass, improves the thermal behavior of the device.

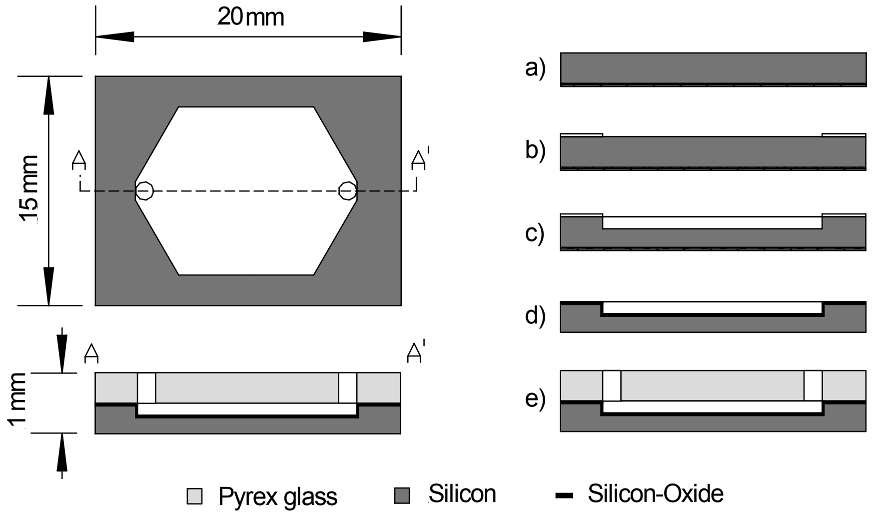

Fig. 1: Design of the PCR chip (top view and cross section) with a reaction volume of about 25 µl (left); Fabrication process of the PCR chip (right)

For fast thermocycling on chip the device has to be small, so that less thermal mass has to be heated and cooled. As a further term the material has to have a high thermal conductivity and a low heat capacity. Silicon fulfills both criteria and additionally, it has excellent structuring characteristics. The heating unit will be realized on the silicon side of the PCR microsystem. As lid a Pyrex glass is used, which has the advantage of allowing insight into the chamber and the possibility of irreversible anodic bonding to the silicon. It can also be machined (through-holes).

Surface chemistry plays a dominant role in PCR reactions within a micro fabricated environment due to the high surface-to-volume ratio. Silicon as such is not very well compatible with DNA and Taq polymerase, since it provokes adhesion effects that can inhibit standard PCR reactions. An oxidized surface however was shown to give consistent amplification that is comparable to those performed in conventional PCR tubes [3]. Thus an oxide layer will be thermal grown on the silicon side in the chamber.

Fabrication Process

The PCR chip is fabricated using photolithography, combined with DRIE (deep reactive ion etching) process, glass drilling and glass-to-silicon dioxide anodic bonding (Fig. 1, right hand side). We used double side mirror polished silicon wafers (100 mm diameter, 525 µm thick, <100>, n-type) coated with an insulating layer consisting of 250 nm thermally grown silicon dioxide and 70 nm LPCVD (low pressure chemical vapor deposition) silicon nitride on one side (a). To fabricate the cavities for the chamber the positive photoresist AZ6624 was coated and patterned on the silicon side of the wafers (b). The reaction cavities were plasma etched to the depth of 180 µm using a DRIE reactor (SF_6/O_2, so called Bosch process) (c). Afterwards a silicon oxide layer with the thickness of 40 nm was thermally grown on the side of the reaction cavities to achieve biocompatibility. The oxide and nitride layers were removed from the wafers with RIE in order to achieve electrical contact during anodic bonding (d). Holes with 1 mm in diameter are drilled in the 500 µm thick Pyrex 7740 glass wafers. Afterwards the wafer is anodically bonded with the silicon wafer to cap the cavities (e). Finally the wafers were diced with a conventional wafer saw.

Fig. 2: Photo of the fabricated PCR chip

Proof of Functionality

The functionality of the PCR chip is tested by placing it into a thermocycler (PTC-200 slide cycler from MJ research). For the thermal cycling a standard PCR program can be run. The temperature of the hot air in the cycler is set at 95 °C for denaturation, 55 °C for primer annealing and 72 °C for extension. Each step is performed for 1 min and to achieve a high yield of DNA amplification 50 cycles are carried out. A standard PCR mastermix is used, where gene-specific primers, deoxynucleotide triphosphates (dNTPs), Taq polymerase and E. coli DNA are included.

The ready-made mastermix is manually injected into the PCR chamber with a conventional pipette. At one port the mastermix is filled in whereas at the other port the air escapes. Before the chip is placed into the thermocycler the filling ports are sealed properly with the PCR tape “ARseal 90404” from Adhesives Research. This prevents gradual evaporation of the sample at denaturation temperature and avoids generating undesired air bubbles in the chamber.

After running the PCR in the conventional cycler the detection of the amplified DNA product is performed off chip. For this the amplified DNA sample is pulled out from the chip with a conventional pipette and afterwards analyzed on an agarose gel. The volumes of the recovered PCR product and the mastermix initially applied to the chip are almost identical due to the chip design. Only tiny amounts of the DNA sample remain at the corners of the reaction chamber.

Figure 3 shows the result of the on chip DNA amplification.

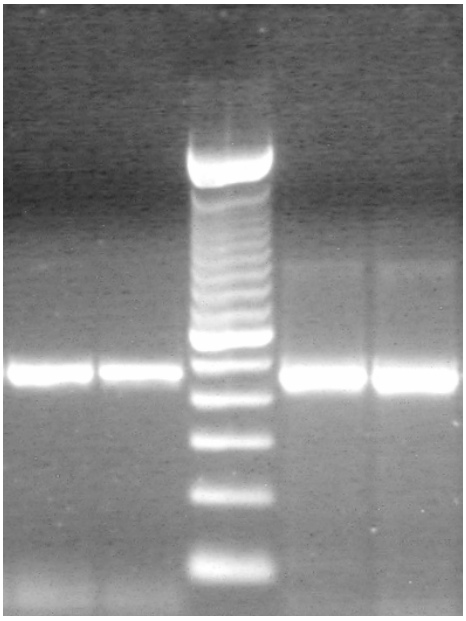

Fig. 3: Agarose gel electrophoresis of 16S rRNA PCR product (497 bp fragment) amplified from E. coli DNA; Lane 1 and 2: single chamber design; in comparison to conventional PCR reaction tubes (Lane 4 and 5). Lane3: 100bp ladder

Discussion

The design of PCR chips with filling ports through the glass has been presented and the functionality of the PCR of these devices has been successfully proven. The device promises miniaturized, fast and effective PCR performance. As a next step a heating unit and thermal sensing elements will be added on the chip to achieve a standalone PCR microsystem.

Acknowledgements

For fabrication of the devices and technical support we thank Dr. A. Jachimowicz, E. Svasek and P. Svasek (ISAS, Vienna University of Technology, Austria) and the Research Centre of Microtechnology at the University of Applied Sciences Vorarlberg, Austria.

References

[1] C.R. Newton, A. Graham: “PCR. Introduction to Scientific Techniques”, BIOS Scientific Publishers Ltd., Oxford 1997, ISBN 1872748821

[2] P.-A. Auroux et al.: “Miniaturised nucleic acid analysis”, Lab Chip, 2004, 4, 534-546

[3] M.A. Shoffner et al.: “Chip PCR. I. Surface passivation of microfabricated silicon-glass chips for PCR”, Nucleic Acids Research, 1996, Vol. 24, No. 2, 375-379

Bridge-Based Microsensor for Determining the Thermal Properties of Liquids

A. Jachimowicz[1], J. Schalko[1], J. Kuntner[1], F. Kohl[2], B. Jakoby[3]

[1] Institute of Sensor and Actuator Systems,
Vienna University of Technology, A-1040 Vienna

[2] Research Unit of Integrated Sensor Systems,
Austrian Academy of Sciences, A-2700 Wr. Neustadt

[3] Institute for Microelectronics,
Johannes Kepler University Linz, A-4040 Linz

Due to unique features like small thermal masses and reduced conductivities, miniaturized thermal sensors offer properties superior to those provided by comparable macroscopic measurement setups. In this contribution a micromachined device is applied to characterize the thermal transport properties of various liquids. By means of sinusoidal excitation of a heater structure placed on a micro-bridge, and recording the resulting temperature at a specified distance using integrated germanium thermistors also located on micro-bridges, the liquid's thermal parameters can be determined. A simple two-dimensional analytical model allows to interpret the amplitude and the phase of the measured sinusoidal temperature variation, yielding both, the thermal conductivity and the diffusivity of the liquid.

Introduction

In the past decades, a number of different measurement methods for thermal material properties of liquids have been developed. Most devices comprise of a single heater or a heater in combination with a spatially separated temperature sensor [1] – [3]. In the former case the temporal evolution of the heater temperature is recorded, whereas in the latter case the temperature in some distance from the heater is measured using the additional temperature sensor. In both approaches the resulting temperature response is determined by the thermal material properties of the surrounding medium and can thus be utilized to extract these parameters. Regardless of the particular realization, all methods aim to restrict an imposed thermal flow to the liquid under test, and to avoid spurious thermal shunts. Due to the unique geometrical features that can be achieved by microtechnology, micromachined devices offer various opportunities for fulfilling this requirement. Here, thin membranes are most commonly applied to decouple the actual sensing region from the sensor substrate and thus obtain high sensitivity and a short response time. For some liquids, however, the remaining spurious heat flow in the membrane is still not negligible. These unwanted thermal shunts can be further decreased by utilizing structures, like cantilevers or micro-bridges. If, on the other hand, materials are used which prohibit exceeding a particular maximum temperature in subsequent process steps, the manufacturing of such sophisticated devices can be challenging. A prominent example is the application of amorphous materials, where high temperatures would cause recrystallization. In this contribution a bridge-based microsensor with highly sensitive amorphous germanium thermistors for determining the thermal conductivity and diffusivity of liquids is presented.

Sensor Design and Fabrication

The sensor presented in this contribution consists of three silicon nitride bridges supported by a silicon frame. On the outer bridges highly sensitive amorphous germanium thermistors (T2 and T3) are located, whereas on the central bridge a chromium heater (H) is placed. Amorphous germanium exhibits high values of both, resistivity and associated temperature coefficient. The specific resistivity is about 5 Ωm and the temperature coefficient of resistance is approximately –1.8%/K at room temperature. Additional thermistors (”substrate thermistors” T1 and T4) arranged at the silicon frame supporting the bridges provide the opportunity of determining the ambient temperature (see Fig. 1 and Fig. 2).

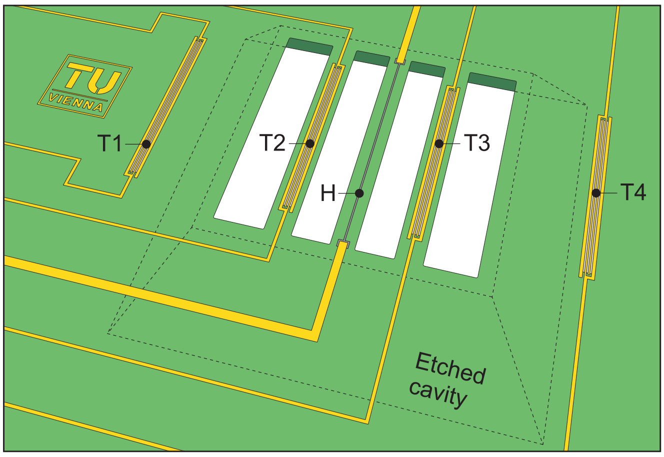

Fig. 1: Schematic picture of the device.

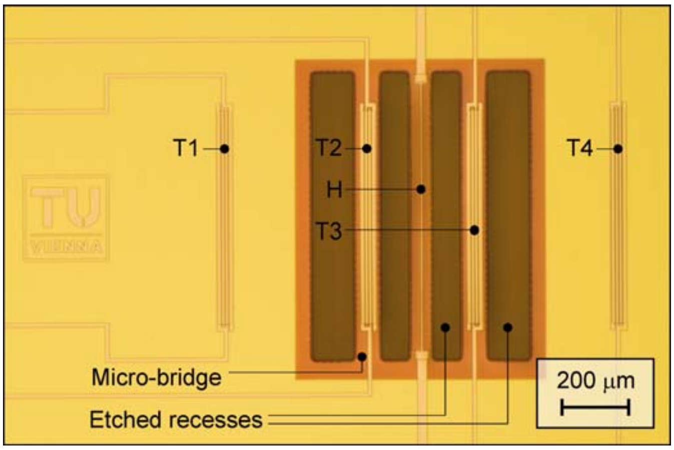

Fig. 2: Photomicrograph of the device.

To fabricate the bridge-based sensor, a 350 µm thick, (100) oriented, and double-sided polished silicon wafer was used. The wafer was coated with 250 nm of thermally grown silicon oxide (SiO_2) and 70 nm of LPCVD silicon nitride (Si_3N_4) on both sides. First, a 250 nm thick layer of germanium has been vapor-deposited and patterned using lift-off technique to form the thermistors. Next, a 130 nm thick layer of chromium has been applied and patterned to create the heater. Subsequently, a titanium-gold-chromium layer featuring a thickness of 50-100-30 nm has been deposited and lift-off patterned to obtain interdigitated electrodes for the thermistors, and connection leads to the bonding pads for heater and thermistors. Then, a low stress silicon nitride (SiN_x) protective film with a thickness of about 1000 nm has been applied using low temperature plasma enhanced chemical vapor deposition (PECVD) at 100 °C. Here, the low deposition temperature prevents the germanium film from recrystallization. Afterwards, square apertures in the wafer backside coating were created by means of photolithography and reactive ion etching (RIE). The membranes have then been manufactured using a KOH based anisotropic wet etching process. In order to obtain the required micro-bridges, the membranes have subsequently been patterned from the topside using photolithography and a RIE process. The apertures for the bond pads were made in the same step. Finally, the chromium has been removed from the bond pad areas by means of a wet-etching. Consequently, the sensor chips feature an overall thickness of about 1.3 µm.

Measurement Principle and Setup

By applying a sinusoidal heater current, a diffusive heat wave propagates from the heater into the surrounding liquid. The steady-state amplitude ΔT_{pk}[1] and the phase Φ of the temperature oscillations measured by the thermistors are determined by the thermal properties of the liquid. The phase Φ denotes the phase lag between the applied heating power and the resulting temperature oscillation. Moreover these temperature oscillations are related to the applied heating power and thus feature twice the frequency of the applied AC heater current plus an additional DC component. Considering the geometry of the heater structure, the corresponding AC temperature field can be approximated by using the solution of the two-dimensional heat diffusion equation for a periodic line source $P(r,t)=P_0 e^{j\omega t}$ yielding

$$\Delta T(r) = \frac{P_0}{2\cdot\pi\cdot\lambda}\cdot K_0\left(\sqrt{\frac{j\omega}{a}}\cdot r\right). \tag{1}$$

Here P_0 denotes the peak of the AC component of the heating power per unit length of the heater structure, λ the thermal conductivity, K_0 the modified Bessel function of the second kind, ω the angular frequency, a the thermal diffusivity, and r the radial distance from the line source [4]. The thermal diffusivity a is related to the heat capacity c_p by

$$a = \frac{\lambda}{\rho\cdot c_p}, \tag{2}$$

where ρ denotes the mass density. It can be seen, that the amplitude in Equation (1) is essentially determined by the thermal conductivity of the liquid under investigation whereas the corresponding phase is governed by the thermal diffusivity. Note that the model above considers heat conductance only, which means that the effects of heat radiation and convection, i.e. flows induced by the non-uniform temperature distribution, are neglected. This can be justified since the considered excess temperatures are in the range of fractions of degree Centigrade. For the measurements, the device was completely immersed into the sample liquid and a sinusoidal heater voltage was applied. In order to single out the steady-state amplitude ΔT_{pk} and the phase Φ of the temperature oscillation measured at the thermistors, a DC voltage was applied to the thermistors and the resulting current oscillations were measured. After eliminating the superposed DC-component, representing the ambient temperature plus the temperature increase associated with the DC-offset of the generated heating power, the amplitude and the phase of the exciting signal's second harmonic were determined by means of a lock-in amplifier (see Fig. 3).

---

[1] Here, Δ indicates the excess temperature, i.e., the difference between ambient and actual temperature.

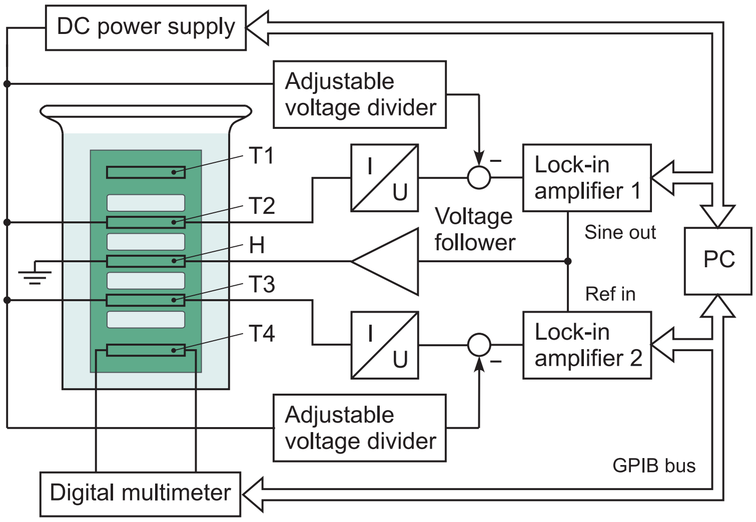

Fig. 3: Measurement setup.

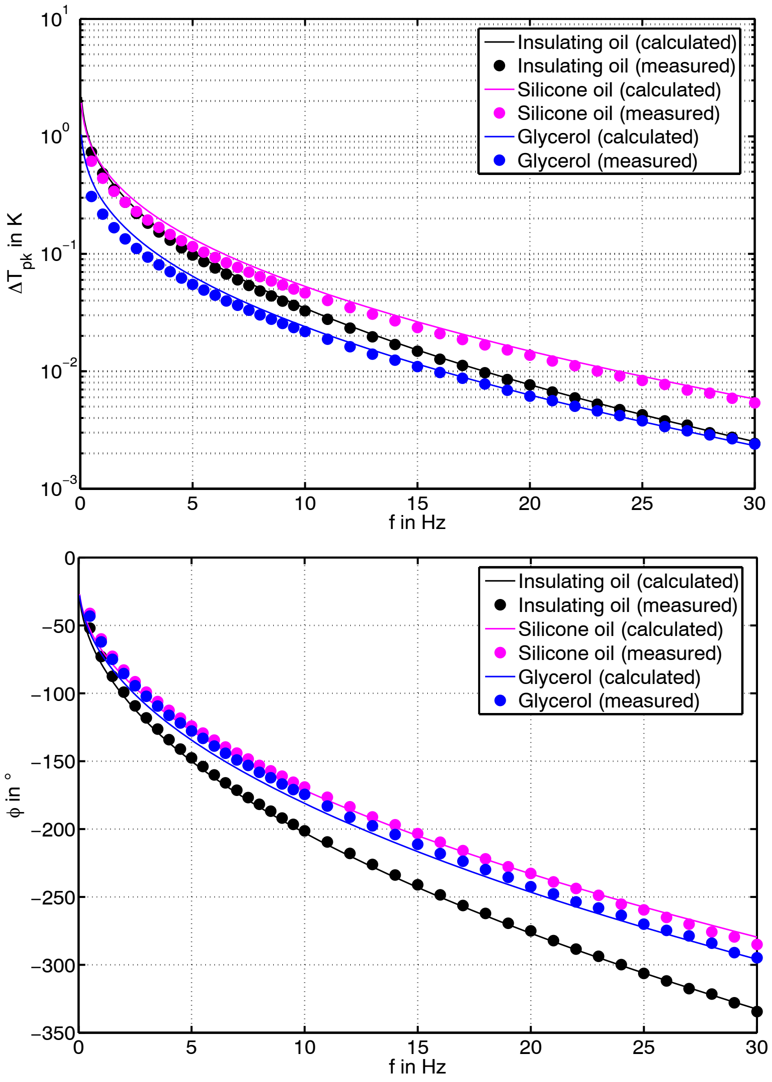

Fig. 4: Amplitude ΔT_{pk} and phase Φ measured for a heater voltage of 1 V_{rms}.

Results and Discussion

In order to investigate the performance of the developed sensor, different liquids have been analyzed. The liquids have been chosen in such a way, that a comparatively large parameter range in both, the thermal conductivity and the thermal diffusivity could be probed. Figure 4 shows the amplitude ΔT_{pk} and the phase Φ of the AC excess temperature amplitude measured at the thermistor T3 compared to the values for the model described above versus the frequency f.

It can be seen that the measurement results correspond well with those predicted by the simple two-dimensional model. Consequently the developed device enables to determine the thermal conductivity and diffusivity of liquids without the need for a complex model for data interpretation.

Conclusion

By utilizing a micromachined structure, the simultaneous measurement of the thermal conductivity and diffusivity of an adjacent liquid has been demonstrated. This was achieved by applying a sinusoidal heater signal and recording amplitude and phase of the resulting temperature increase in some distance by means of a germanium thermistor located on a micro-bridge. A simple two-dimensional analytical model was used to interpret the measurands. The presented approach is well suited for thermal liquid analysis in the laboratory and in the field. In particular, it is suited for online monitoring applications, where size and power consumption can be issues and where the determination of the absolute values is secondary compared to the detection of relative changes.

Acknowledgements

The authors would like to thank E. Svasek and P. Svasek from the Institute of Sensor and Actuator Systems, Vienna University of Technology, for dicing and bonding the devices, respectively. This work was financially supported by the Austrian Research Promotion Agency (FFG), Project 810220 which is gratefully acknowledged.

References

[1] J. J. Healy, J. J. de Groot, and J. Kestin: “The theory of the transient hot-wire method for measuring thermal conductivity”, Physica C, Vol. 82, no. 2, 1976, pp. 392-408.

[2] S. E. Gustafsson, E. Karawacki, and M. N. Khan: “Transient hot-strip method for simultaneously measuring thermal conductivity and thermal diffusivity of solids and fluids”, Journal of Physics D: Applied Physics, vol. 12, no. 9, 1979, pp. 1411-1421.

[3] D. G. Cahill: “Thermal conductivity measurements from 30 to 750 K: the 3ω method”, Review of Scientific Instruments, vol. 61, no. 2, 1990, pp. 802-808.

[4] H. S. Carslaw and J. C. Jaeger: “Conduction of Heat in Solids”, Clarendon Press, 2nd ed., 1986.

Measurement of Liquid Properties with Resonant Cantilevers

C. Riesch[1], E. Reichel[2], F. Keplinger[1], B. Jakoby[2]

[1] Institute of Sensor and Actuator Systems, Vienna University of Technology, 1040 Vienna, Austria

[2] Institute for Microelectronics, Johannes Kepler University Linz, 4040 Linz, Austria

Liquid viscosity and density sensors are essential devices in online process or condition monitoring. Microacoustic sensors combine advantages such as small size, low cost, and absence of macroscopically moving parts. However, these devices feature measurement at high shear rates and, therefore, the results may diverge from those obtained with traditional viscometers. In our contribution we investigate a PZT driven bending actuator and a micromachined doubly clamped bridge device for use as viscosity and density sensors. The presented models allow the description of the sensor's interaction with the surrounding liquid.

Introduction

In many applications like online process or condition monitoring liquid viscosity and density are of high relevance. Microacoustic sensors such as quartz crystal resonators and SAW devices have proved particularly useful alternatives to traditional viscometers [1]. However, these devices basically measure liquid viscosity at high shear rates. The results of microacoustic measurements are thus often not comparable to the readout of conventional viscosity measurement, e.g., based on the Ubbelohde method or rotational viscometers [2]. In contrast, resonating cantilevers allow for measurements at lower frequencies and higher shear amplitudes, making the measuring results more comparable to laboratory methods [3]. Furthermore they allow the determination of liquid viscosity and density separately [4].

In our contribution, we investigate two different types of resonant cantilever sensors: A PZT (lead zirconate titanate) driven bimorph bending actuator and a micromachined sensor utilizing a doubly clamped vibrating beam.

PZT Cantilever Sensor

Sensor Fabrication

Commercially available PZT bimorph bending actuators consist of two piezoelectric PZT layers polarized in the thickness direction and a carbon fiber substrate. Electrodes on both sides of the piezoelectric layers enable the excitation of the actuator. A voltage applied to the electrodes causes transversal contraction in the piezoelectric layer but not in the substrate, and, therefore, leads to flexural mode vibrations of the beam.

The bending actuators used in this work were supplied by Argillon GmbH, Redwitz, Germany. The center electrode is used as ground electrode (Fig. 1(a)), whereas a sinusoidal voltage is applied to the driving electrode to excite bending vibrations. The actual beam deflection is determined by measuring the voltage at the sensing electrode. The phase shift between driving voltage and sensor voltage is measured by means of a lock-in amplifier (Stanford Research SR830). In our setup (Fig. 1(a)), the bending actuator is clamped at one end, whereas different tips of well-defined cross-sections have been attached to the free end of the cantilever (fig. 1b). The clamping fixture is mounted on a rigid frame allowing for vertical positioning of the sensor and preventing vibrations of the whole setup.

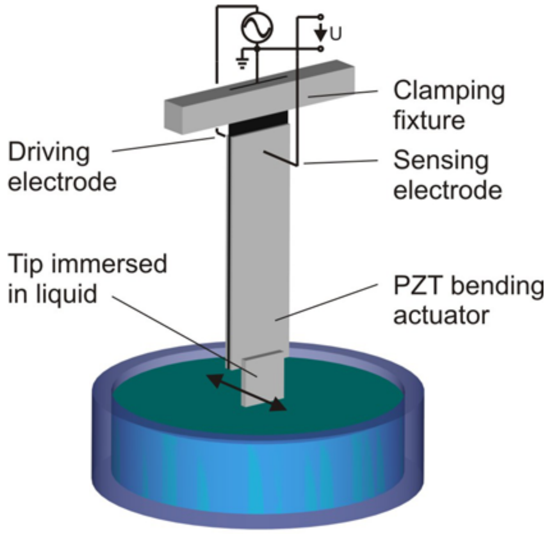

	Tip	Width [mm]	Thickness [mm]
A	Silicon	7	0.5
B	Silicon	5	0.5
C	Silicon	2	0.5
D	terminal pin, soldered on	0.7	0.7

(a) (b)

Fig. 1: (a) Measurement setup; (b) Tip geometries investigated in this work.

Characterization of the PZT Cantilevers

From the cantilever's frequency response we obtained the resonance frequency f_n of the considered vibration mode n and the damping factor D. These parameters are influenced by the liquid's viscosity η and density ρ and the cross-section of the immersed tip. In [5] the relationships between f_n, D and η, ρ were modeled by approximating the oscillating cantilever by an oscillating sphere immersed in a liquid. The force F acting on the said sphere is given by [6]

$$F = \underbrace{6\pi\eta\left(1+\frac{R}{\delta}\right)}_{b_i} u + \underbrace{3\pi R^2\sqrt{\frac{2\eta\rho}{\omega}}\left(1-\frac{2R}{9\delta}\right)}_{M_i}\frac{du}{dt}\,,\quad \delta = \sqrt{\frac{2\eta}{\omega\rho}}\,, \tag{1}$$

where R is the sphere radius, ω the angular frequency, and δ the depth of penetration of the acoustic wave. The terms b_i and M_i represent the additional damping of the cantilever and the added mass due to the surrounding liquid. Considering the bending actuator as an oscillator immersed in a liquid and driven by a harmonic force, the differential equation for the motion u in axial direction is

$$\left(M_e + M_i\right)\frac{d^2u}{dt^2} + \left(b_e + b_i\right)\frac{du}{dt} + Ku = F_0 e^{-j\omega t}\,, \tag{2}$$

where M_e and b_e are the effective mass and the intrinsic damping of the cantilever, K is the spring constant and F_0 and ω are the driving force's amplitude and angular frequency. Based on the oscillating sphere model, a more generalized model for the relationships between $\omega_n = 2\pi f_n$, D and η, ρ was deduced, given by

$$\omega_n = \omega_{n,AIR}\sqrt{\frac{1}{1+c_1\rho+c_2\sqrt{\eta\rho}}} \quad \text{and} \quad \frac{D}{\omega_n^{\,2}} = \frac{D_{AIR}}{\omega_{AIR}^{\,2}}\left(1+c_3\eta+c_4\sqrt{\eta\rho}\right). \tag{3}$$

The model parameters c_1, c_2, c_3, and c_4 were obtained by curve fitting to the equations to the measured data. Figure 2 elucidates that the resonance frequency is dominantly influenced by the liquid's density, whereas the damping is mainly determined by the viscosity. However, there is a “spread” in these straightforward bilateral relations which indicates a cross-sensitivity to the respective other liquid parameter and is properly described by the model (3).

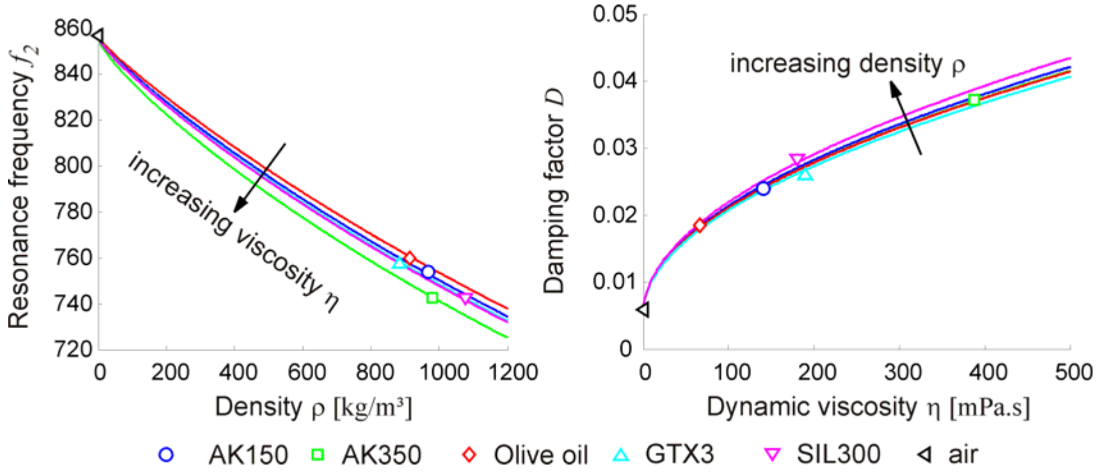

Fig. 2: Measured values (markers) and fitted curves for the respective fluids. These measurements have been obtained with tip A, dipping depth 4 mm.

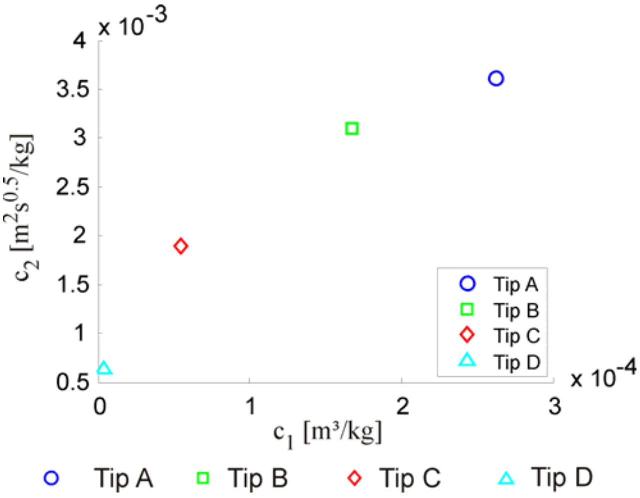

Fig. 3: Fit parameters c_1 and c_2 (associated with $f_n(\eta, \rho)$) for the different tip geometries (Fig. 1(b)).

Figure 3 depicts the dependence of the fit parameters c_1 and c_2 on the kind of tip used. It turns out that the sensitivity of the resonance frequency to the density (determined by c_1) can be steadily increased by increasing the tip width, whereas its sensitivity to the viscosity-density product tends to saturate for increasing widths. This can be explained by the fact that larger amounts of liquid must be moved by the oscillating tip with increasing tip width, whereas the influence of the viscosity is concentrated to the edges of the tip.

Micromachined Doubly Clamped Bridge

Motivated by the applicability for viscosity and density measurement of the PZT cantilevers, effort is being made to miniaturize the sensor with the aim of a sensing device in silicon technology. A precise modeling of the solid-liquid interaction and the measurement of the frequency response enables the measurement of the density and the rheological behavior of liquids [4] in a way comparable to the PZT cantilevers.

A SEM micrograph of a prototype which consists of a doubly clamped beam structure carrying a conductive path is shown in Fig. 4. The beam structure is exposed to a permanent magnetic field and a sinusoidal current through the conductor results in a sinusoidal Lorentz force causing the time-harmonic vibration.

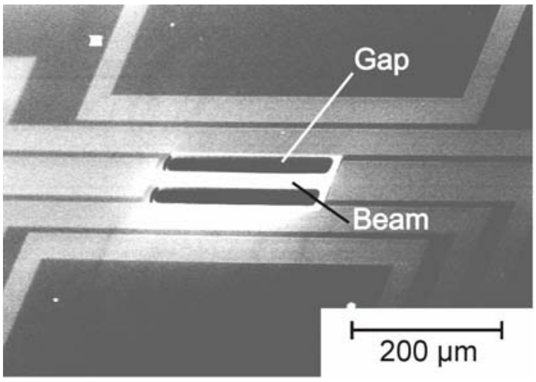

Fig. 4: SEM micrograph of the micromachined sensor element. The cross-sectional dimensions of the Silicon nitride beam are 40x1.3 µm; beams of different lengths ranging from 240 µm to 720 µm were fabricated.

The mechanical deformation (of pure transverse vibration modes) is described by the Bernoulli-Euler beam equation considering an intrinsic normal force *N*, an additional mass m_f and a viscous damping parameter α both resulting from the flow field around the beam:

$$EJ\frac{\partial^4 w}{\partial x^4} - N\frac{\partial^2 w}{\partial x^2} + \left(\rho A + m_f\right)\frac{\partial^2 w}{\partial t^2} + \alpha\frac{\partial w}{\partial t} = q(x,t)$$

where *w* is the deflection, *E* the Young's modulus, *J* the geometrical inertia, ρ the mass density of the beam material, and *x* the spatial coordinate along the beam, $q(x,t)$ is the driving force per unit length.

The additional mass per unit length m_f and the viscous damping coefficient α were calculated from a semi-numerical method based on Green's function in the spatial spectral domain. The simulation of the two-dimensional flow field around the rectangular cross-section yields the dependency of the resistance force on the liquid's mass density ρ_f and viscosity μ shown in Fig. 5.

The readout of the vibration amplitude can be carried out optically, with the integration of piezoelectric materials, or as done here, by measuring the impedance of the excitation circuit over the appropriate frequency range. The electrical equivalent circuit of the vibrating beam in an external magnetic field is depicted in Fig. 6.

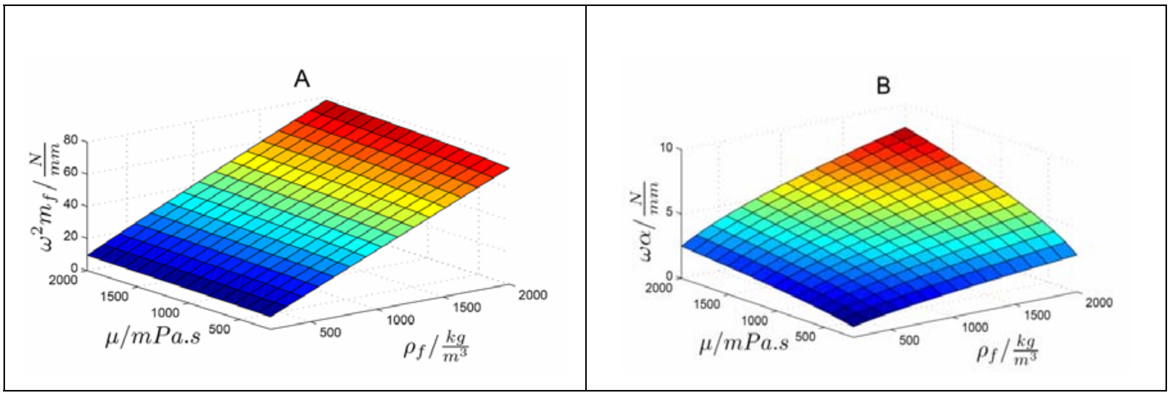

Fig. 5: Results of the semi-numerical analysis of the flow field around the rectangular cross-section of the beam. A: Dependency of the resistance force (per unit length) due to the added mass on both viscosity μ and liquid's density ρ_f. B: Force due to the viscous damping parameter α.

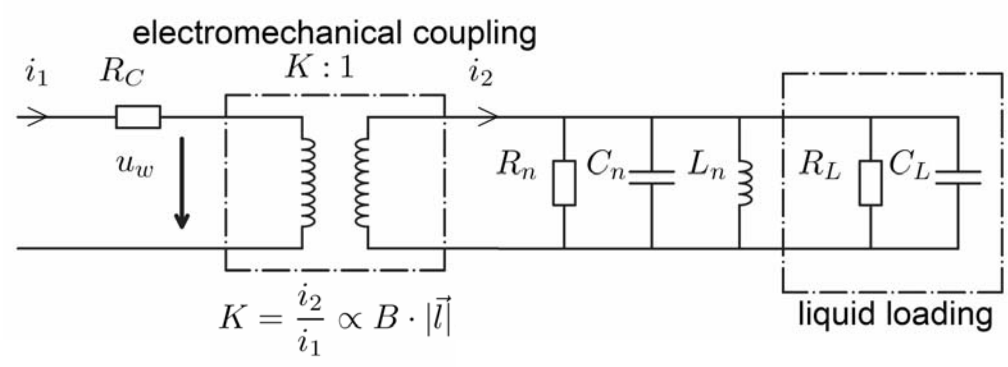

Fig. 6: Electrical equivalent circuit of the vibrating structure. R_C represents the resistance of the excitation path. The parallel resonance circuit on the secondary side of the transformer represents the lumped element approximation of the mechanical system, valid for one specific mode of vibration, and the fluid dependent elements R_L and C_L.

Using the equivalent circuit model it is possible to determine the liquid loading and thus the fluid properties from a measurement of the impedance spectrogram:

$$Z(\omega) = R_C + K^2 \frac{1}{\frac{1}{R_n} + \frac{1}{R_L} + j\omega\left(C_n + C_L\right) + \frac{1}{j\omega L_n}}$$

where R_n, C_n, and L_n are the resonance parameters of mode n in air and R_L and C_L represent the change of the behavior when the structure is immersed in a liquid due to additional damping and additional mass respectively.

Conclusion

In the paper we have investigated two different types of resonant cantilevers for the measurement of liquid properties. The resonance frequency as well as the damping of the cantilevers are influenced by the surrounding liquids. The relationships between the cantilever's frequency response and the liquid parameters were described by models, allowing for separate determination of liquid viscosity and density.

Acknowledgements

This work was supported by the Austrian Science Fund (FWF) Project L103-N07.

References

[1] B. Jakoby, M. Scherer, M. Buskies, H. Eisenschmid: "Microacoustic Viscosity Sensor for Automotive Applications", Proc. IEEE Sensors, 2002, pp. 1587–1589.

[2] A. Agoston, C. Ötsch, B. Jakoby: "Viscosity sensors for engine oil condition monitoring – Application and interpretation of results", Sens. Actuators A, Vol. 121, 2005, pp. 327–332.

[3] A. Agoston, F. Keplinger, B. Jakoby: "Evaluation of a vibrating micromachined cantilever sensor for measuring the viscosity of complex organic liquids", Sens. Actuators A, Vol. 123–124, 2005, pp. 82–86.

[4] L. F. Matsiev: "Application of Flexural Mechanical Resonators to Simultaneous Measurements of Liquid Density and Viscosity", 1999 IEEE Ultrasonics Symposium, 1999, pp. 457–460.

[5] W. Y. Shih, X. Li, H. Gu, W.-H. Shih, I. Aksay: "Simultaneous liquid viscosity and density determination with piezoelectric unimorph cantilevers", J. Appl. Phys., Vol. 89 (2), 2001, pp. 1497–1505.

[6] L. D. Landau and E. M. Lifshitz: "Fluid Mechanics", Pergamon Press, London, 1959.

Sensitive Measurement of Flow Velocity and Flow Direction Using a Circular Thermistor Array

F. Keplinger, J. Kuntner, A. Jachimowicz, F. Kohl

Institute for Sensor and Actuator Systems
Vienna University of Technology, A-1040 Vienna

Eight highly sensitive amorphous germanium thermistors (TCR = -1.8%/K) are the sensitive part of the micromachined sensors for flow velocity and flow direction. Carried by a 1.3 µm thick diaphragm they measure temperature differences generated by the sample flow and a heater (430 µW). This allows gas flow measurements in the range from 0.025 m/s to about 3 m/s with a sensitivity of up to 30 mV/(m/s). Two orthogonal pairs of opposed thermistors feature a sensitivity of 150 µV/°. An increase in sensitivity (50%) is gained by using two 90° rotated thermistors situated in the downstream position.

Introduction

Measurement of fluid velocity combined with the acquisition of flow direction is a challenging task in different fields of research. Especially miniaturized sensors are suitable for investigation of flows with high spatial resolution which are not accessible for mechanical anemometers. The current miniaturized cutting-edge devices are based on the thermal anemometer principle allowing the simultaneous measurement of flow direction and velocity [1]. The application of amorphous germanium thermistors for flow sensor [2] with their high resistive temperature coefficients (TCR) initiated the design of extremely sensitive flow direction sensors. Moreover, a further increase in sensitivity of the direction measurement was expected by the use of four additional thermistors.

Sensor Principle

Basis of the sensor is the so-called ‘calorimetric’ measurement principle where a thin diaphragm supported by a micromachined silicon frame is flush mounted with the wall surrounding the flow channel. A thin-film resistor (heater) at the centre position of the diaphragm generates a symmetric temperature distribution on the diaphragm as long as the flow velocity is zero. When a tangential flow occurs, the thermal symmetry is broken. Two thermistors, placed symmetrically in respect to the heater and parallel to the flow, are used to measure the temperature difference. More heat is transported to the downstream thermistor than to the upstream ones, a difference signal is generated which is a measure for the velocity. Applying more than one thermistor pair on the diaphragm being rotated appropriately compared to the first one, the direction of the flow within the diaphragm plane can be measured.

For high sensitivity the diaphragm has to have a high thermal resistance. The heat should be transported mainly by the sample flow and not by thermal conduction within the diaphragm. Therefore the diaphragm has to be as thin as possible making it very fragile.

Experimental

Sample Preparation

The sensor structures (Fig. 1) are evaporated on a <100>-Si wafer, passivated on both sides with 250 nm SiO_2 and 70 nm Si_3N_4. A chromium meander (300 µm x 5 µm x 130 nm, 580 Ω) serves as heater. The thermistors consist of amorphous germanium (250 nm, 75 µm² x 5 µm, 320 kΩ). Amorphous germanium was chosen as thermistor material because its resistivity is highly sensitive to temperature changes [2]. It exhibits a TCR of about -1.8%/K being almost five times higher than the corresponding value of platinum. The thermistors are contacted by an interdigital sandwich structure consisting of 50 nm titanium (at the germanium side), 100 nm gold and 30 nm chromium.

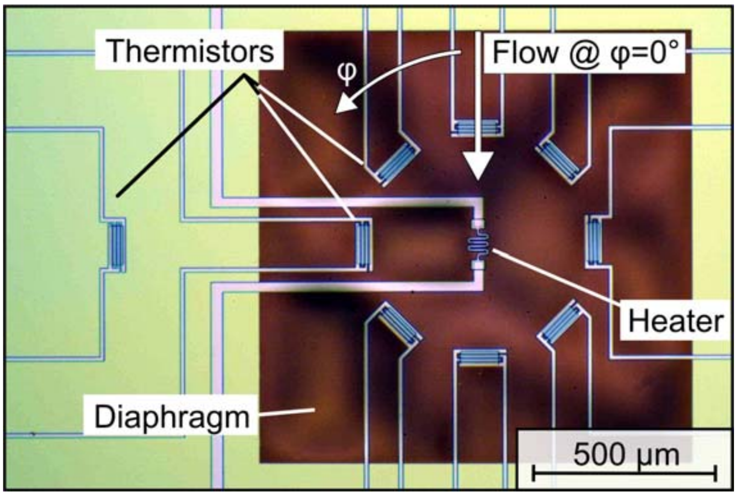

Fig. 1: Micrograph of the flow sensor consisting of eight thermistors on the 1.3 µm thick diaphragm and one on the surrounding Si-frame to measure the ambient temperature. φ denotes the direction of the flow in respect to the N-S-direction. Due to the buckling of the diaphragm it is irregularly shaded.

The metal layer and the Ge layer are evaporated and patterned with an image reversal photo resist. The complete structure is isolated by 1 µm thick LPCVD silicon nitride. Finally, the diaphragm is generated by anisotropic etching with a 30 wt% potassium hydroxide solution at 80 °C. The etching process is stopped by the silicon oxide layer of the wafer. The diaphragm features a size of 1.2 x 1.2 mm^2 and an overall thickness of 1.3 µm. It is an inherent property of the anisotropic etching process of a <100>-Si-wafer that the boundaries of the etched cavity are formed by {111}-planes [3]. Therefore the cavity is a truncated pyramid, bounded by a rectangular silicon nitride membrane.

Measurement Setup

The sensor is positioned flush with the wall of a flow channel (rectangular cross-section of 12 mm x 1 mm) and can be rotated 360° as indicated in Fig. 1. Filtered nitrogen is used as fluid and controlled by a flow controller allowing a maximum velocity of 2.8 m/s. The central Cr resistor is heated up by 430 µW in the constant voltage mode (over-temperature of approximately 5 K). The thermistors resistances are measured by applying constant voltage (5 V) and current-to-voltage converters (120 mV/µA) based on the ultralow noise BiFET OpAmp AD743. Their output voltages are recorded by a PC-controlled data acquisition board (Fig. 2).

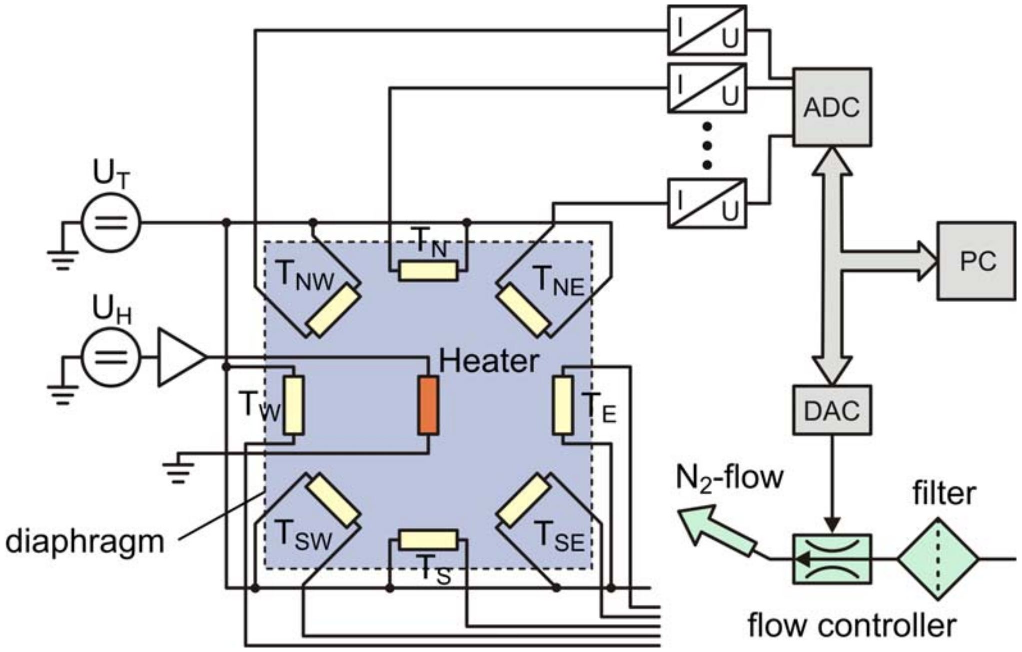

Fig. 2: Schematic measurement setup. Thermistors T_N, T_{NE}, T_E, … T_{NW}, U_T thermistor voltage, U_H heater voltage.

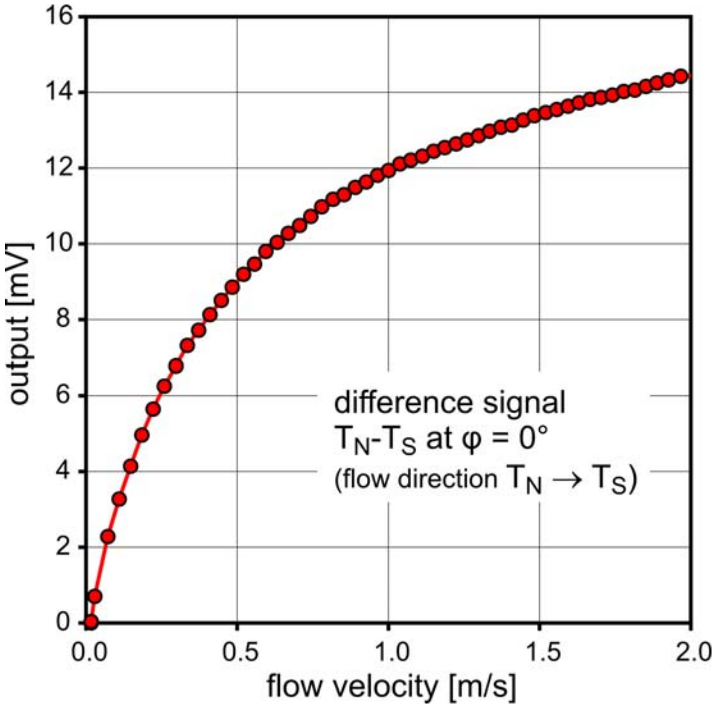

Fig. 3: Difference signal ($T_N - T_S$) of the thermistors at the north and south position versus flow velocity. The channel is oriented in parallel to the connecting line of the thermistors. Heating power: 430 µW.

Measurements

As an example, the measured difference signal of the north/south thermistor pair (Fig. 3) emphases the high sensitivity of the sensor for flow velocities. The gas flows parallel to N-S-direction, the heater is operated in the constant heating power mode. For low velocities the sensitivity is 30 mV/(m/s). At higher velocities the overtemperature of the upstream thermistor vanishes. Also the downstream sensor gets less and less heated because more and more gas has to be heated up. Beyond a velocity of 3 m/s the temperature difference decreases with increasing flow rate.

The dependence of the difference signal of opposed sensors versus flow direction is plotted in Fig. 4 (thick lines). The direction sensitivity for flow with an angle smaller than 60° in respect to the connecting line is about 150 µV/°. Evaluating the signal difference of 90° rotated thermistors (e.g., S-E) the directional sensitivity can be improved by approximately 50%, when the thermistor pair is near the downstream position.

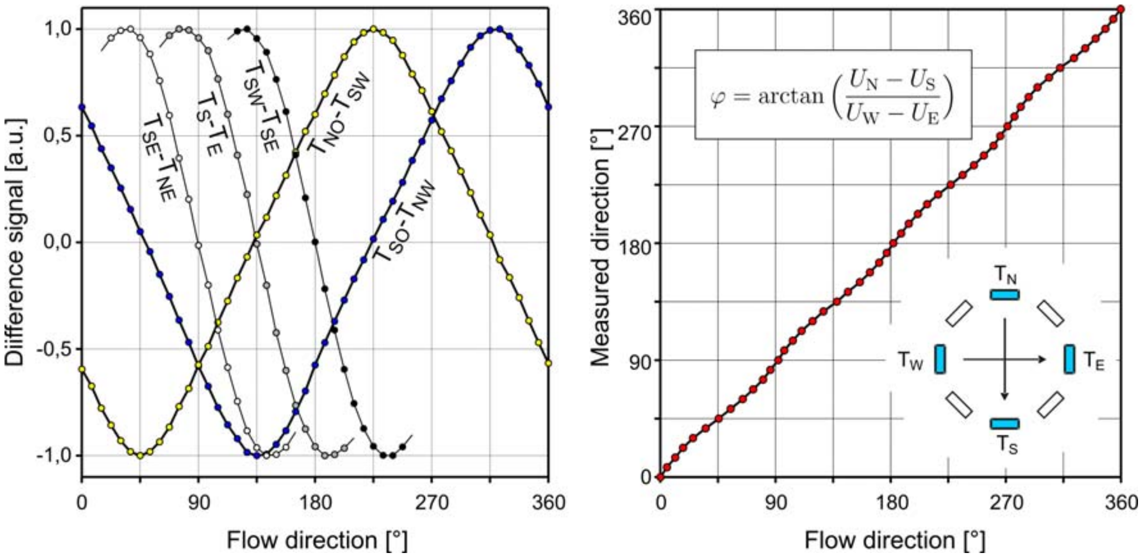

Fig. 4: Left: Measured and normalized difference signals of opposed (thick lines) and of 90°-rotated thermistors (thin lines). Right: Measured flow direction assuming sinusoidal characteristic of the difference signals of opposed sensors (N-S and W-E).

The value of the angle of the flow direction can be determined using the difference signals of two thermistor pairs: $\varphi = \arctan\left[(U_N - U_S)/(U_W - U_E)\right]$ taking into account the signs of the individual differences to decide the quadrant. The function assumes a sinusoidal response of the difference signal to the flow direction. The deviations from this are mainly responsible for the nonlinearity in the measured direction of Fig. 4.

Conclusion

The application of amorphous germanium enables the development of highly sensitive sensors for flow velocity and flow direction measurement. By applying eight thermistors the angular resolution can be increased by about 50%. The directional characteristic of a single thermistor deviates significantly from a sinusoidal function. A very high accuracy is achievable using all available thermistor signals and more sophisticated evaluation schemes. Additionally, improved sensor designs are feasible to take full advantage of the superior properties of the thin-film thermistors.

References

[1] S. Kim, S. Nam and S. Park: “Measurement of flow direction and velocity using a micromachined flow sensor”, Sens. Actuators A, vol. 114, 2004, pp. 312–318.

[2] F. Kohl, R. Fasching, F. Keplinger, R. Chabicovsky, A. Jachimowicz and G. Urban: “Development of miniaturized semiconductor flow sensors”, Measurement, Vol. 33, 2003, pp. 109–119.

[3] M. Elwenspoek and H. Jansen: “Silicon Micromachining”, Cambridge University Press, Cambridge, England, 1998.

ISBN: 978-3-901578-17-5